

# University of Alberta

Geology and Geochemistry of Late Devonian-Mississippian Sediment-Hosted  
Barite Sequences of the Selwyn Basin, NWT and Yukon, Canada

by

Neil Andrei Fernandes

A thesis submitted to the Faculty of Graduate Studies and Research  
in partial fulfillment of the requirements for the degree of

Master of Science

Department of Earth and Atmospheric Sciences

©Neil A. Fernandes

Fall 2011

Edmonton, Alberta

Permission is hereby granted to the University of Alberta Libraries to reproduce single copies of this thesis and to lend or sell such copies for private, scholarly or scientific research purposes only. Where the thesis is converted to, or otherwise made available in digital form, the University of Alberta will advise potential users of the thesis of these terms.

The author reserves all other publication and other rights in association with the copyright in the thesis and, except as herein before provided, neither the thesis nor any substantial portion thereof may be printed or otherwise reproduced in any material form whatsoever without the author's prior written permission.

*School should teach you how to learn, not what to think...*



*For Sarah Gleeson and Tom Chacko,  
for taking a chance on me when nobody would.  
For my Mother,  
for believing in me even when I could not  
believe in myself.*

***Abstract:***

A sediment-hosted barite horizon occurs in the upper part of the lower Earn Group in the Selwyn Basin, NWT, Canada. This horizon consists of synsedimentary, laminated barite and diagenetic, nodular barite which are hosted in shale, siltstone and mudstone. The lithogeochemistry of the sediments associated with these horizons indicates a reducing, oxygen-depleted environment of deposition. Stable isotope geochemistry indicates a limited supply of sulphate in the Selwyn Basin at this time.

Epigenetic barite and witherite, intergrown with base-metal sulphides is hosted by the lower Earn Group in the Walt/Tyrjala/Hess occurrences in the Mac-Millan Pass District, Yukon and has similar geochemical characteristics.

A reducing, Ba and H<sub>2</sub>S-rich fluid transported along faults; was carried to the seawater-interface where it precipitated barite from seawater and porewater sulphate in the NWT study area. A fluid of similar composition reacted with an oxidized, Zn-Pb-SO<sub>4</sub>-CO<sub>3(aq)</sub>-bearing brine to form the mineral assemblages in the Walt/Tyrjala/Hess occurrences in the Yukon.

### *Acknowledgements*

Both the NTGO and YGS have provided tremendous financial and logistical support for a project that covered such a large, normally inaccessible area. This research was also supported by an NSERC discovery grant to Dr. Sarah Gleeson.

There are so many people who have been a part of this project and they all have played a key role in helping with my development as a geochemist and as a field geologist. Bob Sharp came up with the initial question as to the origin of the barite horizons in the NWT and has been an ever-present source of ideas. Edith Martel and Hendrik Falck from the NTGO got this project off the ground and have given unending support in its development. Venessa Bennett taught me a great many things about fieldwork and to never be myopic in my thought process. Dr. Elizabeth Turner from Laurentian University made me a knight of the realm of stratigraphy. Teck Resources is gratefully acknowledged for providing samples from Hess and Nidd drill core.

The Department of Earth and Atmospheric Sciences at the University of Alberta is home to a lot of people who have inspired me and gave me a chance to perform research. Dr. Thomas Stachel gave me an unexpected source of motivation with his kind words and positive outlook. Dr. Murray Gingras provided stimulating discussions on sedimentology and stratigraphy. Dr. Sergei Matveev taught me the patience to run marathon microprobe sessions. Dr. Karlis Muehlenbachs inspired me with his vast knowledge of isotope geoscience and showed me the true meaning of broad-minded research. Dr. Kurt Konhauser helped me understand low-temperature geochemical processes and the incredible effects that single-celled organisms can have on geochemistry. Dr. Robert Creaser must be thanked for swift Re-Os analyses but more importantly, for giving me an idea that fundamentally shaped my final interpretation and model.

The Mackenzie Mountains have given me many dreams (and nightmares) that have profoundly impacted my psyche and have made me a better person for it.

The greatest gift that one can be given is a second chance. Sarah Gleeson and Tom Chacko let me in the door to graduate studies in EAS. Every single thing I have learnt or gained from my experiences in the last two years is a reflection of their belief in me and the initial gamble that they took. The small thanks that I can offer to both of them can be found in all the pages of this thesis.

## ***Table of Contents***

<u>Chapter One: Introduction</u>	1
1.1. Introduction	1
1.2. Rationale and objectives of study	3
<u>Chapter Two: Geological background, Field methods and results</u>	5
2.1 Background geology of the NWT study area	5
2.2 NWT field results	7
2.2.1 Non-barite bearing Canol Formation:	8
2.2.2 Barite occurrences with measured sections	10
2.2.3 Barite occurrences with no measured sections:	15
2.3 Summarized NWT field results	16
2.4 Geological setting of the Yukon study area	17
2.5 Yukon sediment-hosted barite field results	19
2.5.1 Field relationships	20
2.5.2 Hess Drill Core	23
<u>Chapter Three: Analytical Procedures</u>	25
3.1. Petrography and EPMA	25
3.2 Stable isotope geochemistry of sulphates and sulphides	26
3.3 Re and Os isotope isotope analysis	27
3.4 Bulk sediment lithogeochemistry	27
<u>Chapter Four: Petrography and Mineralogy</u>	29
4.1 Barite petrography and mineralogy	29
4.1.1 Pyritic debritic mudstone at Cooper showing	29
4.1.2 NWT Laminated barite	30
4.1.3 NWT Nodular barite:	33
4.1.4 Cowan epigenetic barite and nodular barium carbonate	36
4.2 Hess ‘mineralized’ barite petrography and mineralogy	40
4.2.1 Hess barite drill core:	40
4.2.2 Paragenetic sequence of minerals at Hess:	48
<u>Chapter Five: Geochemical Results</u>	50
5.1 NWT ‘barren’ barite geochemistry	50
5.1.1 Geochemistry of Late Devonian Canol Fm. sediments	50

5.1.2 $\delta^{34}\text{S}$ and $\delta^{18}\text{O}$ isotope geochemistry of NWT barite	53
5.2 Walt/Tyrala/Hess/Cathy ‘mineralized’ barite geochemistry	54
5.2.1 Geochemistry of Middle Devonian Portrait Lake Fm. sediments	55
5.2.2 $\delta^{34}\text{S}$ and $\delta^{18}\text{O}$ isotope geochemistry of minerals from outcrop and Hess drill core	57
5.2.3 Re-Os isotope systematics of Hess pyrite	59
<u>Chapter Six: Discussion</u>	61
6.1 NWT ‘barren’ barite	61
6.1.1 The stratigraphic position of synsedimentary-diagenetic barite	61
6.1.2 Basin geochemistry and geochemical processes during formation of barite horizons in the upper Canol Fm.	64
6.1.3 Geochemical comparisons with modern environments	71
6.2. Walt/Tyrala/Hess mineralized barite, Yukon	73
6.2.1 Lithochemistry of middle Devonian Portrait Lake Formation sediments	73
6.2.2 Timing of mineral assemblages and geochemistry of Stage 1 sulphides and sulphates at Hess: Implications for fluid geochemistry and sulphur sources	74
6.3 Barite and its relationship with sediment-hosted Pb-Zn deposits: Implications for further exploration in the Selwyn Basin	80
<u>Chapter Seven: Conclusions and directions for future research</u>	86
7.1 Conclusions	86
7.2 Directions for future research	87
<u>Chapter 8: References</u>	89
Appendix A: Stratigraphic sections	A-i
Appendix B: Microprobe data	B-i
Appendix C: Lithochemistry Data	C-i
Appendix D: Re-Os model data	D-i

## *List of Figures*

Figure 1.1: Idealized cross-section of a vent proximal SEDEX deposit	2
Figure 1.2: Regional geology of the northern Cordillera in the Northwest Territories, Yukon, British Columbia and Alaska	3
Figure 2.1: Paleographic reconstruction and interpretation of the North American continent during the late Devonian	5
Figure 2.2: Selwyn Basin stratigraphy	6
Figure 2.3: Earn Group stratigraphy	7
Figure 2.4: NWT study area field map	8
Figure 2.5: Compiled NWT stratigraphic sections	17
Figure 2.6: District map of the MacMillan Pass region, Yukon	18
Figure 2.7: Geological map of Yukon study area	20
Figure 4.1: Ternary plot of hyalophane composition	36
Figure 5.1: Chondrite-normalized REE plots of samples from the NWT	52
Figure 5.2: $\delta^{34}\text{S}$ and $\delta^{18}\text{O}$ values of NWT barite plotted against the S- and O-isotope curves of Claypool et al. (1980)	54
Figure 5.3: Chondrite-normalized REE plots of samples from the Walt/Tyralla/Hess barite occurrences	56
Figure 5.4: $\delta^{34}\text{S}$ and $\delta^{18}\text{O}$ values of Walt/Tyralla/Hess barite plotted against the S- and O-isotope curves of Claypool et al. (1980)	58
Figure 5.5: Re-Os data for Hess pyrite	60
Figure 6.1: Stratigraphic position of barite horizons in the Earn Group, NWT	61
Figure 6.2: Schematic depth zonation of biogeochemical processes in marine sediments applied to barite-forming environments	66
Figure 6.3: Re-Os values for Hess pyrite plotted on a graph of $^{187}\text{Re}/^{188}\text{Os}$ against $^{187}\text{Os}/^{188}\text{Os}$ with 2-point isochrons calculated for individual pyrite pairs and theoretical Re-Os isotope system evolution of a black shale	76
Figure 6.4: Schematic diagram of mineralizing events and mineral assemblages generated as a result of fluid-fluid interactions	81
Figure 6.5: Log $f\text{O}_2$ -pH diagrams showing stability fields for Fe oxides and sulfides, siderite, solubility contours, and the metal transport window for galena and sphalerite, and for barite and witherite	83

### ***List of Plates***

Plate 2.1: Background Canol Formation	10
Plate 2.2: Outcrop view of NWT barite occurrences	12
Plate 2.3: Harp occurrence	15
Plate 2.4: BA and Cowan occurrences	16
Plate 2.5: Yukon barite occurrences	22
Plate 2.6: Hess drill core	24
Plate 4.1: Cooper petrography	30
Plate 4.2: NWT laminated barite petrography	32
Plate 4.3: NWT nodular barite petrography	34
Plate 4.4: Cowan barite petrography	37
Plate 4.5: Yukon barite outcrop petrography	39
Plate 4.6: Lower Earn Group sediments in Hess drill core	41
Plate 4.7: Carbonate gangue minerals in Hess drill core	42
Plate 4.8: Pyrite in Hess drill core	44
Plate 4.9: Lead minerals in Hess drill core	46
Plate 4.10: Zinc minerals in Hess drill core	48

### ***List of Tables***

Table 3.1: Average detection limits for EPMA on NWT laminated barite, NWT nodular barite, Yukon barite	25
Table 3.2: Average detection limits for EPMA on silicates	25
Table 3.3: Average detection limits for EPMA on Hess drill core sulphides	26
Table 4.1: Average major element composition of NWT laminated barite, NWT nodular barite, Cooper NWT barite and Yukon barite	31
Table 4.2: Average major element composition of hyalophane in laminated and nodular barite, cymrite and albite from NWT barite occurrences	35
Table 4.3: Average elemental composition of sulphides and sulphosalts from the Hess barite hole	45
Table 5.1: $\delta^{34}\text{S}$ and $\delta^{18}\text{O}$ values of NWT barite	53
Table 5.2: $\delta^{34}\text{S}$ and $\delta^{18}\text{O}$ values of Yukon barite and $\delta^{34}\text{S}$ values of Hess sulphides	57
Table 5.3: Re/Os isotopic data for pyrite from Hess drill hole.	59

# CHAPTER ONE: INTRODUCTION

## 1.1. Introduction

Sedimentary basins host some of the world's major base metal (Zn, Pb, Cu) mineral deposits e.g., McArthur Basin, Australia; the Zambian Copperbelt; and Rammelsburg, Germany. In particular, sedimentary-exhalative (SEDEX) deposits are an important source of these commodities.

SEDEX deposits gain their name from the original model proposed by Carne and Cathro (1982), whereby fluids were 'exhaled; and precipitated metals on the seafloor'. In this model fluids are sourced from deep within the basin, and are transported along structures such as synsedimentary faults to the sediment-seawater interface (SWI). Upon reaching the seafloor, the mineralizing fluids then interact with the water column, which is thought to be stratified into an upper oxygenated layer and a lower anoxic layer (Goodfellow, 1987). In this model, sulphide minerals, mostly occurring as sphalerite and galena, precipitate due to mixing of anoxic, reduced ( $\text{H}_2\text{S}_{\text{aq}}$ -rich) seawater with saline, metaliferous, oxidized ( $\text{H}_2\text{S}_{\text{aq}}$ -poor) fluids. Barite ( $\text{BaSO}_4$ ) is thought to represent the distal component of the hydrothermal vent associated with SEDEX mineralization, and is precipitated in the upper, oxygenated ( $\text{SO}_4^{2-}$ -rich) layer. Hence, stratification of the ocean is crucial for both sulphide and barite precipitation. Minerals precipitated as a result of these reactions accumulate on the basin floor along with normal marine sediments to form stratiform deposits with sulphide-rich, sulphate-rich and sediment-rich laminations that can often display normal sedimentary features such as bedding and grading. Therefore according to this model, it should be possible to use barite textures to source the sulphide component of a SEDEX system.

SEDEX deposits around the world have some common features. The most important characteristic of these deposit-types are Pb and Zn sulphides which are interlaminated with fine-grained sedimentary lithologies (shale, mudstone, Leach, 2010). The synsedimentary model (i.e., co-precipitation of sulphides and basinal sediments) proposed by Goodfellow et al. (1993) for the formation of these stratiform deposits is largely based on these textural interpretations.

One subset of SEDEX deposits is the vent-proximal type (Goodfellow et al., 1993). The conduit for fluids in this case is thought to be a growth fault that creates relief on the seafloor (Goodfellow and Lydon, 2007). The vent facies can be recognised in paleosystems by the brecciation of the basinal units, and the replacement of the host rocks by sulphides and iron carbonates (Fig. 1.1).

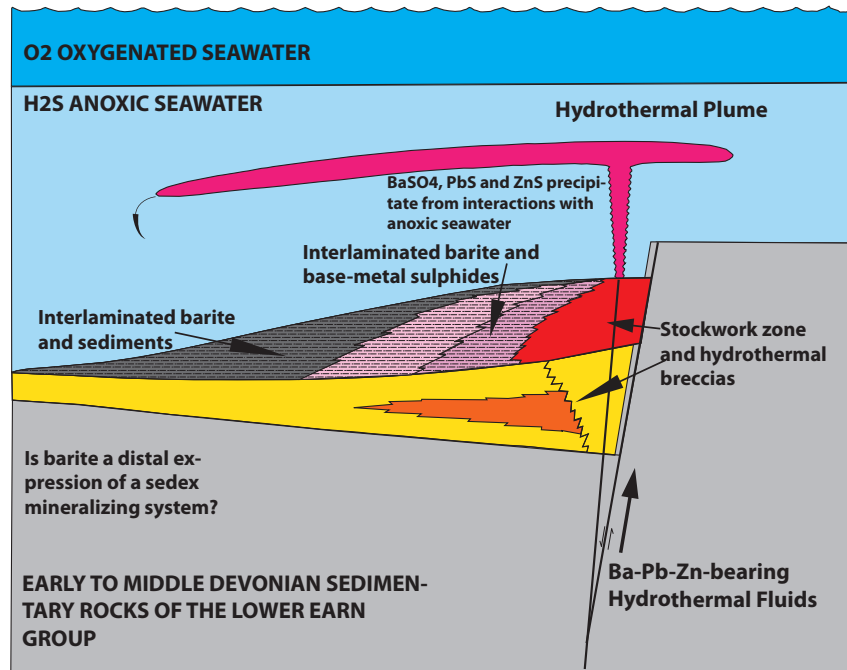


**Figure 1.1: Idealized cross-section of a vent proximal SEDEX deposit (modified from Goodfellow and Lydon, 2007).**

The composition, temperature and oxidation state of the fluids that formed SEDEX deposits are still debated even though the models for their genesis were hypothesized nearly thirty years ago. There are no modern-day analogues forming on the seafloor. Proterozoic Australian SEDEX deposits have no observable vent-complex, have abundant siderite ( $\text{FeCO}_3$ ) and are considerably more metal-rich than vent-proximal SEDEX deposits such as those found in the Selwyn Basin in Canada.

It is believed that Australian SEDEX deposits, which contain virtually no barite; were formed by oxidizing, metalliferous brines migrating through stratigraphy and buffered by oxidized sedimentary packages in the McArthur and Mount Isa Basins, which then interacted with a reduced, carbonaceous shale package to precipitate Pb and Zn sulphides in favourable horizons (Cooke et al., 2000). Similarly, it has been suggested that vent-proximal SEDEX deposits in the Selwyn Basin are thought to be precipitated from highly reducing, acidic, Pb-Zn-Ba-bearing hydrothermal brines which were buffered by reduced shale lithologies (Goodfellow and Lydon, 2007). These Pb-Zn-Ba bearing-fluids then reached the seafloor and interacted with anoxic seawater which was the source of sulphide and sulphate in these deposits (Cooke et al., 2000; Goodfellow and Lydon, 2007).

The vent-proximal SEDEX model postulates that mineral zonation about

the vent-complex would result in the formation of interlaminated sulphides and sulphates close to the vent. Distal to the the sulphides and barite would be interlaminated barite and basinal sediments (Goodfellow and Lydon, 2007). Therefore, by this model, barren barite deposits (i.e. barite with no associated ore-bearing minerals) may be in relatively close proximity to a metaliferous sequence of Pb and Zn sulphides which has been used as an exploration tool by mining companies.

## 1.2. Rationale and objectives of study

In Canada, the Selwyn Basin (Fig. 1.2), which is located in both the Northwest and Yukon Territories contains several economic Zn-Pb-Ag resources that have been assigned to the vent-proximal SEDEX deposit type. Additionally, the Selwyn Basin is host to a number of barite occurrences not associated with sulphides, whose origins are unknown (Axe, Bunk One, Bunk Two, BA, Wise, Anita, NAFCAC-1, NAFCAC-2, Harp, Cowan in the NWT, Walt/Tyrala/Hess in the Yukon).

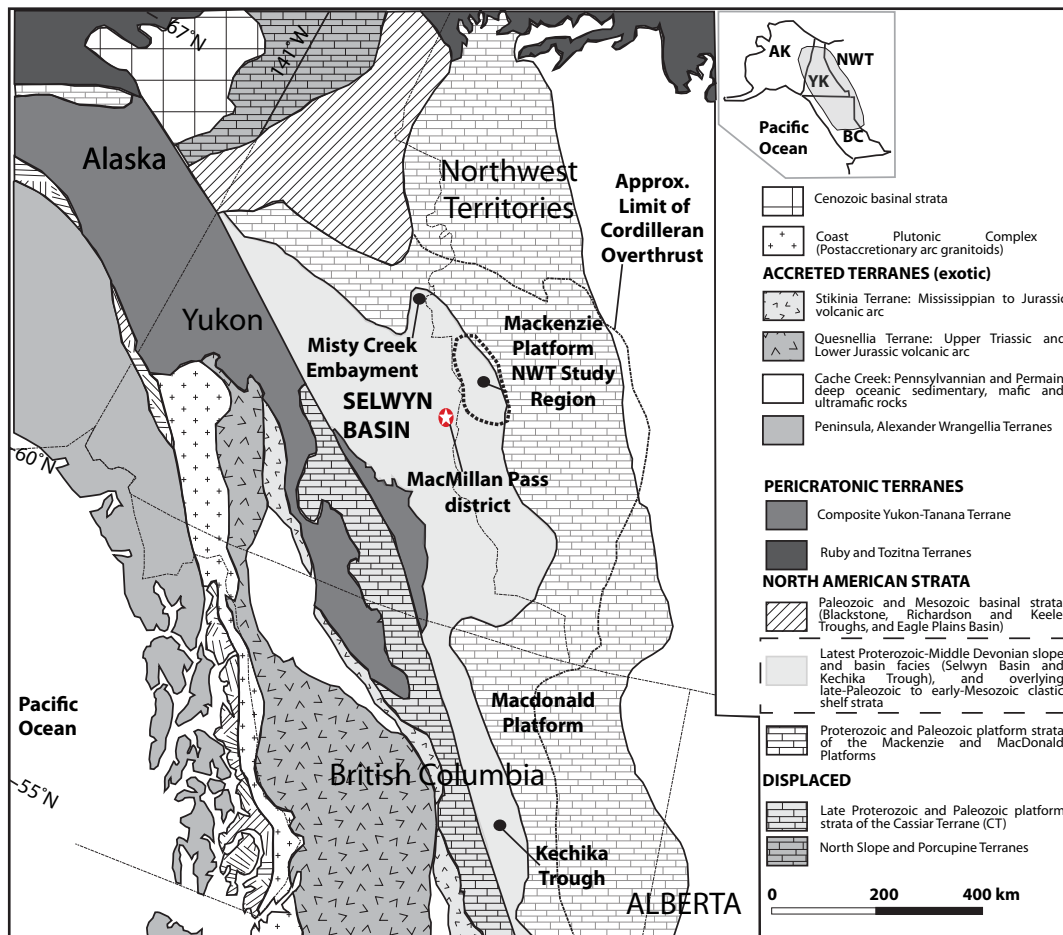


*Figure 1.2: Regional geology of the northern Cordillera in the Northwest Territories, Yukon, British Columbia and Alaska (modified from Mair et al., 2006).*

*The study area in the NWT is circled in the dashed line and the MacMillan Pass district in the Yukon is indicated with a star.*

The major vent-proximal deposits of the Selwyn Basin are thought to have formed in the late Devonian-early Mississippian based on the age of host lithologies (Goodfellow and Lydon, 2007). The barren sediment-hosted barite sequences that are found in both the NWT (Fernandes et al., 2010) and in the MacMillan Pass District, Yukon are interpreted to be in host rocks of the same age (e.g. Turner and Goodfellow, 1990).

The objectives of this study were as follows:

1. To visit and describe barite-bearing occurrences from a wide geographic area within the Selwyn basin. In the MacMillan Pass district, Yukon, barite occurrences are close to known SEDEX-type mineralization. In the NWT there are no currently known vent-proximal SEDEX occurrences. These barite occurrences were geologically mapped and stratigraphic sections were measured through the units where possible.
2. To analyze the major, minor and trace element (including rare-earth elements) signatures of the following groups of samples:
  - Devonian-Mississippian barren sedimentary host rocks
  - Samples from the NWT study area with no sulphides constituting a ‘barren barite’ dataset.
  - Samples from the Yukon study area that have some sulphides associated with them and are considered to be a ‘mineralized barite’ dataset.
3. To analyze the stable isotope geochemistry of sulphates and sulphides to understand their possible fluid source(s) and to compare results from the NWT with those from the Yukon.
4. To sample drill core from the Hess barite (MacMillan Pass) occurrence to investigate the relationship between barite and sulphide mineralization.
5. To attempt to date pyrite mineralization in the Hess barite drill core using Rhenium-Osmium (Re-Os) isotope geochronology in order to constrain the timing of the ‘mineralized’ barite at the Walt/Tyrala/Hess barite occurrences and to compare results with the age of ‘barren’ barite sequences in the NWT.

## CHAPTER TWO: GEOLOGICAL BACKGROUND, FIELD METHODS AND RESULTS

### 2.1 Background geology of the NWT study area

One of the best preserved and documented examples of an epicratonic sedimentary sequence is found in the Selwyn Basin in northwestern Canada. This is interpreted to have formed on the passive margin of Ancient North America as a result of erosion of the crystalline basement during continental breakup initiated at ~760 Ma (Eisbacher, 1981) (Fig. 2.1). The oldest rocks exposed in the Selwyn Basin consist of a thick (4-6 km) sequence of Hadrinian-Cambrian clastic sedimentary rocks of the Windermere Supergroup (Eisbacher, 1981). However, the Windermere Supergroup may also represent the basement to the Selwyn Basin and current work by the Yukon Geological Survey will refine its regional setting.

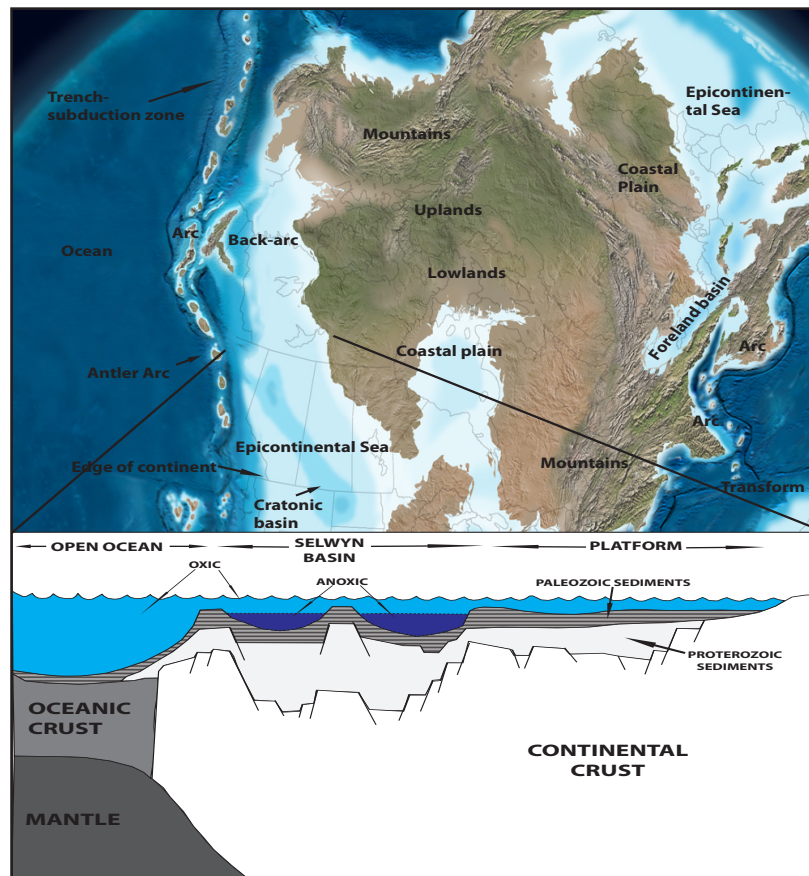


*Figure 2.1: Paleographic reconstruction and interpretation of the North American continent during the late Devonian (modified from Blakey, 2003), Inset: cross-section of the Western passive continental margin of North America during the late Devonian (adapted from Goodfellow and Jonasson, 1984; Hanor, 2000)*

The Windermere Supergroup rocks are overlain by deep-water Cambrian-Ordovician carbonate rocks of the Sekwi Formation, which in turn are overlain by late Ordovician-Silurian basinal facies chert and shale of the Road River Group (Cecile, 1982; Gordey et al., 1982). The basinal sedimentary facies is bounded by the Mackenzie and Macdonald carbonate platforms to the east and north, and dissected by the intrabasinal shelf facies of the Cassiar Platform in the south-central part. The regional stratigraphy is illustrated in Figure 2.2.

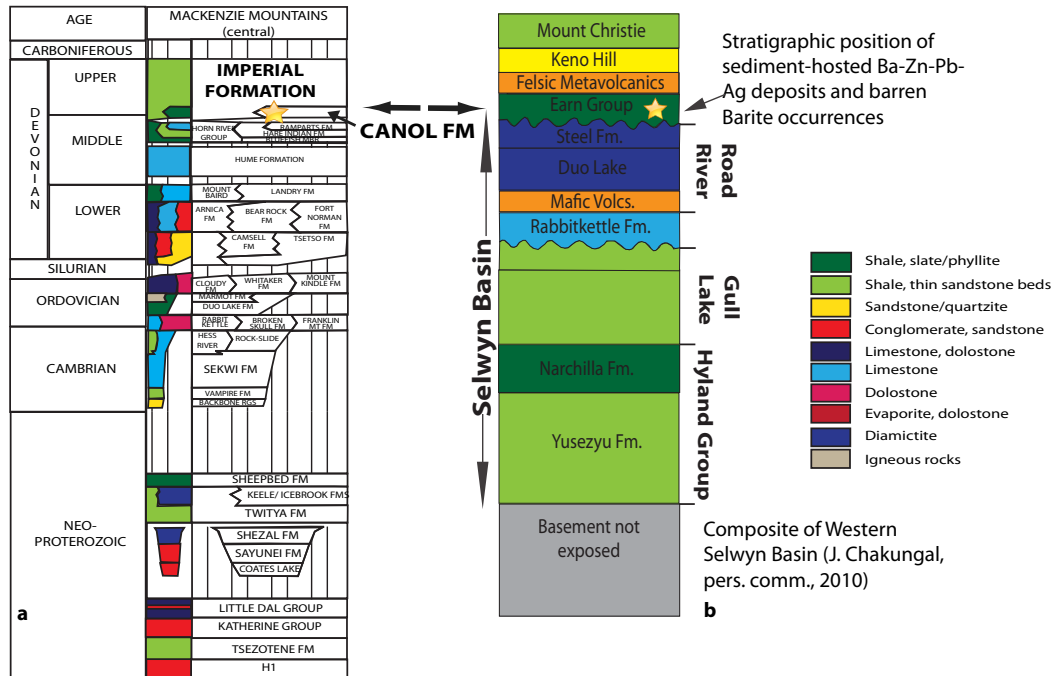


**Figure 2.2:** (a) *Regional stratigraphy of the Mackenzie Mountains (modified after Dewing et al., 2006).* (b) *regional stratigraphy of the western Selwyn Basin (modified after J.Chakungal, pers. comm., 2010)*

Sedimentation changed dramatically in the late Devonian when transgressive shales covered the platform and thick sequences of basin-derived clastic sediments accumulated in a number of submarine fan complexes to the west (Gordey et al., 1982). This was followed by a sequence of arenites and debrites deposited in the early Mississippian. This group of Devonian-Mississippian rocks was first formally defined as the Earn Group in the Nahanni, Sheldon Lake, Niddery Lake and Sekwi Mountain map areas by Gordey et al. (1982). They divided the Earn Group into a lower and an upper unit, with the lower consisting of basinal siliceous shale, mudstone and shaley siltstone, and the upper portion containing coarser-grained turbiditic siliciclastic rocks.

The units covered for this study are the sedimentary rocks belonging to the Earn Group. The Earn Group is subdivided into the lower Earn Group and the upper Earn Group, and more specifically as the Canol and Imperial Formations respectively (Fig. 2.3). The Canol Formation consists of a package of cherty mudstones, black, siliceous shales and grey siltstones that often weather to a characteristic silver colour. The Imperial Formation which unconformably overlies the Canol Formation comprises coarse-grained, brown debrites and sandstones.

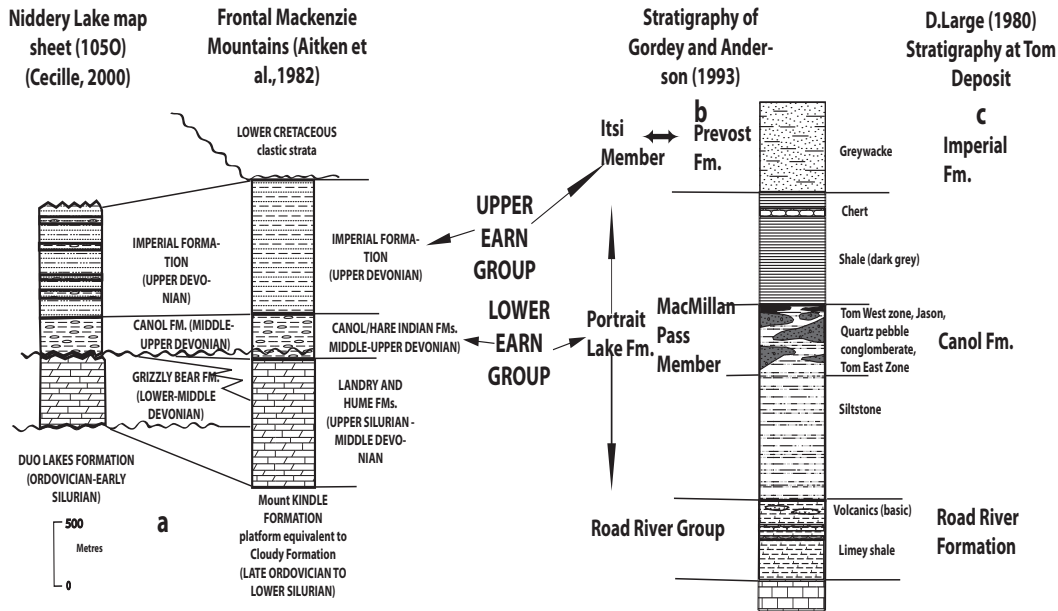


**Figure 2.3:** (a) Earn Group Stratigraphy in the Selwyn Basin and Frontal Mackenzie Mountains (modified after Aitken et al., 1982; Cecile, 2000). (b) Earn Group stratigraphy in the MacMillan Pass District (modified after Gordey and Anderson, 1993). (c) Earn Group stratigraphy at the Tom SEDEX deposit (modified after Large, 1980)

## 2.2 NWT field results

Two seasons of field work in the Mackenzie Mountains were completed in the summers of 2009 and 2010. The occurrences that were investigated are plotted in Figure 2.4.

In 2009 stratigraphic sections were measured across six barite sequences hosted by the Earn Group to constrain their stratigraphic position and the distribution of various barite textures within each section. Detailed sampling was conducted along each section and at an additional site (BA) which did not have sufficient outcrop for a measured section.

Field work in 2010 focused on the region between the Bunk One, Axe and Bunk Two showings which represents an 80 km NW-SE corridor of exposure of the both the Canol and Imperial Formation (red box in Fig. 2.4). This reconnaissance work was carried out to find new barite exposures, measure stratigraphic sections, and determine the lateral extent of the barite horizon within the Canol Formation.

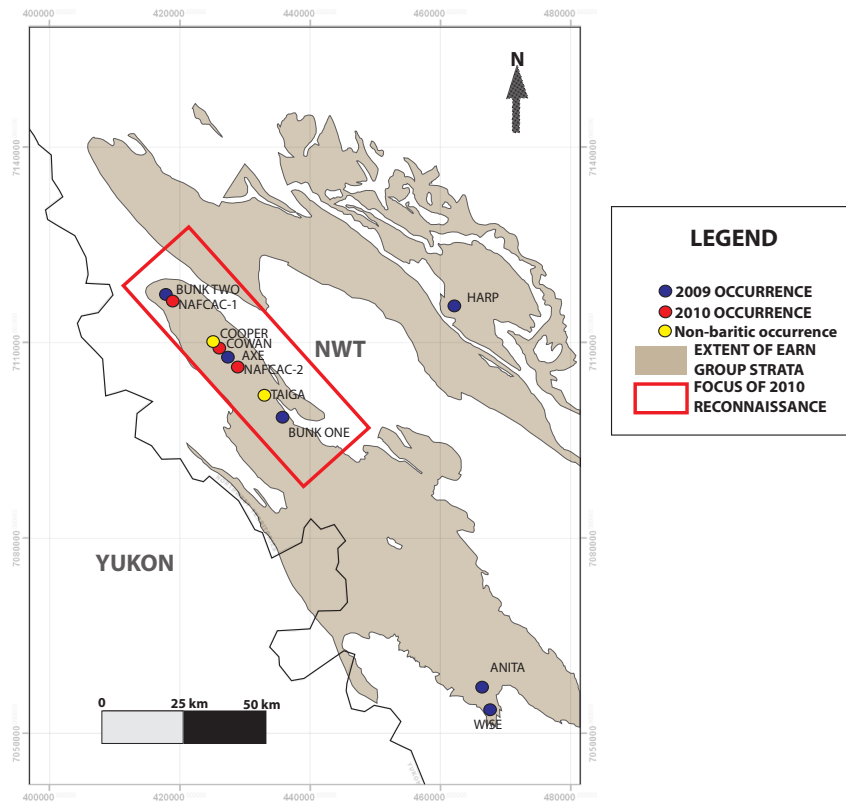


**Figure 2.4:** Field map showing extent of Earn Group outcrop in the study region, locations of barite occurrences (blue and red circles) and other samples (yellow circles). Red box outlines an ~80 km long focus of reconnaissance during the summer of 2010.

### 2.2.1 Non-barite bearing Canol Formation:

General geology of Canol Formation sediments below barite horizons:

A stratigraphic section from the bottom to top of the Canol Formation was not measured. A section measured by Gordey and Anderson (1993) showed the Canol Formation to be up to 850 m thick. During reconnaissance in 2010, it was found that Canol Formation rocks exposed downhill from baritic showings are composed almost entirely of brown-grey, thin to thick bedded siliceous shale and mudstone.

These Canol Formation sediments from the lowermost exposed part of the Earn Group are rich in hydrocarbons which give them a characteristic efflorescent purple coating (Plate 2.1a). Bedding is deformed and marked by gentle, open folds (Plate 2.1b).

Taiga (Section 1; Appendix A):

The Taiga section was measured even though it had no barite because it is spatially associated with barite horizons. The lowermost unit in the section consists of grey-weathered cherty mudstone similar to that found at the base of the Axe occurrence. Most of the section consists of orange-weathered black shale although a small, 1m thick limestone concretion was observed. The lithology changes abruptly back into silver-grey, platy shale associated with the top of the Canol Formation at 51 m in the section. Samples in this section were selected to compare their geochemistry with those found in barite occurrences.

Cooper:

There are two lithotypes at this location, a 'crinkly', strongly foliated mudstone with abundant mm-sized quartz and strongly altered clasts that are often replaced by fine-grained pyrite (Plate 2.1c), and a black, laminated shaley mudstone with a distinct, pen-shaped weathering profile. The pyritic, diamictic mudstone was previously undocumented in the Canol Formation, and was sampled for further study and analytical work.

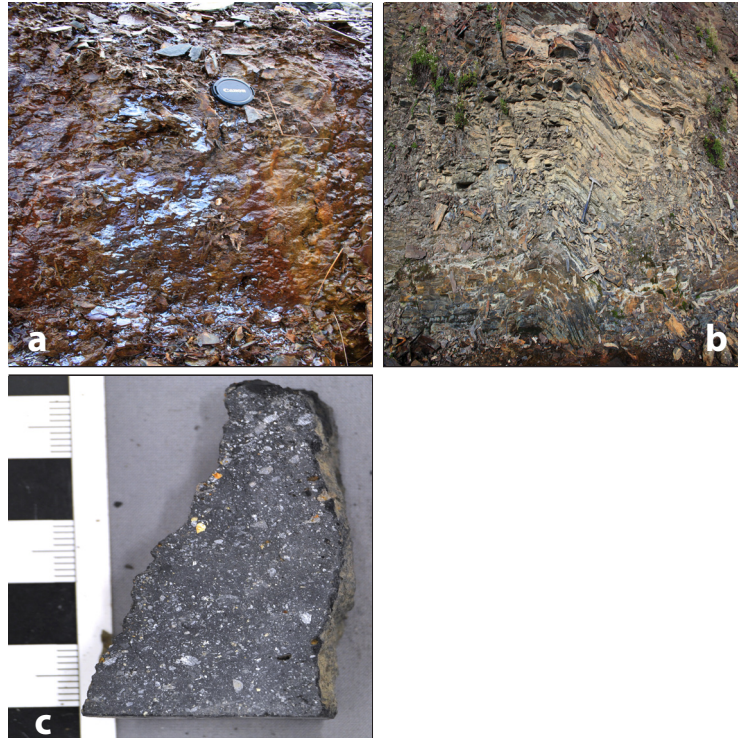


***Plate 2.1: (a) efflorescent hydrocarbons seeping from Canol Formation sediments stratigraphically below barite horizons, (b) Folding and deformation within Canol Formation shales and siltstones stratigraphically below barite horizons, (c) Diamictite from Cooper occurrence***

### *2.2.2 Barite occurrences with measured sections*

Anita (Section 2; Appendix A):

The Anita showing is found at the top of a hill (Plate 2.2a) and the average strike and dip of the bedding is  $155^{\circ}/14^{\circ}$  SW. The lowermost stratigraphic unit underlying the barite-bearing sequence at Anita is a resistant, brown, laminated siliceous mudstone unit corresponding to the lower parts of the Canol Formation. This is overlain by a sequence of thin-bedded, non-calcareous, silvery-grey white shale at the base of the section. In the lower 3 m of the section barite appears as rare mm-scale nodules with no particular orientation in a dark-grey mudstone matrix. Barite concentrations increase upward in the section and textures vary repeatedly from coarser-grained, nodular to finer-grained, laminated barite within the mudstone and siltstone in a repeating sequence. 25 m of talus consisting of sandstone and debrite occurs above the shale and mudstone before the Imperial Formation outcrops.

Wise (Section 3; Appendix A):

The base of the measured stratigraphic section is composed of a 5.5 m thick sequence of black, finely-laminated, carbonaceous shale. At 2.5 m above the base of the section, a small (0.2 m) interbed of coarser-grained cherty fragments in a grey siliceous matrix and a brownish grey debrite occurs. Overlying the debrite is 80m of talus consisting of siltstone with locally calcareous intervals. Approximately 10 m below the lower contact of the barite-rich beds, black non-calcareous shale is exposed. This is in direct contact with greyish-black, laminated, locally siliceous shale and siltstone that contains barite (Plate 2.2b). The barite beds have a repeating sequence that goes from larger (>1 mm), deformed barite crystals to predominantly microcrystalline barite laminations and lesser, smaller (~0.2 mm) barite nodules (Plate 2.2c). The laminated subunits increase in thickness upward in the section from tens of centimetres to metres. The barite-bearing section has a composite thickness of approximately 20 m and has an average bedding strike and dip of 205°/10° NW. This unit is then unconformably overlain by brownish-grey, blocky sandstones tentatively interpreted as the Imperial Formation, which are exposed in a small outcrop approximately 50 m west of the section line.

Bunk-One (Section 4; Appendix A):

The Bunk One showing consists of a 'fining-up' sequence with the bulk of the barite being hosted in two brown-weathering, shaley siltstone units (25 - 33 m) at the bottom and in the middle of the section. The shaley siltstone is less resistant to weathering than other sediment-hosted barite showings and dominates the talus underlying it. A nodular barite subunit (31 - 33.5 m) overlies a 'wispy barite' subunit. The lithology of the upper parts of the sequence (40 - 50 m) is dominated by grey-weathering shale that contains relatively less barite, but displays much finer grain-sizes and a high concentration of laminations. Nodules in this section are highly deformed with long axes oriented along shale laminations. The outcrop exposure ends at roughly 49 m. However, nodular barite in shaley units dominates the talus until the contact with the overlying Imperial Formation is reached about 25 m - 30 m above the end of the section.

NAFCAC-2 (Section 5; Appendix A):

NAFCAC-2 was discovered during reconnaissance work in the second field work season during a traverse between Axe and Bunk-one. The entire section is 72 m thick, with an average bedding dip and strike of 131°/39° SW. While it may repre-

sent the largest barite showing investigated, it also contains a non-baritic section (39.3 – 62.7 m) which is also the thickest measured. There are three distinct subunits in this section. The lower third (0 – 22.5 m) consists of thinly-laminated to massive mudstone containing sparse, 0.2 – 1 cm barite nodules which are sometimes deformed and aligned along laminations. The top third is made up of interlaminated, fine-grained barite and grey siltstone. These are separated by a barren shale subunit and an unusually large, 6m thick, limestone concretion. All lithologies exposed correspond to the Canol Formation.

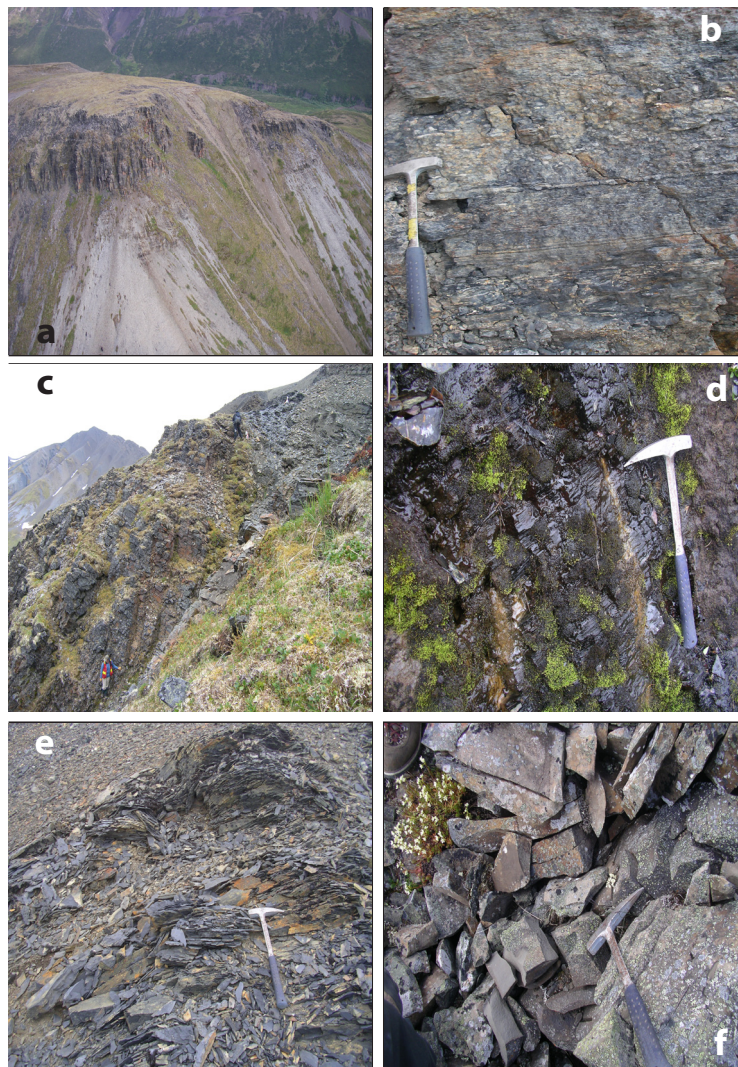


***Plate 2.2: (a) outcrop view of Anita occurrence, (b) baritic sediments at Wise, (c) outcrop view of the Axe section, (d) siliceous mudstone underlying Axe, (e) non-baritic shale at Axe, (f) Imperial Fm at Axe***

Axe (Section 6; Appendix A):

The Axe showing is located between the Bunk One and Bunk Two barite showings. All three showings are on a trend and appear to represent the same stratigraphic level in the Canol Formation (Plate 2.2c), near the upper contact with the Imperial Formation. A section was measured from the non-baritic siltstone, mudstone and chert unit at the base, through a 38 m thick barite section into overlying, weakly baritic rocks whose upper contact with non-baritic rocks is obscured by talus.

Underlying the Axe showing is a black siliceous cherty mudstone (Plate 2.2d) which is overlain by dark grey, very thinly bedded Canol Formation shale. Barite-bearing units at Axe are separated by two discrete black, carbonaceous, platy shale units containing no barite (Plate 2.2e). These two shale units and an almost identical shale unit that directly overlies the section belong to the Canol Formation and hence constrain this showing to the upper section of the lower Earn Group. The average bedding strike and dip throughout the section are 130 - 145°/40 - 45° SW respectively. There is only one discernable 'fining-up' sequence of barite textures with an increase in laminated microcrystalline barite content upwards relative to nodular barite. The laminated barite and mudstone unit from 21 - 34 m in the section is the thickest baritic subunit mapped in all the showings. The Imperial Formation outcrops roughly 50 m above the section (Plate 2.2f)

Bunk-Two (Section 7; Appendix A):

Although the host rock lithologies at the Bunk One and Bunk Two showings (~26 km apart) are similar, there appears to be a reversal in the sequence of observed barite textures going from bottom to top of the section. The grain-size of the barite crystals increases going upward in the section and the barite becomes more nodular as opposed to laminated. The beginning of the section is a ~ 9 m thick thinly-laminated mudstone interlaminated with microcrystalline barite. Most of the other barite-bearing units in the section are siltstones. Limestone concretions ranging from tens of centimetres up to 1 m wide are found. At 36 m, overlying the limestone nodular unit, the outcrop is obscured by talus composed of predominantly black, carbonaceous shales of the Canol Formation. The Bunk Two showing is contained entirely within the upper part of the Canol Formation. The Imperial Formation outcrops approximately 25 m vertically above the Canol Formation shale capping the barite section.

NAFCAC-1 (Section 8; Appendix A):

NAFCAC-1 was found on the southeast side of the hill hosting the Bunk-Two showing during reconnaissance in the second field season. It is 46 m thick (slightly smaller than Bunk-Two) and is similar to Bunk-Two in that it has 'reversed' barite morphology with a trend from laminated to nodular barite upward in section and it also has two limestone concretions, all of these lithologies are contained within the Canol Formation. Beds in this section have an average dip and strike of  $307^{\circ}/29^{\circ}$  NW, which is in the same orientation as sedimentary bedding at Bunk-Two. The Imperial Formation can be found roughly ~ 50 m vertically above the occurrence, after an area of no exposure.

Harp (Section 9; Appendix A):

The Harp showing is unique among all the visited occurrences. It is the only occurrence found in a river bank (i.e. in a topographic low). The measured section shows no discernable evolution of barite textures and most barite mineralization at this showing appears to be structurally controlled.

The showing is a continuous outcrop of steeply dipping beds ( $60^{\circ}$  -  $70^{\circ}$ ) of siliceous siltstone, shale and an 8 m thick carbonate unit, all of which are equally resistant to weathering. Alternating thin beds (1 – 10 cm) of siltstone and very thin (0.3 - 0.8 cm) black, shaley layers are present (Plate 2.3a). From 11.25 m to 11.75 m, there is an off-white, barite vein that appears to be associated with a fault. Lithologies are consistently the same until 28.1 m up-section where barite appears. This barite is concentrated along bedding planes and bears no resemblance to the barite documented at any of the other showings in this study. It appears to be associated with veins and structures related to a fault gouge at 33.5 m. There is a thick (7.5 m) carbonate sequence that overlies the fault. It can be subdivided into a lower carbonate nodule subunit which contains disseminated microcrystalline barite, and an upper, well-bedded limestone with interlaminated microcrystalline barite that is texturally comparable with those documented at other sections.

These laminations increase in thickness until the contact with an overlying siltstone unit. From 42 - 46 m, the siltstone unit also contains thin laminations of barite. The siltstone is in direct contact with black shale that contains no barite. About 1 km upstream from the Harp barite showing is an outcrop of Canol Formation containing abundant hydrozincite ( $Zn_5(CO_3)_2(OH)_6$ ) on bedding and fracture surfaces (Plate 2.3b). This hydrozincite occurs approximately 25 m stratigraphically above the lower contact of the Canol Formation and the upper surface of the

Hume Formation limestone.



**Plate 2.3: (a) outcrop view of Harp showing, (b) efflorescent blue hydrozincite coating Canol Formation (Sample 09NF517J).**

### *2.2.3 Barite occurrences with no measured sections:*

#### **Bedded Barite (BA):**

The BA (short for Bedded Barite) showing is unusual in that it is underlain by greyish-white, fossiliferous carbonates which are thought to belong to the Devonian Nahanni Formation. The contact, while not exposed, is interpreted to be faulted (Roots and Martel, 2008). The few outcrops observed at this site have predominantly fine-grained, laminated barite with abundant deformation manifested by small-scale folding (Plate 2.4a). In some samples, barite laminations are on the order of 2-5 mm, and are interlaminated with a dark, grey mudstone that has microcrystalline barite nodules scattered throughout.

#### **Cowan:**

The Cowan barite occurrence was discovered during reconnaissance sampling in the 2010 field season. It is made up mostly of a single 3 – 5 m thick horizon consisting of grey weathering, platy siltstone interlaminated with fine grained barite and sometimes, 2 – 6 mm sized barium mineral nodules. This horizon is partially exposed for roughly 70 m along strike (143°/30° SW, Plate 2.4b). Downslope of the baritic horizon, there is an abrupt change in lithology to black shale and mudstone of the Canol Formation with little to no barite at all. The Imperial Formation only outcrops 300 m west of the Cowan occurrence.



**Plate 2.4:** (a) interlaminated barite and siltstone from BA occurrence, (b) outcrop view of exposed baritic horizon at Cowan occurrence looking ~NW.

### 2.3 Summarized NWT field results

The barite occurrences in the NWT are hosted primarily in shale, siltstone and mudstone in the upper part of the Canol Formation, underlying the debrites and turbiditic siliciclastic rocks of the Imperial Formation (Fig 2.5). The showings typically occur in black, siliceous, carbonaceous shale and siltstone. Strata in the measured sections are moderately to steeply dipping, and range from 22 -72 m true total thickness. All barite occurrences (except Harp) can be found on top of, or on the side of a topographic high.

Barite displays a variety of grain sizes and textures in all the showings. Lower parts of showings are composed primarily of laminated black mudstone with rare wispy sub-millimetre crystals of white barite. These subunits grade upwards into beds dominated by sub-centimetre barite nodules. The long axes of these nodules are commonly oriented along laminations and display varying degrees of deformation. Barite nodule size generally increases to 1 - 3 cm towards the top of these subunits. The second subunit consists of grey, very thinly-bedded (0.2 - 1 cm) siltstone/shale with 1 - 2 mm interlaminations of microcrystalline barite. There is a systematic change from nodular to deformed-nodular to bedded barite (and sometimes a reappearance of nodular textures) up-section (except at Bunk Two and NAFCAC-1) and a general thickening of subunits. Barite crystals in the laminations are smaller than those in barite nodules.

Often overlying sections, and sometimes sandwiched between baritic units ,

is the barite-poor, silvery grey, recessive shale of the Canol Formation. The contact with the Imperial Formation is not typically exposed, but occurs within 5 - 35 m of the top of barite sections. Canol Formation sediments stratigraphically below the baritic horizons are composed of siliceous fine-grained shale and mudstone that are often associated with hydrocarbons.

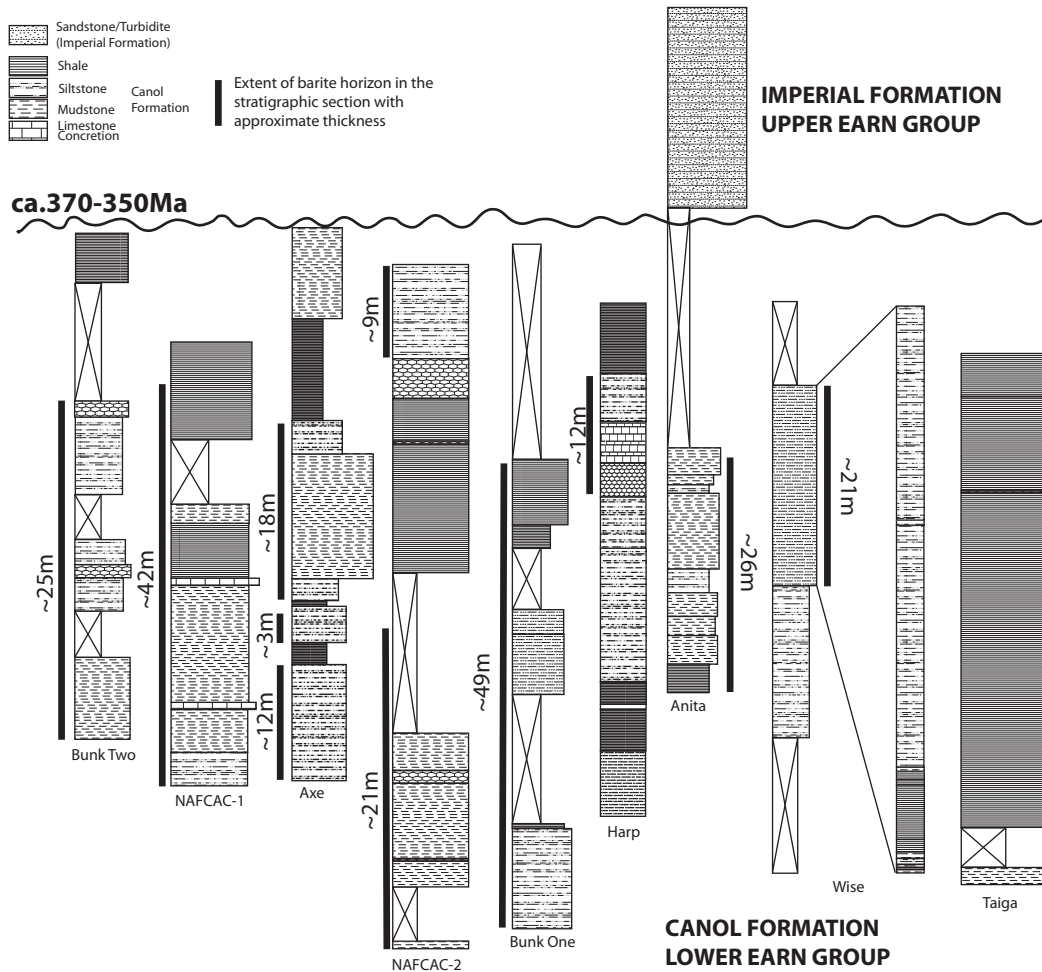


**Figure 2.5:** *Compiled stratigraphic sections measured in this study constraining sediment-hosted barite within the uppermost parts of the Canol Formation. Baritic subunits within stratigraphic sections are indicated with thick black lines. Detailed stratigraphic sections with individual sample locations and coordinates of each section are found in Appendix A.*

## 2.4 Geological setting of the Yukon study area

The Walt/Tyrala/Hess sediment-hosted barite occurrences are found in the MacMillan Pass District, east Yukon and are located in map sheet 105O (Fig. 2.6). Abbott (1982) divided the MacMillan Fold Belt (MFB) into three tectonostratigraphic do-

mains (North, Central and South blocks) based on style of the Mesozoic structures present and distribution of the Silurian-Devonian units. The region is dominated by west-trending tight folds and steep faults. In the Central block, the lower Earn Group stratigraphy overlies basaltic flows and volcanoclastic rocks as young as late-middle Devonian (Turner and Rhodes, 1990).

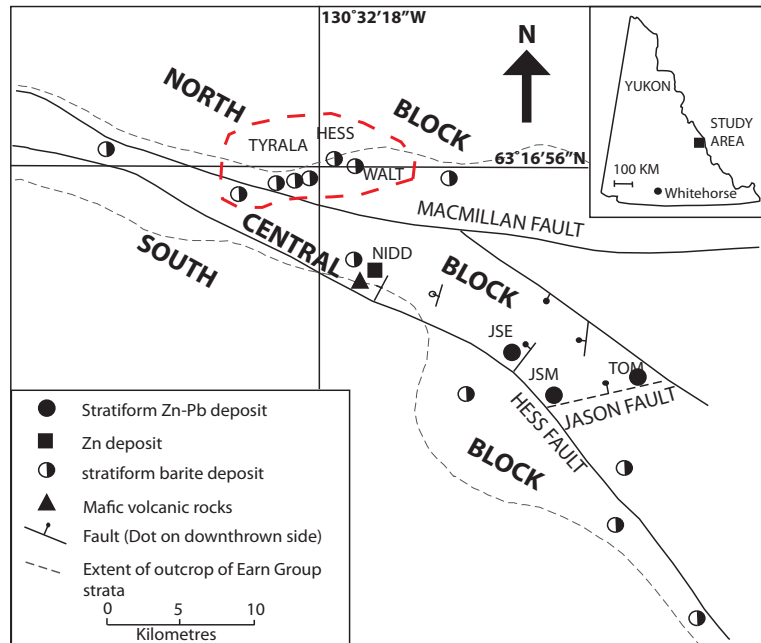


**Figure 2.6: District map of the MacMillan Pass region showing major structural blocks, trends and deposits/showings. Area encircled in dashed line is the Yukon study area. JSE = Jason Endzone, JSM = Jason Main zone (modified after Turner and Goodfellow, 1990).**

The sediment-hosted barite showings correspond to Yukon MINFILE 1050 021 and 105 O22 and are located within the Walt and Tyrala claim blocks. These barite occurrences were drilled by Baroid of Canada in 1980, mapped and sampled by Cominco and later re-examined by NDU resources because the samples had anomalous levels of Zn, Pb and Cu.

The sedimentary rocks hosting barite mineralization in the Walt/Tyrala/Hess occurrences also belong to the Earn Group. The lower Earn Group; known as the Portrait Lake Formation in the Yukon consists of a package of cherty mudstones, black, siliceous shales and grey siltstones that often weather to a characteristic silver colour. The upper Earn Group which unconformably overlies the Portrait Lake Formation; known as the Prevost Formation in the Yukon and more recently called the Itsi Member of the Earn Group (Abbott and Turner, 1990); comprises coarse-

grained, brown debrites and sandstones.

Abbott et al. (1987) recognized three informal units within the lower Earn Group in the MacMillan Pass District: a lower member of carbonaceous chert, a middle turbidite member, and upper member of carbonaceous siliceous shale. A thick conglomerate unit occurs within the middle turbidite member and reflects the development of a Devonian graben (Abbott, 1982). This conglomerate unit, which has been named the MacMillan Pass Member; is not well-constrained stratigraphically but is thought to occur in the middle of the lower Earn Group (Fig. 2.3b, Gordey and Anderson, 1993). Also restricted to this graben are Silurian and Devonian volcanic rocks, late Devonian faults and upper Devonian stratiform zinc-lead mineralization (Abbott and Turner, 1990). The Walt/Tyrala/Hess occurrences are located along the northern margin of the Central Block, a domain intensely deformed by an imbricate package of south-directed thrust faults (Turner and Goodfellow, 1990). Irwin and Orchard (1990) derived a middle Devonian age for sediments at the Cathy occurrences from conodont biostratigraphy.

Confusion can occur when reading older literature (e.g., Large, 1980) that used NWT nomenclature for the Earn Group in the MacMillan Pass District (Fig 2.3c). For simplicity, Yukon stratigraphic nomenclature is used when describing the geological setting of the barite occurrences in the Yukon study area. However, it is recognized that this terminology is different from nomenclature used in the NWT and that Portrait Lake Formation is interchangeable with the Canol Formation, and that the Itsi Member of the Portrait Lake Formation correlates with the Imperial Formation.

## **2.5 Yukon sediment-hosted barite field results**

Samples were collected from a single drill-hole from Hess during fieldwork in 2009 and a field investigation was conducted on the Walt/Tyrala/Hess occurrences during the summer of 2010. Coordinates of showings and a map of local geology from the Yukon database can be found in Figure 2.7.

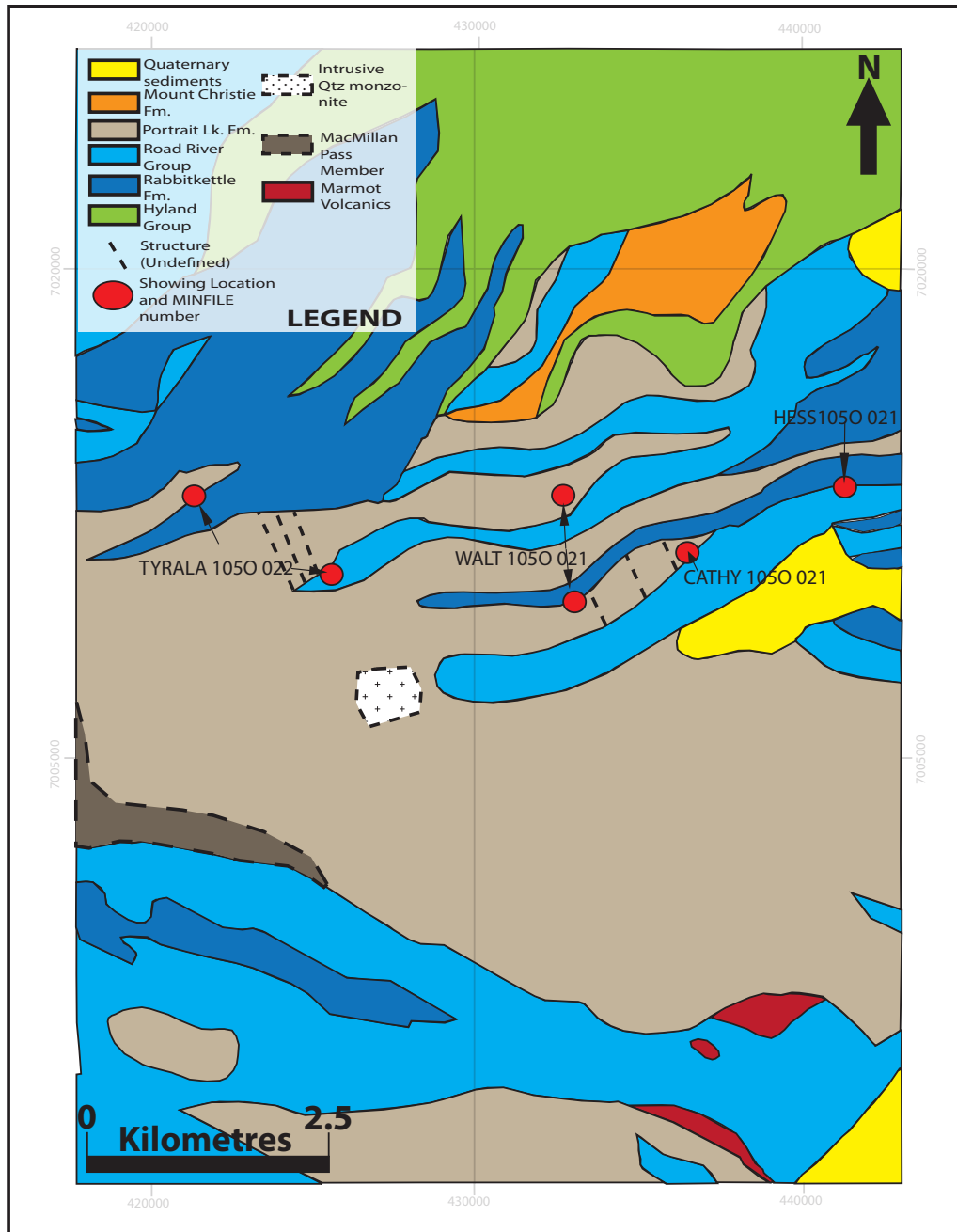


**Figure 2.7:** Geological map of study area, 1:50000 scale, coordinates are in UTM NAD 83 Zone 9, see legend for lithological description (modified from YGS database map).

### 2.5.1 Field relationships

Sediment-hosted barite at all occurrences in the study area occurs within interbedded shale and siltstone of the Portrait Lake Formation, and in massive to brecciated limestone of the Road River Group (stratigraphically below the Earn Group). The

Itsi member (upper Earn Group) is absent in the study area. No visible sulphides were observed in outcrop samples.

Barite that is hosted in the Portrait Lake Formation shale and mudstone occurs predominantly as fine laminations (Plate 2.5a) or in minor, millimetre – sized nodules (Plate 2.5b). Tight to isoclinal folding of barite laminations indicates a pre-fold and thrust deformation origin (Plate 2.5c). Barite laminae vary from 0.5 to 2 mm thick and are dark grey in colour. Barium-enriched laminae in the Road River Group carbonates are dark grey, weather to a pale cream colour and are composed of fine grained barium carbonate and barite (Plate 2.5d). Barite nodules are round, roughly 1 mm in diameter and composed of sub-millimetre, radiating barite crystals which make up a very small portion of samples.

Within the study area, the greater majority of barite deposition occurred within highly altered, carbonate-replaced Portrait Lake sediments (or possibly Road River Group carbonates), and has a marked fault-related structural control punctuated by sharp contacts (Plate 2.5e). Massive, fine to medium grained barium carbonate is the principal component of barite lenses up to 20 m thick that form steep, resistant ridges. Barium carbonate breccias range from pale grey, angular to subrounded and clast-supported, to large subrounded pale grey clasts up to 50 cm in diameter in a fine-grained, dark grey siliceous matrix (Plate 2.5f). Clasts that are composed of fine-grained barium carbonates suggest coeval barium replacement of sediments and brecciation.

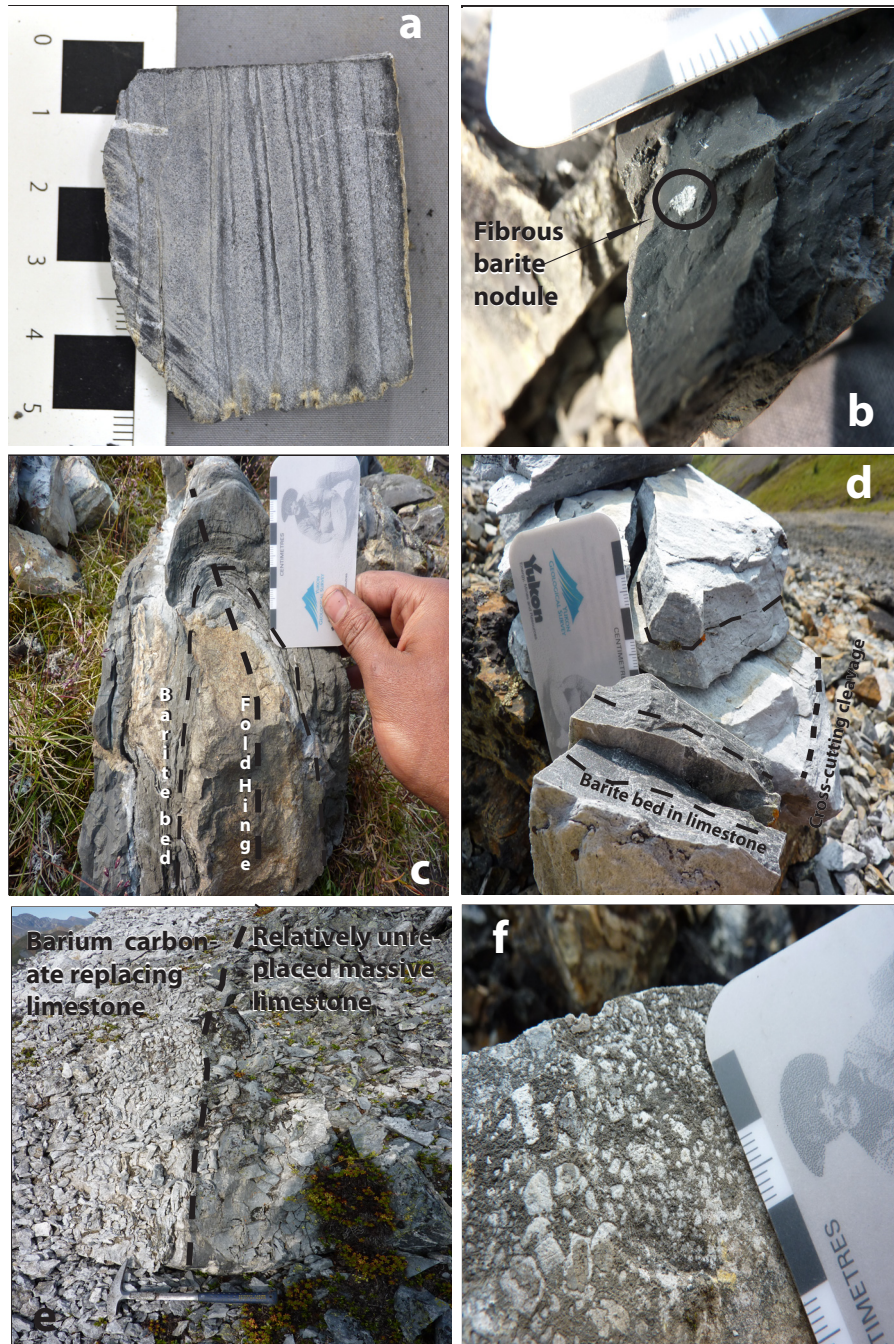


**Plate 2.5:** (a) shale-hosted laminated barite mineralization (sample 10NF42F). (b) shale-hosted nodular barite mineralization (sample 10NF40A). (c) pre-deformation laminated barite wraps around a fold hinge. (d) laminated barium mineralization in Road River Group carbonates at Walt showing. (e) sharp contact between barite replacement front and Road River Group carbonates at Cathy showing. (f) barium carbonate breccias in Road River Group carbonates.

### 2.5.2 Hess Drill Core

Samples were collected from weathered Cominco drill core at the Hess barite occurrence which was drilled to a depth of 105.5 m. Textures associated with barium mineralization are similar to those observed in outcrop.

The Cominco drill hole was collared in deformed and locally brecciated non-calcareous black, siltstone and mudstone of the Portrait Lake Formation (Plate 2.6a). Minimal barite was observed from 0 to 39 m in the hole. Unmineralized siltstone and mudstone units are underlain (39 – 105.5 m) by increasingly altered, brecciated, and carbonate/sulphide/sulphate-rich lithologies.

Some samples have textures identical to barium nodules from the Northwest Territories (Plate 2.6b). However, these nodules effervesce upon reaction with 10 % HCl which indicates the presence of carbonate.

The carbonate units contain barium minerals that exhibit similar epigenetic textures found in outcrop. Barium minerals are intergrown with disseminated sulphides consisting of coarse-grained, euhedral pyrite, medium to coarse-grained, reddish-brown sphalerite and medium-grained, subhedral galena which can occur as 0.5 cm patches and as millimetre-thick veinlets which cross-cut laminations (Plate 2.6c and d). Sphalerite also occurs in these sulphide patches as fine-grained, light honey brown anhedral crystals. One sample (ca. at 88.65 m) has thin silica-rich layers interlaminated with carbonates (Plate 2.6e). Late quartz veinlets also cross-cut all host rocks and mineralization (Plate 2.6f).

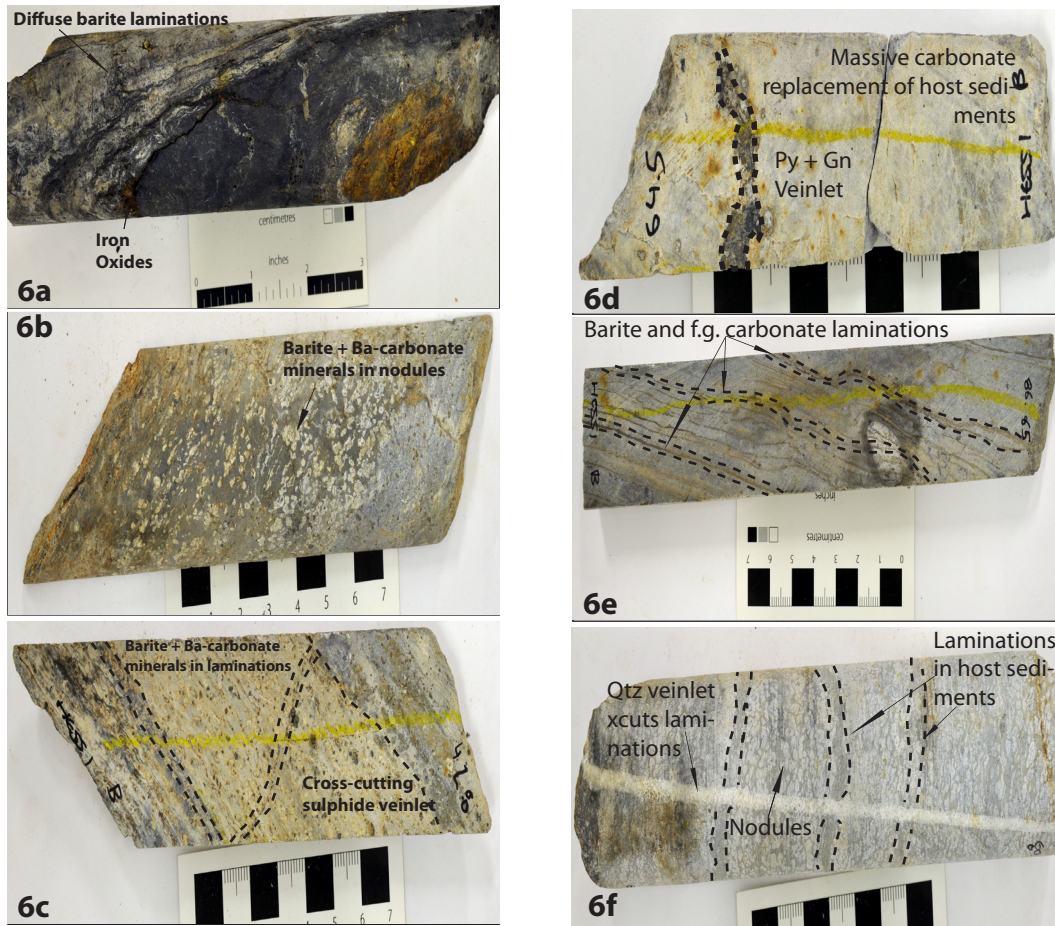


**Plate 2.6:** (a) Portrait Lake Fm. mudstone with minor diffuse barite and iron oxide mineralization (Depth = 27.05 m). (b) barium mineral nodules in Portrait Lake Fm. siltstone (Depth = 42.8 m). (c) laminated barium minerals in Portrait Lake Fm. siltstone (note disseminated pyrite throughout sample, depth = 42.8 m). (d) pyrite + galena veinlet crosscutting massive barium carbonate rich rock (Depth = 64.5 m). (e) quartz + fine-grained brown carbonate laminations in altered sedimentary rock (Depth = 86.85 m). (f) late quartz veinlet cross-cuts laminated barium mineralization (Depth = 89.5 m).

## CHAPTER THREE: ANALYTICAL PROCEDURES

### 3.1. Petrography and EPMA

Hand specimens were cut into thin sections for optical microscopy and petrography. These samples were analyzed by electron microprobe analysis (EPMA) on the CAMECA SX-100 at the University of Alberta, Edmonton, Alberta to determine the chemical composition of the minerals. The microprobe was operated at 20 kV accelerating voltage, 20 nA probe current and 1 micron beam diameter. The techniques and standards for measurement of barite and barium-silicate composition were modified from those of Moro et al. (2001). Standards used for analyzing barite were: apatite for P, barite for Ba and S, diopside for Ca and Si, forsterite<sub>93</sub> for Mg, hematite for Fe, sanidine for K and strontianite for Sr. Standards used for Ba-silicates were: albite for Na, barite for Ba, diopside for Ca and Si, forsterite<sub>93</sub> for Mg, hematite for Fe, Mn<sub>2</sub>O<sub>3</sub> for Mn, pyrope for Al, rutile for Ti, sanidine for K and strontianite for Sr. Standards used for sulphides in Hess drill core were: Sb-metal for Sb, Sn-metal for Sn, Bi-metal for Bi, Pyrite for Fe and S, sphalerite for Zn, W-metal for W, Cu-metal for Cu, galena for Pb and Ag-metal for Ag. None of the sulphides analyzed contain any detectable Bi, W or Te so these elements are omitted from results. Average EPMA detection limits for all analyzed elements are presented in Table 3.1 for barite, Table 3.2 for silicates and 3.3 for sulphides.

Sulphate	Average Detection Limit (ppm)			
	Ba	Ca	Sr	SO <sub>3</sub>
NWT laminated barite	573	111	559	377
NWT nodular barite	573	111	559	377
Yukon barite	572	111	552	377

*Table 3.1: Average detection limits for EPMA on NWT laminated barite, NWT nodular barite, Yukon barite.*

Silicate mineral	Average Detection Limit (ppm)									
	Na	Mg	Al	Si	K	Ca	Ti	Mn	Fe	Ba
Hyalophane	338	320	241	280	422	353	217	574	738	708
Cymrite	376	359	268	280	415	367	234	630	786	790
Albite	405	278	213	276	369	315	179	466	643	563

*Table 3.2: Average detection limits for EPMA on silicates*

Sulphide mineral	Average Detection limit (ppm)								
	S	Fe	Cu	Zn	As	Ag	Sn	Sb	Pb
Pyrite	503	365	383	462	489	430	818	793	2396
Sphalerite	497	301	391	531	648	456	886	839	2388
Galena	418	414	468	553	575	729	1125	1153	2619
Kesterite	461	330	428	647	610	564	929	0	2248
Geocronite	435	405	462	546	568	684	1073	1128	2581
Franckeite	442	404	463	547	570	688	1082	1472	2504

*Table 3.3: Average detection limits for EPMA on Hess drill core sulphides*

### 3.2 Stable isotope geochemistry of sulphates and sulphides

Barite mineral separates were obtained by drilling laminations and nodules into a fine-grained powder using a steel-tipped drill. Sulphide mineral separates were produced by rough crushing and subsequent hand-picking of pyrite, galena and sphalerite grains from Hess drill core.

The sulphur isotope geochemistry of sulphates and sulphides were analyzed at the Isotope Science Laboratory at the University of Calgary, Alberta using the technique of Grassineau et al. (2001). The sulphur isotope ratios of barite and sulphides were determined using Continuous Flow-Elemental Analyzer Isotope Ratio Mass Spectrometry (CF-EA-IRMS). The instrumentation comprises a Carlo Erba NA 1500 elemental analyzer interfaced to a VG PRISM II mass spectrometer (Giesemann et al., 1994). Samples are packed in tin cups, which are dropped by auto sampler, onto a quartz tube combustion reactor. The temperature of this column is maintained at 1020 °C and ‘flash-combustion’ is achieved by injecting a pulse of O<sub>2</sub>(gas) exactly at the time of sample drop. The eluent gases are then swept by the helium carrier stream through a GC column to achieve separation of SO<sub>2</sub>, CO<sub>2</sub> and NO<sub>x</sub>’s before being leaked through an open split into the ion source of the mass analyzer. δ<sup>34</sup>S values are determined by comparing the respective sample peak areas, as [Amp-s], to a reference gas peak inlet from the DI reference bellows of the mass spectrometer during each sample run. Raw data were normalized to the Canyon Diablo Troilite (CDT) reference scale. The precision of δ<sup>34</sup>S<sub>BaSO<sub>4</sub></sub> (n=10), using the VG Prism II–CE EA1500 technique, is generally better than ±0.25‰.

Barite mineral separates were acidified with dilute hydrochloric acid prior to analysis of <sup>18</sup>O/<sup>16</sup>O ratio in order to avoid contamination by intergrown carbonates. The <sup>18</sup>O/<sup>16</sup>O ratio of BaSO<sub>4</sub> was determined using a high temperature, pyrolysis

reactor coupled to an isotope ratio mass spectrometer in continuous flow mode (Kornexl et al., 1999). The system is comprised of a Finnigan MAT TC/EA pyrolysis reactor interfaced to a Finnigan Mat Delta+XL mass spectrometer via a Conflow III open split/interface. Oxygen-containing compounds are quantitatively converted to CO gas at temperatures between 1350 and 1500°C. After GC separation, the CO gas is swept by a carrier gas into the mass spectrometer and  $\delta^{18}\text{O}$  values are determined. Results are expressed in the usual per mil notation relative to the international V-SMOW standard. Accuracy and precision of  $\delta^{18}\text{O}$  of  $\text{BaSO}_4$  is generally better than  $\pm 0.3\text{‰}$ .

### **3.3 Re and Os isotope analysis**

Rhenium-Osmium analysis of pyrite in Hess drill core was performed at the Radiogenic Isotope Facility at the University of Alberta. Analyses were carried out according to procedures used by Morelli et al. (2004) on pyrite mineral separates picked from samples that were hand-crushed using an agate mortar and pestle.

Sample fractions were weighed with a known amount of mixed  $^{185}\text{Re} + ^{190}\text{Os}$  spike and digested by the Carius tube method (Shirey and Walker, 1995). A maximum of 200 mg of sample was used for pyrite. The small sample size was used to avoid potential effects of the Claus process, which results in the oxidation of  $\text{H}_2\text{S}$  to S in preference to oxidation of Os to  $\text{OsO}_4$  during sample dissolution (Frei et al., 1998). Osmium was separated from the dissolved sample by solvent extraction and microdistillation (Birck et al., 1997; Cohen and Waters, 1996; Pearson and Woodland, 2000), and Re was separated by anion-exchange chromatography. Re and Os isotope compositions and abundances were determined by isotope dilution negative thermal ionization mass spectrometry (Creaser et al., 1991; Volkening et al., 1991) on a Thermo Triton mass spectrometer at the University of Alberta Radiogenic Isotope Facility. Blanks were monitored for the range of reagent volumes used in each analysis, and range from 0.06 – 0.57 %  $^{187}\text{Re}$ , 0.01 – 0.13%  $^{187}\text{Os}$  and 0.04 – 1.06%  $^{188}\text{Os}$  depending on the sample. Uncertainties in Re and Os mass spectrometer measurements, blank abundances, standard Re and Os isotopic values, and typical weighing uncertainties are all used in the error propagation to determine uncertainties for Re-Os isotopic abundances.

### **3.4 Bulk sediment lithochemistry**

Geochemical data were acquired for 68 major, trace and rare earth elements on whole-rock powders using a combination of analytical techniques used by Slack

et al. (2004). Analyses were carried out by Activation Laboratories in Ancaster, Ontario. Total organic carbon, S, CO<sub>2</sub> and SO<sub>4</sub> were measured by a LECO infrared analyzer (C and S), by difference after HCl dissolution, and by roasting to 250°C respectively. Major element oxide compositions were determined by inductively coupled plasma-atomic absorption spectrometry (ICP-AES). Trace elements including the rare earth elements were determined using inductively coupled plasma - mass spectrometry (ICP-MS) with the exception of the elements Sc, Be, V, Sr and Ba which were analyzed by ICP-AES. The ICP- AES and ICP-MS data were acquired on powders fused with lithium metaborate-tetraborate in order to insure total dissolution of resistate minerals (e.g., barite, zircon, rutile, monazite) prior to analysis. Duplicate samples and standards (e.g., Ohio Shale, SDO-1) were routinely run to monitor precision and accuracy.

## CHAPTER FOUR: PETROGRAPHY AND MINERALOGY

### 4.1 Barite petrography and mineralogy

Seventy samples from the barite occurrences in the NWT were examined in hand sample, by optical microscopy and using back-scattered electron (BSE) imaging on the Cameca SX100 microprobe at the University of Alberta. Six outcrop samples from the Walt/Tyrala/Hess occurrences were examined using the same methods. EPMA was necessary to identify and to understand the major element composition of barium silicates. Texturally, NWT samples can be divided into two broad categories, laminated barite and nodular barite. The Cooper occurrence is spatially associated with the barite occurrences in the NWT study area and is described separately. Samples 10NF12C and 10NF12E from the Cowan occurrence consist of barite and barium carbonate nodules and are described separately. Samples from outcrop in the Yukon are also presented separately.

#### *4.1.1 Pyritic debritic mudstone at Cooper showing*

The debritic mudstone at the Cooper showing has heterogenous clasts that could be sourced from a variety of lithologies. The samples can be classified as poorly-sorted, polymictic matrix-supported debrites (Plate 4.1a). The mudstone matrix is 50 to 70 % by volume of samples and is composed of very fine-grained brownish clay minerals and some 2 – 5  $\mu\text{m}$  sized, elongate micas. There is no discernable foliation in any samples.

There are at least 5 observed clast-types with varying morphologies and sizes. These are: (1) 200 – 1000  $\mu\text{m}$  elongate, subrounded, muddy-brown mudstone clasts (~ 35 % of clasts, Plate 4.1b), (2) 500 – 2500  $\mu\text{m}$ , high-relief, transparent, embayed, subangular to subrounded clasts composed of 10  $\mu\text{m}$  anhedral sericitized feldspars which are sometimes replaced by coarse, euhedral pyrite (~35 % of clasts, Plate 4.1c), (3) 40  $\mu\text{m}$ , high relief, subrounded and weakly embayed quartz crystals (20 % of clasts, Plate 4.1b), (4) 500  $\mu\text{m}$ , dark grey, high relief, elongate laminated siltstone/shale clasts (5 % of clasts, Plate 4.1d), and (5) 5 % dark black organic matter. There are trace amounts of orange-brown, translucent phosphate aggregates.

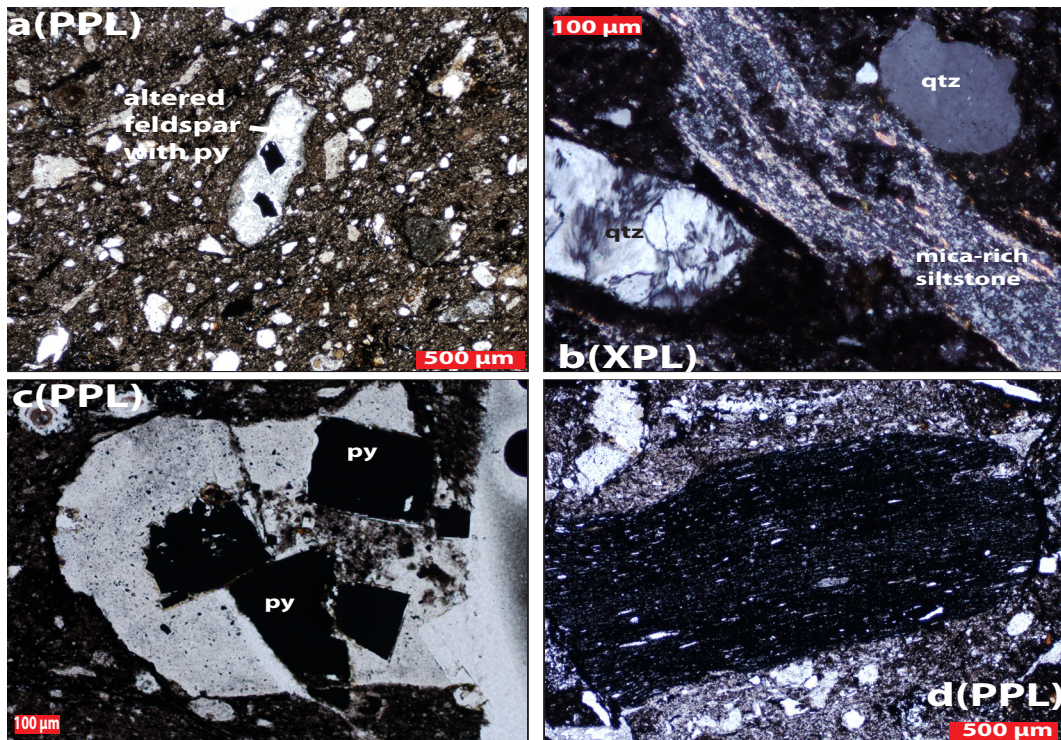


**Plate 4.1:** Cooper debritic mudstone (a) general view (sample 10NF8A-1), (b) mudstone clasts (sample 10NF8A-1), (c) altered feldspars replaced by pyrite (sample 10NF8A-1), (d) laminated shale/siltstone clasts (sample 10NF10A).

#### 4.1.2 NWT Laminated barite

Laminated barite and fine-grained sediments are distinct from each other. Lower Earn group sediments are composed of low-relief, dark brown, very-fine grained brown, clays ( $< 2 \mu\text{m}$ ) and  $5\text{--}10 \mu\text{m}$  high-relief, elongate crystals of detrital quartz (Plate 4.2a) These layers are often crudely laminated ( $500 - 2000 \mu\text{m}$  thick) and show pressure solution features (Plate 4.2b). There are often very fine laminations/veinlets that are composed of opaque organic matter and microcrystalline aggregates of translucent, orange-brown phosphatic material (Plate 4.2c). Very-fine grained crystals of pyrite can be found within the organic matter, these often appear as discrete ( $5 - 10 \mu\text{m}$ ) crystals which rarely form framboids. Phosphate and organic-rich veinlets can also cross-cut baritic layers.

Barite laminations are dominantly composed of  $50 - 200 \mu\text{m}$ , low relief crystals of barite which range from anhedral to subhedral in morphology. Laminated barite has trace amounts of CaO (mean of  $0.06\%$ ) and Sr (mean of  $0.14\%$ ) (Table B1). The major element composition of barite from both the NWT and Yukon is summarized in Table 4.1 with detailed results in Appendix B. Barite from the NWT

and Yukon, whether laminated or nodular, is similar in its major element composition with the exception of Sr, which is slightly more enriched in Yukon barite.

Barite major element composition											
NWT Laminated barite						Cooper Barite					
wt. %	BaO	CaO	SrO	SO <sub>3</sub>	Total	wt. %	BaO	CaO	SrO	SO <sub>3</sub>	Total
N	238	200	237	238	238	N	54	49	54	54	54
Mean	66.47	0.04	0.13	34.53	101.23	Mean	66.49	0.21	0.19	33.50	100.37
Max	67.65	1.17	1.57	37.70	103.31	Max	68.40	5.57	1.20	34.99	102.61
Min	61.72	0.01	0.01	30.75	98.13	Min	64.98	0.01	0.02	30.46	98.06
Stdev	0.72	0.10	0.19	0.61	0.82	Stdev	0.65	0.79	0.27	1.39	1.24
NWT Nodular barite						Yukon barite					
wt. %	BaO	CaO	SrO	SO <sub>3</sub>	Total	wt. %	BaO	CaO	SrO	SO <sub>3</sub>	Total
N	61	49	61	61	61	N	184	184	184	184	184
Mean	66.67	0.03	0.21	34.39	101.39	Mean	66.26	0.05	0.28	34.44	101.00
Max	68.49	0.16	1.14	35.78	103.01	Max	67.51	1.07	9.95	36.60	102.61
Min	64.98	0.01	0.02	32.13	100.03	Min	58.27	0.01	0.02	29.94	97.80
Stdev	0.61	0.04	0.23	0.56	0.69	Stdev	0.91	0.11	0.79	0.63	0.81

**Table 4.1: Average major element composition of NWT laminated barite, NWT nodular barite, Cooper NWT barite and Yukon barite.**

A major accessory mineral in these laminations is hyalophane (Ba, K – bearing feldspar) which forms 100 – 500 µm, moderate relief, euhedral, unzoned, elongate hexagonal crystals. These are ubiquitously replaced to some extent by barite (4.2d). Hyalophane has no particular orientation within laminations but is preferentially concentrated at the boundary between the host-sediments and barite laminations (Plate 4.2e). Hyalophane in barite laminations has a range of concentrations of BaO from 22 to 38 %, K<sub>2</sub>O from 3.4 to 6 %, and trace amounts of TiO<sub>2</sub> and Na<sub>2</sub>O (Table B5). Euhedral, < 50 µm, crystals of pyrite can also be found in barite laminations. Pyrite is often oxidized to some extent and has rims of iron oxyhydroxides (Plate 4.2f).

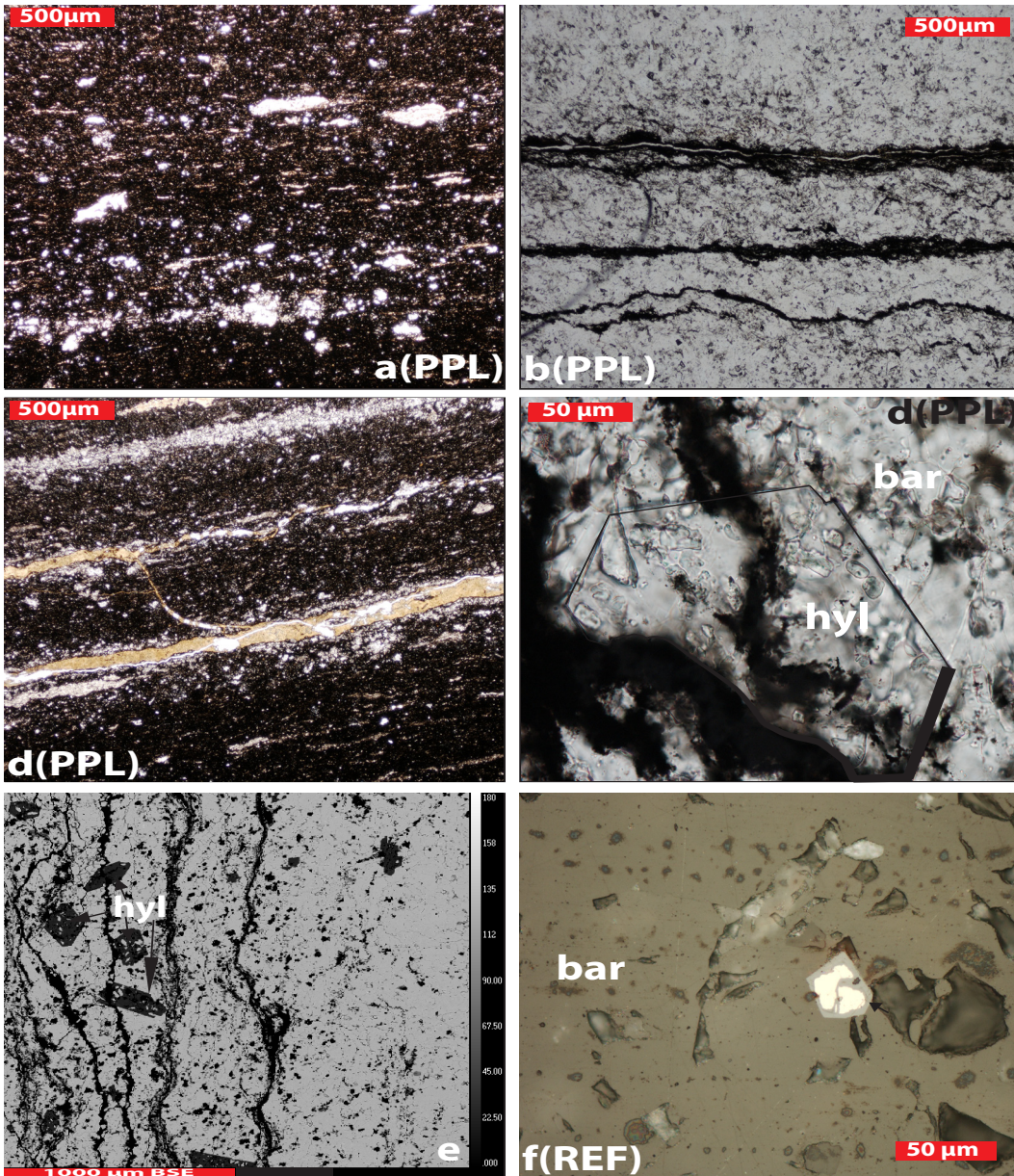


*Plate 4.2: (a) Very-fine grained clays and detrital quartz-grains in lower Earn Group sediments (sample 10NF17A), (b) thick fine-grained barite laminations (sample Ax-size 1), (c) orange, phosphate rich laminations in lower Earn group sediments (sample 10NF17A), (d) euhedral, high-relief hyalophane crystal in barite laminations (sample Ax-09-02), (e) BSE image of laminated white barite and grey hyalophane crystals with black host sediments (sample Ax-size 1), (f) fine-grained yellow, euhedral pyrite cube coated with grey iron oxyhydroxides in a barite lamination (sample Ax-09-02).*

#### 4.1.3 NWT Nodular barite:

The sediments that host nodular barite are the same as those that host barite laminations and consist of very-fine grained clays and detrital quartz. These sediments often contain much more organic material than those containing laminated barite and sometimes even contain fossil material such as sponge spicules in the sedimentary matrix (Plate 4.3a). The laminations in the sediments wrap around barite nodules.

Barite nodules have a wide range of morphologies and bulk compositions. Shapes and sizes of nodules range from 500 – 3500  $\mu\text{m}$  and from elongate to perfectly spherical, respectively (Plates 4.3b and 3c). Nodular barite has trace amounts of CaO (mean of 0.03%) and SrO (mean of 0.21%) (Table B2). Barite crystals can be less than 100  $\mu\text{m}$  and anhedral, to elongate fibres that are up to 800  $\mu\text{m}$  long. Clay minerals from host sediments can be found in some nodules which is consistent with formation of the nodules post-deposition of sediments (Plate 4.3d).

Hyalophane is much more common in the barite nodules than the laminations, forms larger crystals (up to 500  $\mu\text{m}$ ), and is also replaced in patches by barite. Hyalophane in nodular barite has a range of concentrations of BaO from 15 to 29%,  $\text{K}_2\text{O}$  from 3 to 8 % and slightly elevated  $\text{TiO}_2$  concentrations (Table B5) compared to hyalophane from laminated barite. Another barium mineral found in nodular samples is cymrite ( $\text{BaAl}_2\text{Si}_2(\text{O}, \text{OH})_8 \cdot \text{H}_2\text{O}$ ). Cymrite forms large (500 – 2000  $\mu\text{m}$ ), high relief, euhedral, rectangular crystals that are often brown under transmitted light and have 2 very-well developed cleavages at right angles. These crystals can also be observed growing into the host sediments (Plate 4.3e). Cymrite has major element oxide concentrations that range from 36 to 39 % BaO, 0.04 to 3.5 %  $\text{K}_2\text{O}$ , 30 to 35 %  $\text{SiO}_2$ , 18 to 26 %  $\text{Al}_2\text{O}_3$ , and trace concentrations of NaO, MgO, CaO,  $\text{TiO}_2$  and FeO (Table B6). It is a hydrous-silicate which contains Al, Si, Ba and 4-5 weight %  $\text{H}_2\text{O}$  in its structure (Deer et al., 2001), and, therefore, the measured elemental totals (mean of 95.73) are acceptable.

Cymrite and hyalophane can be intergrown but cymrite more commonly replaces hyalophane. Pyrite is also present in nodules to a greater extent than in laminated barite (Plate 4.3f). One sample (B2-515A) also contained medium-grained, euhedral albite crystals which are much rarer than hyalophane. Albite from this sample is remarkably pure and has trace amounts of  $\text{K}_2\text{O}$ , BaO, FeO and MgO (Table B7).

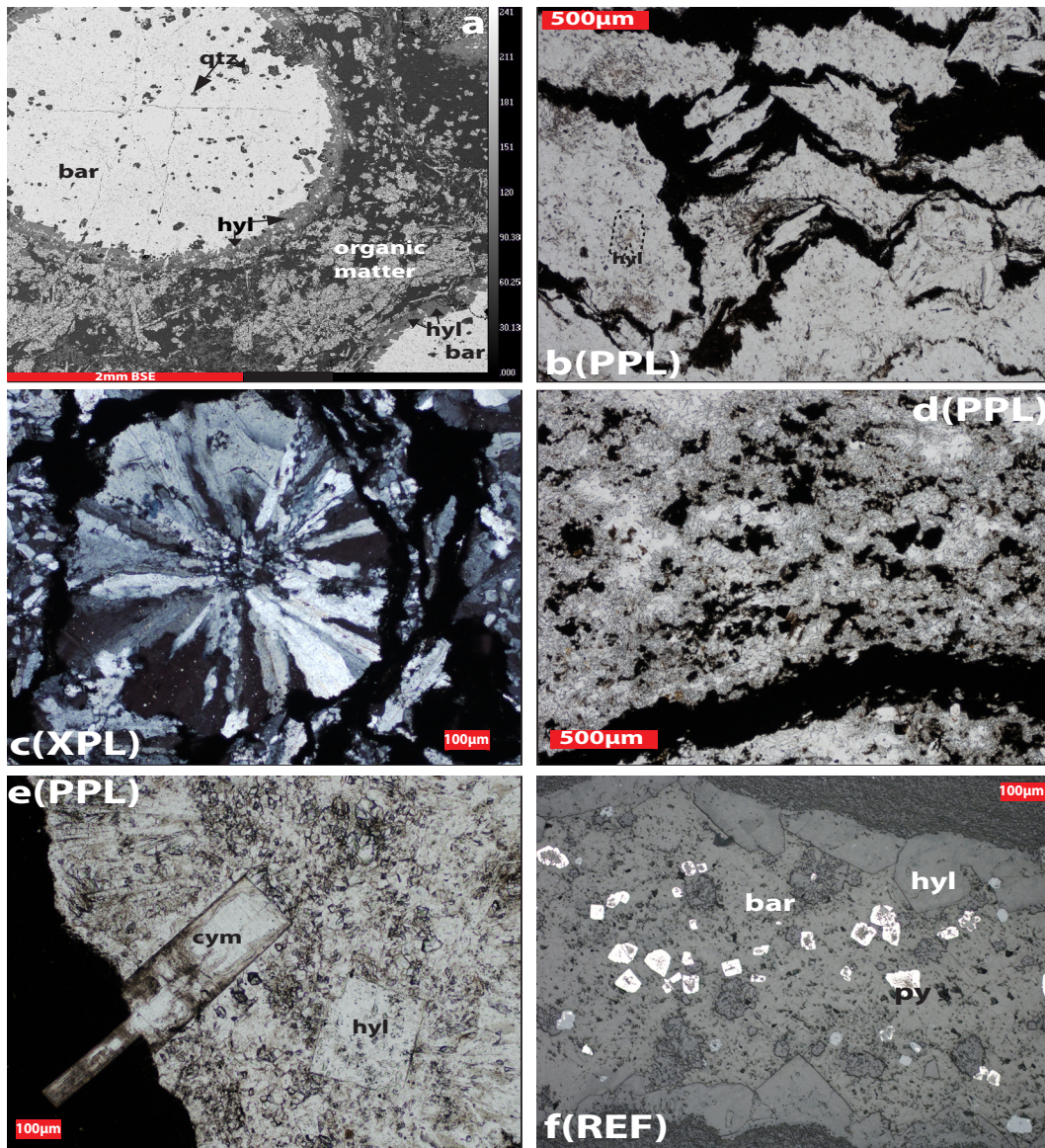


*Plate 4.3: (a) BSE image of spherical barite (white) nodule rimmed by grey hyalophane crystals and containing small black quartz crystals in organic-rich sediments (sample B1-nod6), (b) irregular barite nodules in dark black organic-rich sediments (sample 10NF12B), (c) radiaxial, fibrous barite crystals in a nodule with a core of fine-grained barite (sample 10NF12A), (d) fine-grained white barite nodule with inclusions of amorphous black clays (sample B2-516D-2), (e) coarse, rectangular, brownish cymrite crystal growing into sediments and low relief hyalophane in white barite nodule (sample B2-3), (f) yellow, euhedral pyrite crystals overgrowing a barite and hyalophane-rich nodule (sample 10NF12D).*

The major element composition of all diagenetic hyalophane, cymrite and albite from NWT barite occurrences is summarized in Table 4.2. Microprobe data for barium silicate composition can be found in Appendix B.

<b>Mineral</b>	<b>Major element composition</b>										
	<b>Na<sub>2</sub>O</b>	<b>MgO</b>	<b>Al<sub>2</sub>O<sub>3</sub></b>	<b>SiO<sub>2</sub></b>	<b>K<sub>2</sub>O</b>	<b>CaO</b>	<b>TiO<sub>2</sub></b>	<b>MnO</b>	<b>FeO</b>	<b>BaO</b>	<b>Total</b>
<b>Lam Hyl</b>											
N	168	13	168	168	168	0	168	0	3	168	168
Mean	0.25	0.29	22.50	46.42	4.57	-	0.12	-	0.12	22.56	96.87
Max	0.48	1.21	23.98	51.15	5.96	-	0.19	-	0.18	38.02	99.54
Min	0.17	0.04	17.75	35.02	3.38	-	0.07	-	0.08	18.47	95.03
Stdev	0.04	0.37	0.59	1.85	0.48	-	0.02	-	0.05	2.16	0.81
<b>Nod Hyl</b>											
N	325	2	325	325	325	10	325	0	22	325	325
Mean	0.23	0.06	22.46	48.20	5.29	0.11	0.16	-	0.21	21.38	97.79
Max	0.59	0.08	24.06	53.96	7.97	0.32	2.23	-	0.75	28.94	100.51
Min	0.14	0.03	19.48	42.01	3.03	0.04	0.07	-	0.08	15.19	95.19
Stdev	0.06	0.03	0.57	2.11	0.80	0.11	0.12	-	0.19	2.19	0.81
<b>Cymrite</b>											
N	38	2	38	38	38	6	38	0	7	38	38
Mean	0.09	0.05	25.11	32.57	0.53	0.05	0.31	-	0.16	37.50	95.73
Max	0.25	0.06	25.81	35.02	3.53	0.07	0.35	-	0.46	39.41	96.42
Min	0.04	0.04	17.75	30.39	0.04	0.04	0.19	-	0.09	35.98	95.08
Stdev	0.03	0.01	1.25	0.88	0.52	0.01	0.03	-	0.13	0.74	0.36
<b>Albite</b>											
N	10	2	10	10	1	1	1	0	3	3	10
Mean	11.03	0.26	20.30	68.44	1.40	0.11	0.02	-	0.77	0.35	100.37
Max	11.86	0.37	25.14	69.74	1.40	0.11	0.02	-	1.01	0.84	101.36
Min	7.07	0.16	19.13	61.90	1.40	0.11	0.02	-	0.61	0.07	97.63
Stdev	1.43	0.15	1.72	2.36	-	-	-	-	0.21	0.42	1.10

**Table 4.2: Average major element composition of hyalophane in laminated and nodular barite, cymrite and albite from NWT barite occurrences.**

The microprobe data from this study was normalized to feldspar composition (on the basis of 8 oxygens) and converted to the end-member ternary K-feldspar-albite-celsian system based on the sedimentary association of Essene et al. (2005). Hyalophane has a trend of end-member compositions that range from 24 – 61 % K-Feldspar, 1 – 7 % albite and 36 – 71 % celsian. These data are plotted in Figure 4.1 against compiled data for barium feldspars with diagenetic associations (Essene et al., 2005 and references therein). As can be seen from this figure the feldspars from this study expand the range of barium feldspar composition and

stability in diagenetic settings.

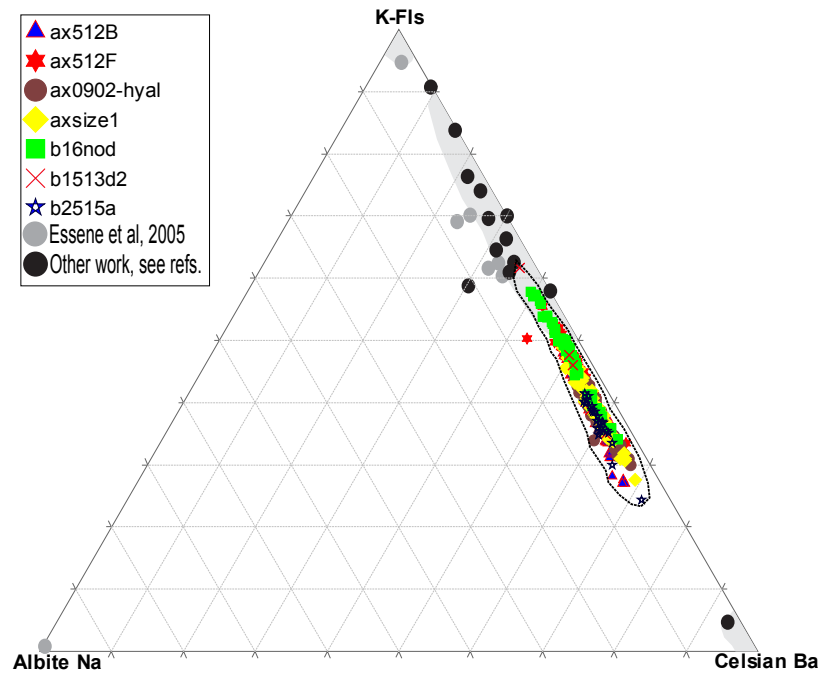


**Figure 4.1: Ternary plot of hyalophane composition. Apices of diagram are end-member compositions of Na (Albite), K (K-feldspar) and Ba (Celsian) feldspars. Data for this plot from this study can be found in Appendix C. Grey and black circles represent data from Bjorlykke and Griffin, 1973; Essene et al., 2005; Jakobsen, 1990; Long et al., 1994; Moro et al., 2001**

#### 4.1.4 Cowan epigenetic barite and nodular barium carbonate

Samples 10NF12C and 10NF12E collected from the Cowan consist of a mineral assemblage unlike those found in the other NWT barite occurrences.

The host sediments in the sample consist of crudely laminated, dark brown clays. Well-defined, elongate (50 to 200  $\mu\text{m}$  X 1000  $\mu\text{m}$ ) crystals of barytocalcite have been identified which appear to resemble spicules that cross-cut laminations, but terminate against nodules (Plate 4.4a). Microcrystalline (< 50  $\mu\text{m}$ ), fibrous barite crystals clusters on the edges of nodules (Plate 4.4b) and also replace the barium carbonates. Barite from these samples has similar major element composition to laminated and nodular barite from the NWT (Table B3)

Nodules in this sample are elongate and deformed (700 - 1400  $\mu\text{m}$  by 300 - 1000  $\mu\text{m}$ ) and consist mostly of subhedral, interlocking, high relief, 200 to 400  $\mu\text{m}$  crystals of witherite (barium carbonate) which is replaced by varying amounts of

very fine grained, barite (20 – 50  $\mu\text{m}$ ) (Plate 4.4c) and norsethite ( $\text{Ba,Mg}(\text{CO}_3)_2$ ). Norsethite is common on the edges/rims of nodules and can also be replaced by barite (Plate 4.4d). Euhedral hyalophane crystals are also present in the nodules but are replaced by patches of barytocalcite, witherite and barite (Plate 4.8e). Euhedral crystals of pyrite which have the same altered/weathered appearance as others found in laminations and nodules are also found (Plate 4.4f).

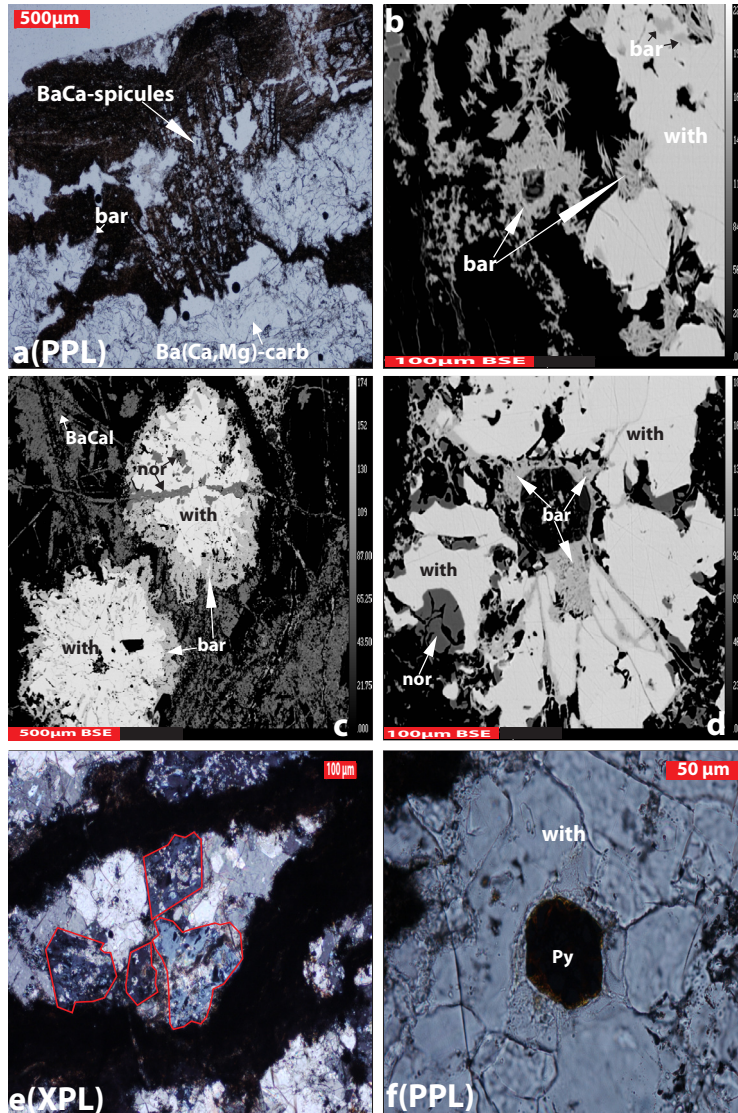


**Plate 4.4:** (a) barytocalcite spicules and witherite nodules in a dark-brown silty mudstone, (b) BSE image of grey microcrystalline barite fibres replacing a white witherite nodule, (c) BSE image of light grey barite and dark grey norsethite replacing white witherite nodules, (d) BSE image of light grey barite and dark grey norsethite replacing white witherite nodules, (e) grey, euhedral hyalophane crystals (outlined in red) in a witherite nodule being replaced by carbonates and

***barite, (f) oxidized pyrite grain in a witherite-rich nodule. [All photos are from sample 10NF12C].***

#### *4.1.5 Yukon 'laminated' barite outcrop*

'Laminated' barite in the Portrait Lake Formation is made up of very thin layers of very fine grained ( $< 5 \mu\text{m}$ ), light brown aggregates of clay minerals with varying amounts of microcrystalline, orange-brown, translucent phosphatic material and opaque black organic material (Plate 4.5a). Under reflected light the organic material contains 1- 5 % anhedral iron oxyhydroxides and oxidized pyrite ( $< 10 \mu\text{m}$ ), there are no observed pyrite framboids.

A significant proportion by volume of the laminations comprises witherite which is found as moderate relief, transparent, elongate,  $\sim 400 \mu\text{m}$  crystals (Plate 4.5b). Low-relief, subhedral, rectangular crystals of hyalophane which contain many inclusions are also commonly observed within barite- or witherite-rich 'laminations' (Plate 4.5c). Another accessory mineral is medium-grained, subhedral quartz crystal (Plate 4.5d)

Laminations are thick (0.2 – 0.4 cm) and consist of low-moderate relief, transparent barite crystals. Barite from Yukon study area has higher Sr concentrations (mean of 0.28 %) and lower Ca concentrations (mean of 0.05%) (Table B4) compared to barite from the NWT. These crystals are medium grained, subhedral and elongate and roughly aligned long-end along thick laminations. Barite layers in these samples do not have well-defined boundaries with host sediments, and are often fractured indicating post-depositional brittle deformation and brecciation (Plate 4.5e).

In sample 10NF42F-2, microcrystalline, carbonate-rich minerals replace both original host-sediments and barite (Plate 4.5f). Where the barite layers are thick, the replacement is dominant on the edges. Trace amounts of sulphides in the form of pyrite and galena accompany the fine-grained carbonate (Plates 4.5g and 5h); these are identical to sulphides in Hess barite drill core (see Section 4.2).

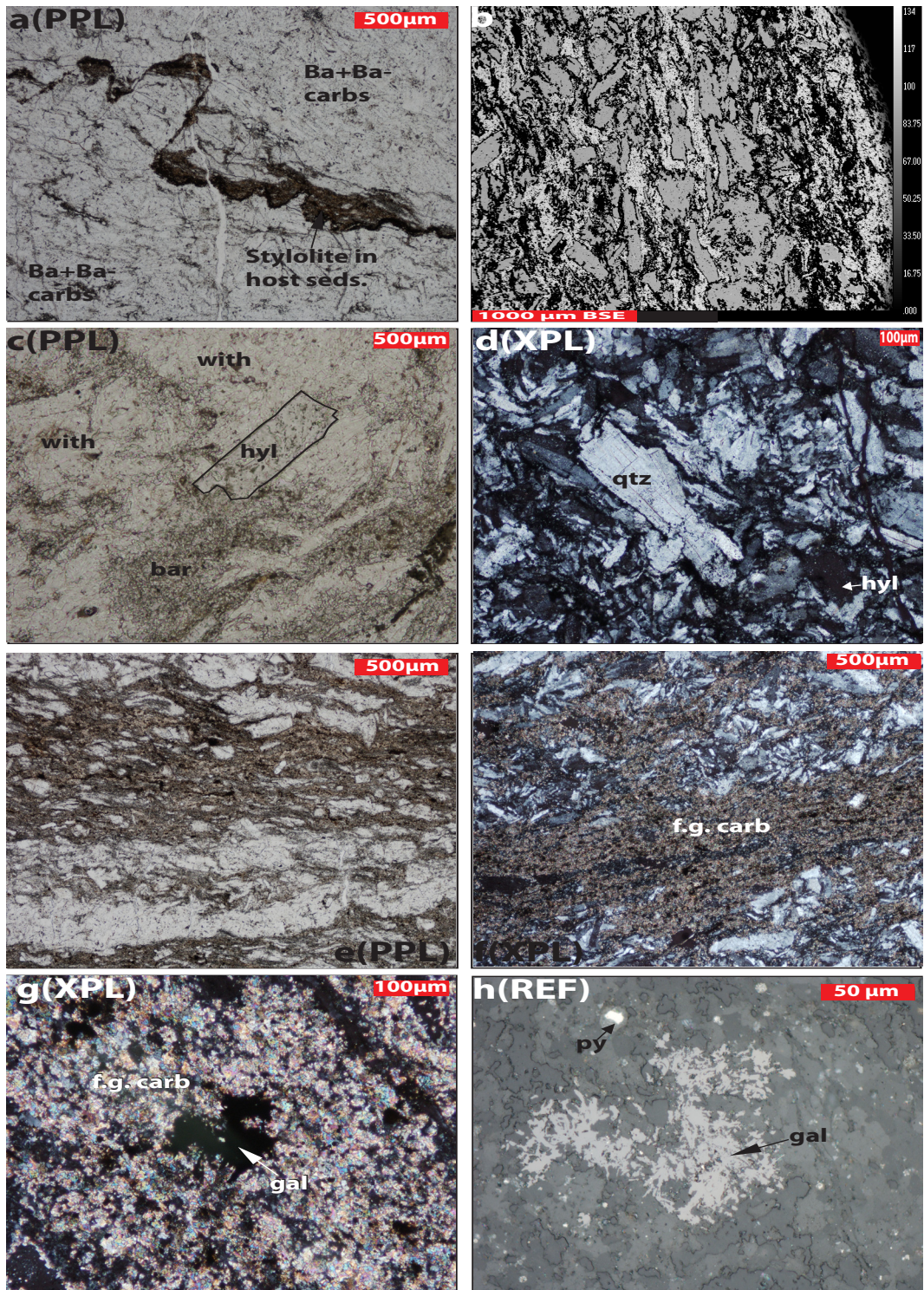


*Plate 4.5: (a) stylolite of organic-rich sedimentary material sandwiched between white barite and witherite-rich laminations (sample 10NF42F1), (b) BSE image of grey barite and white witherite crystals in laminations (sample 10NF42C), (c) hyalophane crystal in witherite-rich laminations (sample 10NF42F2), (d) coarse*

*quartz crystals in barite + witherite lamination (sample 10NF42F1), (e) brecciated margins of barite + witherite laminations (sample 10NF42F1), (f) fine-grained, brown carbonate replacing sediments and barite along laminations (sample 10NF42F2), (g) fine-grained, high-relief Ba(Ca)-carbonate associated with opaque galena (sample 10NF42F), (h) Close-up, reflected light image of (g) showing grey galena hosted by fine-grained carbonates (sample 10NF42F).*

#### **4.2 Hess ‘mineralized’ barite petrography and mineralogy**

Twenty thin-sections were prepared from drill core from the Hess barite hole, were examined by optical microscopy and using back-scattered electron (BSE) imaging on the Cameca SX100 microprobe at the University of Alberta. EPMA was utilized to understand the major element composition of base-metal sulphides and to allow distinction between different stages of mineralization. Although there are only limited samples from a single hole, multiple assemblages of base metal sulphides and gangue carbonates ± quartz can be observed. These hydrothermal mineral assemblages are described below.

##### *4.2.1 Hess barite drill core:*

Least altered sediments:

Weakly altered and/or brecciated Portrait Lake Formation sediments are found in the first 35 m of the Hess barite hole. These sediments are crudely laminated and consist of dark black-grey, organic rich clays which contain varying amounts of very fine grained detrital quartz (Plate 4.6a). Where least altered, there are only trace amounts of very-fine grained iron oxyhydroxides and almost no pyrite.

A series of fine-grained quartz ± pyrite veinlets, 100 – 300 µm thick; cross-cut and brecciate Portrait Lake Formation sediments into subangular to subrounded, 200 – 600 µm clasts (Plate 4.6b and 4.6c). These are post-dated by thicker quartz veinlets (500 – 1000 µm) which are monominerallic (Plate 4.6d).

At 40.9 m depth, there is a dramatic change in overall mineralogy which marks the beginning of a ~ 50m thick alteration zone. Hand samples are distinctly grey in colour and react with 10 % hydrochloric acid. This corresponds to an overall increase in carbonate content of the sediments, which accompanies the disappearance of quartz veinlets.

Nodules in the Hess core are morphologically similar, but have a different composition to those found in the NWT barite samples (with the exception of Cowan). Nodules in the Hess core consist of carbonate minerals, barite and some

quartz (Plates 4.6e and 4.6f). Barite where observed, is microcrystalline to very-fine grained and can only be distinguished by its low relief and first-order grey to white interference colours.

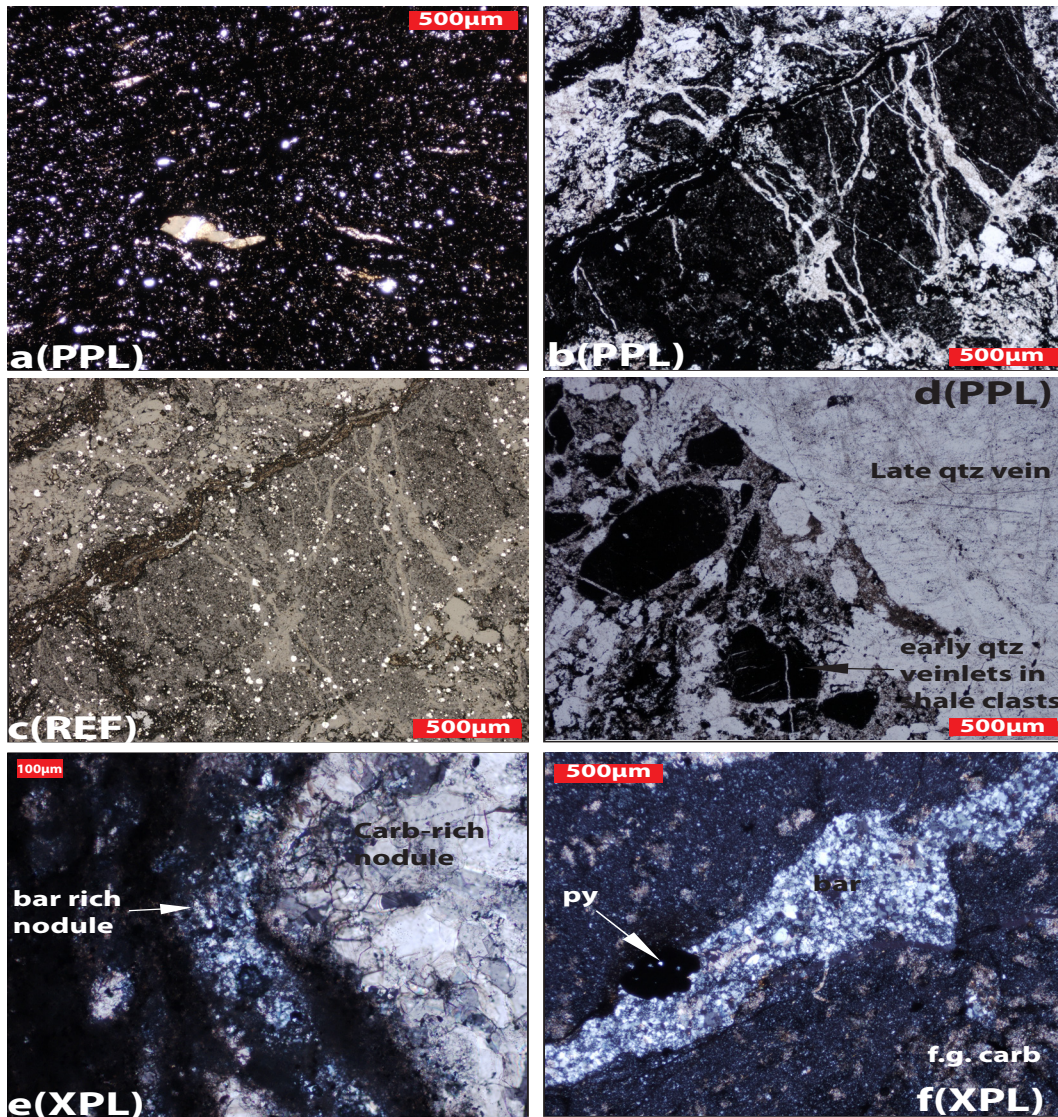


*Plate 4.6: (a) very-fine grained clays and detrital quartz-grains in Portrait Lake Fm. sediments (sample H36.6), (b) multiple quartz veinlets cross-cutting and brecciating Portrait Lake Fm. (H27.05), (c) reflected image of (b) showing fine-grained pyrite associated with quartz veinlets and with Portrait Lake Fm. sediments (H27.05), (d) shale clasts cross-cut by late, barren, coarse quartz veinlet (H27.05), (e) barium-rich and carbonate-rich nodules in Earn Group sediments (H40.9), (f) barite nodule overprinted by opaque pyrite crystal (H42.8).*

The carbonates in these samples include fine-grained ankerite, witherite,

barytocalcite, and norsethite, coarse-grained calcite, dolomite and rare siderite. All of these minerals have characteristic carbonate interference colours and can only be distinguished from each other on the basis of cleavage, twinning, interference figures or BSE imaging (Plates 4.7a – f). The barite and barium carbonates are coeval with sulphide mineralization.

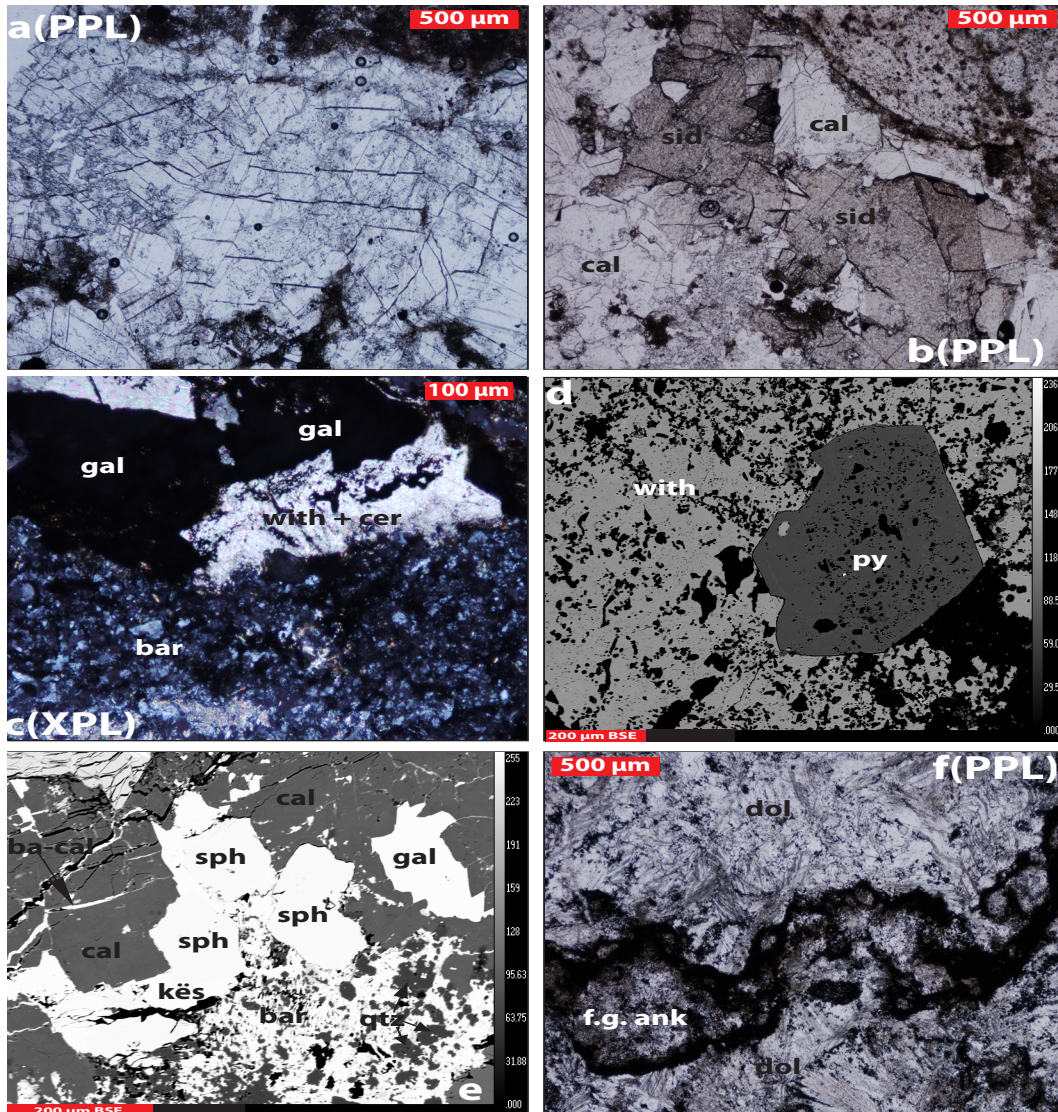


*Plate 4.7: (a) coarse-grained calcite nodule (H40.9), (b) brown siderite and calcite in a nodule in carbonate-altered sediments (H41.9), (c) high-relief, white, very-fine grained witherite and cerussite associated with galena (opaque) and fine-grained, grey, barite (H44.4A), (d) BSE image of white fine-grained witherite rimming grey pyrite crystal (H45.0), (e) BSE image of coarse grained, grey calcite crystals overgrown by bright white sulphides and barite (H44.4A), (f) coarse grained, white dolomite crystal layers sandwich a fine-grained, brown ankerite*

*layer (H72.1)*

Early Pyrite:

Pyrite is the only sulphide mineral that is present consistently throughout the paragenesis in Hess drill core. Early pyrite is found overprinting nodules (Plate 4.8a) and often displays complex fracturing patterns (Plate 4.8b) suggesting that it post-dates lithification of the sedimentary rocks but pre-dates a brittle deformation event. In the least altered parts of the Hess core the relationship between the pyrite and the carbonates is unclear. Here, pyrite replaces host clays as opposed to carbonate and/or barite rich nodules (Plate 4.8c). However, as the amount of alteration increases; it is common to see pyrite replaced by carbonates, barium minerals and other sulphides (Plates 4.8d and 4.8e). In some cases, barite, base metal sulphides and carbonates can rim pyrite crystals or line fractures within them (Plate 4.8f). These relationships clearly suggest that the pyrite is epigenetic and is the oldest sulphide at Hess. Pyrite shows no major changes in major element composition (Table 4.3)

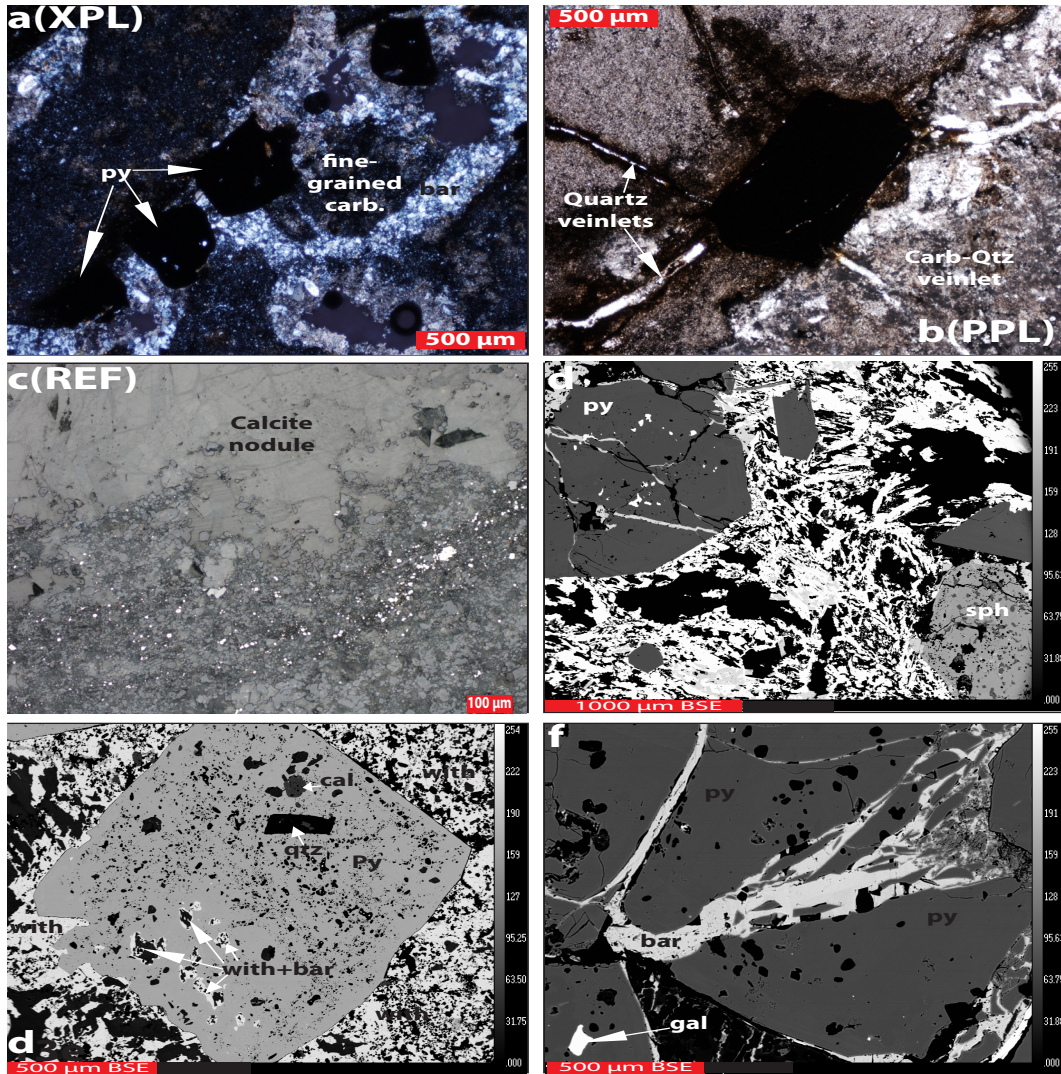


*Plate 4.8: (a) opaque, epigenetic pyrite grains overprint both barite-carbonate nodule and host Earn group sediments (H42.8A), (b) fractured, yellow pyrite grain cross-cut by multiple quartz-carbonate veinlets (H44.4B), (c) epigenetic, yellow, fine-grained pyrite lining outside of a calcite-rich nodule (H40.9), (d) BSE image of a dark grey pyrite crystal and light grey Stage 1 spalerite overgrown and cross-cut by bright white galena and creamy white witherite (H64.5B), (e) BSE image of a large grey pyrite crystal rimmed by witherite and replaced by white witherite and barite as well as dark grey calcite and quartz (H45.0), (f) BSE image of light grey barite veinlet fracturing dark grey pyrite crystals (H64.5).*

<b>MINERAL</b>	<b>Elemental Composition</b>									
	<b>S</b>	<b>Fe</b>	<b>Cu</b>	<b>Zn</b>	<b>As</b>	<b>Ag</b>	<b>Sn</b>	<b>Sb</b>	<b>Pb</b>	<b>Total</b>
<b>Pyrite</b>										
N	32	32	0	3	29	0	0	0	0	32
Mean	52.87	46.53	-	0.88	0.88	-	-	-	-	99.85
Max	53.85	47.19	-	1.67	2.36	-	-	-	-	100.87
Min	51.64	44.28	-	0.06	0.10	-	-	-	-	98.33
Stdev	0.60	0.49	-	0.81	0.64	-	-	-	-	0.59
<b>Sphalerite</b>										
N	136	136	57	136	12	4	14	1	2	136
Mean	33.01	0.77	0.34	64.87	0.08	0.09	1.05	0.10	1.08	98.76
Max	35.84	12.73	3.61	66.48	0.21	0.15	3.10	0.10	1.68	104.04
Min	31.18	0.07	0.04	55.55	0.07	0.06	0.10	0.10	0.49	96.12
Stdev	0.40	1.40	0.66	1.55	0.04	0.04	0.99	-	0.84	0.82
<b>Galena</b>										
N	30	18	12	5	3	5	1	28	30	30
Mean	13.30	0.08	0.15	0.95	0.10	0.63	0.53	2.43	82.49	98.38
Max	13.69	0.24	0.54	2.12	0.18	1.01	0.53	4.67	86.51	101.44
Min	12.67	0.04	0.05	0.08	0.06	0.10	0.53	0.13	78.23	96.08
Stdev	0.25	0.06	0.13	0.87	0.07	0.34	-	1.66	2.62	1.43
<b>Kesterite</b>										
N	88	88	88	88	4	87	88	0	1	88
Mean	28.65	0.56	26.07	14.72	0.07	1.29	27.34	-	0.08	98.50
Max	29.45	11.72	27.46	19.91	0.07	3.42	28.69	-	0.08	100.39
Min	27.98	0.05	24.16	3.80	0.06	0.40	24.56	-	0.08	96.37
Stdev	0.29	1.53	0.74	1.95	0.00	0.47	0.64	-	-	0.69
<b>Geocronite</b>										
N	65	23	6	13	65	3	6	65	65	65
Mean	17.34	0.18	0.18	0.49	4.02	0.51	5.88	11.13	65.63	98.64
Max	19.53	0.98	0.32	4.13	5.04	0.54	11.65	23.44	69.16	103.19
Min	16.47	0.04	0.05	0.06	0.33	0.49	0.13	9.21	54.68	96.31
Stdev	0.57	0.31	0.13	1.11	1.03	0.02	6.27	3.16	3.80	0.96
<b>Franckeite</b>										
N	12	12	11	2	12	12	12	12	12	12
Mean	19.51	0.97	0.28	0.16	0.33	0.53	11.66	9.45	54.47	96.96
Max	19.78	1.09	0.33	0.22	0.37	0.79	11.92	10.19	55.21	97.52
Min	19.30	0.90	0.20	0.10	0.28	0.42	11.51	9.26	53.56	96.44
Stdev	0.13	0.06	0.04	0.08	0.03	0.09	0.13	0.25	0.48	0.35

*Table 4.3: Average elemental composition of sulphides and sulphosalts from Hess barite drill core.*

Base-metal sulphides and gangue minerals:

Galena is found as 100 to 200  $\mu\text{m}$ , anhedral patches (Plate 4.9a) and can be observed replacing pyrite (Plate 4.9b). It is intimately associated with barite and witherite ( $\pm$  cerrusite) (Plate 4.9c and 9d). It is often replaced by dark, grey anhedral geocronite ( $\text{Pb,Sb,As}$ -sulphosalt,  $\text{Pb}_{14}(\text{Sb,As})_6\text{S}_{23}$ ) (Plate 4.9e). Franckeite ( $\text{Pb,Sn,Sb}$ -sulphosalt) and geocronite (Plate 4.9f) post-date galena mineralization. Galena is slightly enriched in antimony (mean of 2.27 wt. %) when it is replaced by geocronite (Table 4.3).  $\text{Pb,Sb,As}$  sulphosalts have more variable Pb, Sb and As content (Table 4.3).

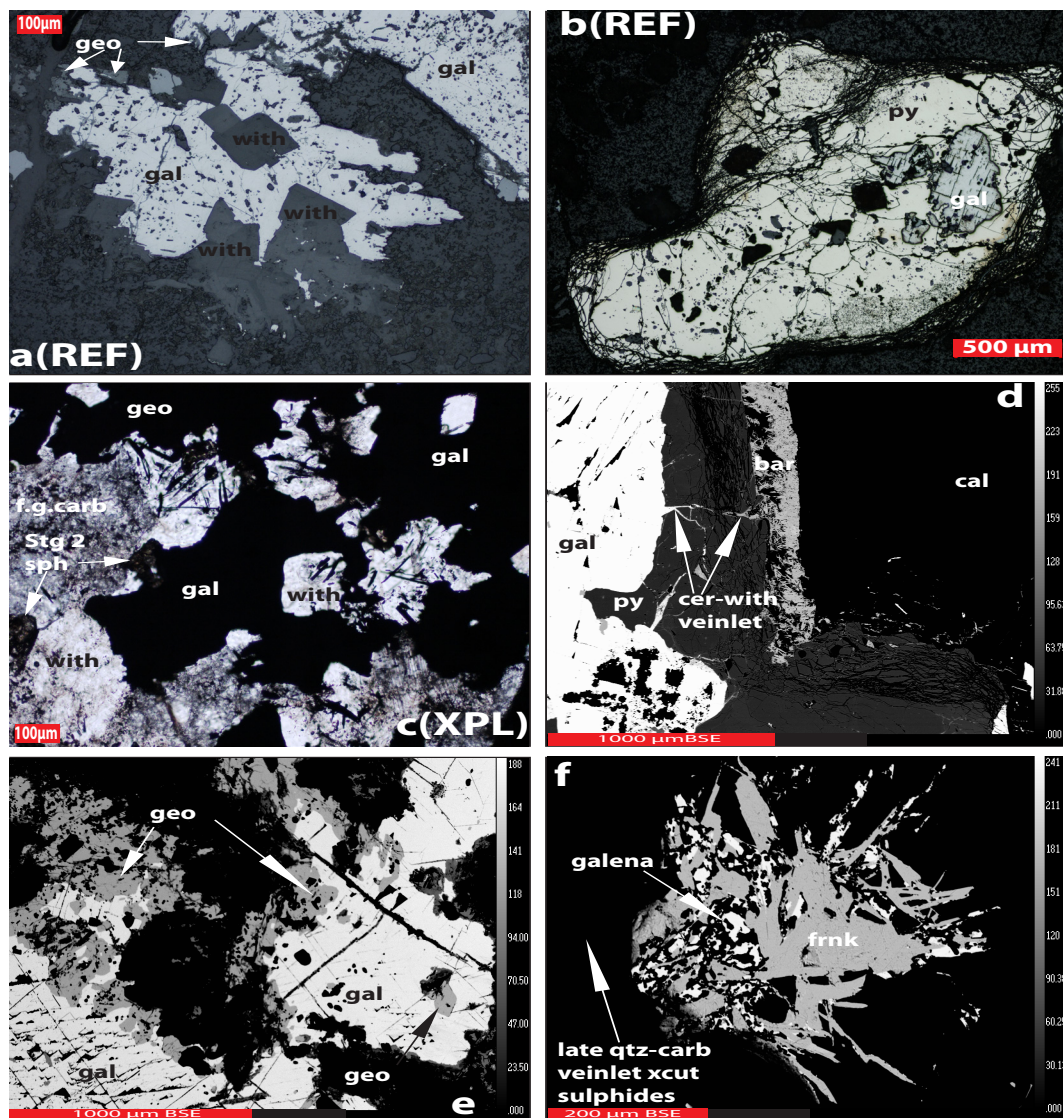


*Plate 4.9: (a) grey galena associated with coarse, high-relief witherite and edges replaced by dull grey PbSbAs-sulphosalts (H44.4A), (b) Yellow, coarse, fracture pyrite crystal replaced by grey galena (H46.2), (c) opaque galena intergrown with high-relief, white witherite (H45.0), (d) BSE image of white galena overgrowth-*

*ing a fractured, dark grey pyrite crystal that is rimmed with creamy grey micro-crystalline barite with a veinlet of witherite and cerrusite connecting the galena and barite (H44.4a), (e) BSE image of grey PbSbAs-sulphosalts replacing white galena (H44.4A), (f) BSE image of grey franckeite overprinting galena, these minerals are crosscut by a late quartz-carbonate veinlet on the left (H66.1).*

Textural relationships observed in the zinc-bearing minerals indicate two stages of mineralization. Early sphalerite mineralization (Stage 1 sphalerite) is coarse-grained and has distinct Fe-zoning that corresponds to orange layers with abundant pyrite inclusions (Plate 4.10a) which are cross-cut by galena and barite (Plate 4.10b). Late sphalerite (Stage 2 sphalerite) appears as fine to coarse grained, yellow, anhedral to euhedral crystals that rarely have inclusions of pyrite. Both stages of sphalerite are associated with k esterite ( $\text{Cu}_2(\text{Zn,Ag})\text{SnS}_4$ ), which replaces Stage 1 sphalerite in patches while predominantly forming rims on Stage 2 sphalerite crystals (Plate 4.10c). Stage 1 sphalerite is replaced to some extent by fine-grained quartz and carbonate (Plate 4.10d). Fine-grained, relatively-pristine, Stage 2 sphalerite and k esterite can be found overgrowing fibrous barite. Stage 1 and Stage 2 sphalerite do not differ greatly in their iron-content (mean of 0.77 wt. %) or Cu-content (mean of 0.15 wt. %) (Table 4.3). Therefore they can only be distinguished on the basis of colour in plane-polarized light which could be attributed to trace element composition, and on the basis of crystal morphology (size, crystallinity, zoning). K esterite has consistent Sn, Cu and Ag content while its Zn and Fe content may vary.

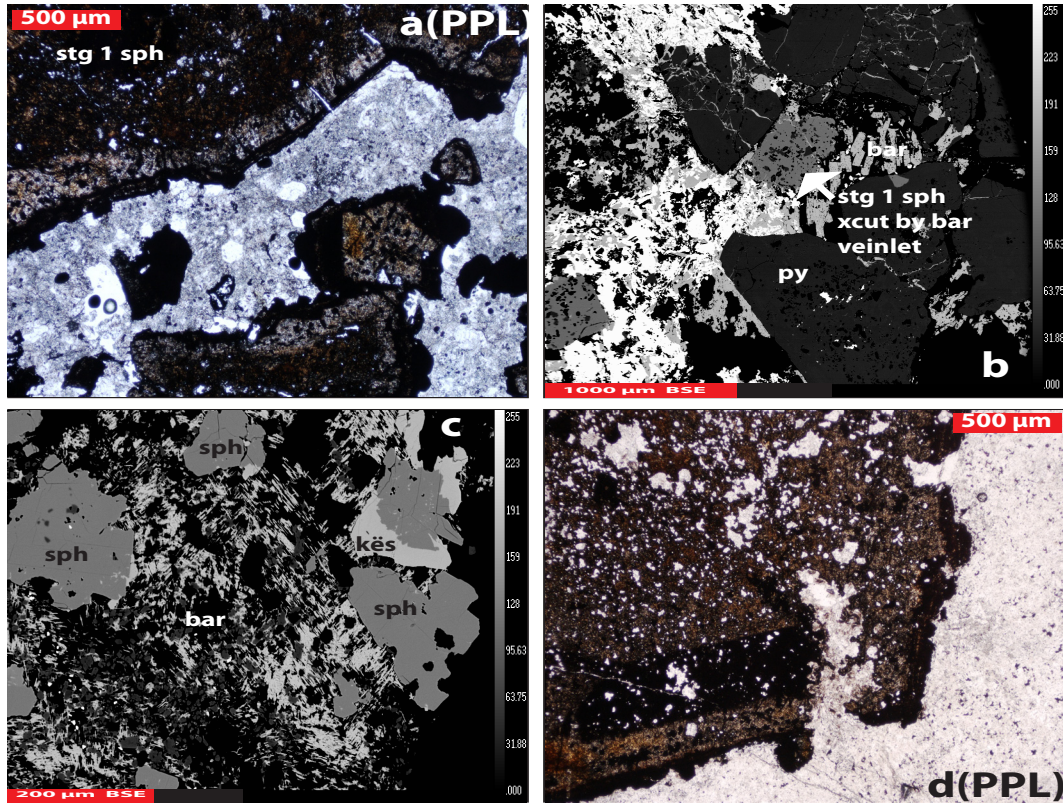


**Plate 4.10:** (a) coarse, zoned, orange-brown sphalerite rimmed by opaque k esterite with white quartz-carbonate gangue (H64.5B), (b) Stage 1 sphalerite (grey at centre of image) cross-cut by the same barite veinlets related to early galena mineralization (H64.5A), (c) BSE image of dark grey sphalerite and grey k esterite postdating fine-grained creamy-grey barite (H44.4A), (d) coarse, orange, zoned sphalerite crystal replaced by quartz-carbonate minerals (H64.5A).

#### 4.2.2 Paragenetic sequence of minerals at Hess:

The timing of hydrothermal mineral formation is clearly epigenetic (post-lithification) based on the petrographic evidence. A summary of the paragenetic sequence is presented in Figure 4.2. Early pyrite precipitation is followed by the formation of Stage 1 sphalerite and non-barium carbonates. Galena, barite, witherite and baryto-calcite  $\pm$  norsethite post-date or are broadly co-eval with Stage 1 sphalerite.

A second stage of hydrothermal mineralization then alters and overprints Stage one sphalerite and galena, this carries Zn, Pb, Cu, Sb, Sn and As ( $\pm$ Ag) sulphides and sulphosalts along with gangue quartz and fine-grained carbonates (ankerite, calcite, dolomite). Polymetallic mineralization corresponds to the formation of k esterite which replaces Stage 1 sphalerite and rims both Stage 1 and Stage 2

sphalerite. Second stage hydrothermal activity also results in the alteration of galena to cerrusite, and barite and witherite to a second phase of barytocalcite. These assemblages could correspond to either the evolution of a single hydrothermal system, or two distinct mineralizing events.

Mineral	Time of formation	
	Stage 1	Stage 2
<b>Sulphides:</b>		
Pyrite	██████████	
Sphalerite I (Fe-rich)	██████████	
Galena		██████████
Sphalerite II (Fe-Poor)		██████████
K�esterite		██████████
Geocronite		██████████
Franckeite		██████████
<b>Gangue:</b>		
Quartz	██████████	██████████
Barite		██████████
Barytocalcite		██████████
Witherite		██████████
Norsethite		██████████
Cerrusite		██████████
Calcite	██████████	██████████
Dolomite	██████████	██████████
Ankerite		██████████

*Figure 4.2: Paragenetic sequence of hydrothermal mineralization in Hess drill core*

## CHAPTER FIVE: GEOCHEMICAL RESULTS

### 5.1 NWT 'barren' barite geochemistry

The bulk geochemistry of forty-four samples was determined. The samples can be divided into: (1) Background Canol Formation sediments unrelated to barite mineralization (n = 4), (2) the Taiga section (n = 6) that does not contain any barite but is in close proximity to barite occurrences, (3) Canol Formation sediments devoid of visible barite at barite occurrences (n = 23) and (4) barite-bearing Canol Formation from the NWT (n = 11). The litho-geochemical data from all analyses can be found in Appendix C. Samples will be compared against the Post-Archean Australian Shale (PAAS) standard used by Taylor and McLennan (1985) in order to compare and contrast their geochemistry.

#### *5.1.1 Geochemistry of Late Devonian Canol Fm. sediments*

Major element oxides in background Canol Formation sediments (Table C1) have elevated  $\text{SiO}_2$  concentrations, lower  $\text{Al}_2\text{O}_3$ ,  $\text{Na}_2\text{O}$ ,  $\text{K}_2\text{O}$ ,  $\text{TiO}_2$  and  $\text{Fe}_2\text{O}_3$  (Total) concentrations and broadly similar  $\text{P}_2\text{O}_5$  and  $\text{MgO}$  concentrations compared to PAAS. Organic carbon concentrations ( $\text{C}_{\text{org}}$ ) range from 0.1 – 1.5 %. Sulphate concentrations are typically less than 1 % in samples. The two elements Ba and Sr which are major components of barite are relatively enriched in Canol Formation sediments, especially Ba which has concentrations orders of magnitude greater than PAAS concentrations (650 ppm). The transition metals (Cr, Ni, Cu, Zn, Pb,) have variable concentrations relative to PAAS. Elements that are enriched compared to PAAS include V, Mo, Th, and U while others such as Rb, Sc, Co, Zr and W are depleted. Overall REE concentrations in the Canol Fm. sediments are similar to PAAS.

The samples from the Taiga section (Table C2) are  $\text{SiO}_2$ -rich and have lower concentrations of major element oxides compared to PAAS and the background Canol samples.  $\text{C}_{\text{org}}$  concentrations range from 2 – 5 % in the Taiga samples and sulphate concentrations are slightly elevated (< 0.3 to 3.7 %). Samples are depleted in Rb, Cs and Sr but are enriched in Ba (2490 – 59660 ppm). There is an overall decrease in minor element and transition metal concentrations in Taiga samples with the exception of V, Mo and U. REEs are relatively depleted compared to PAAS.

Non-barite bearing Canol Formations shale from barite occurrences (Table C3) has the same major element oxide compositions as samples from Taiga. These samples are enriched in  $\text{C}_{\text{org}}$  (4 – 16 %) compared to both Taiga and background samples while overall sulphate concentrations are broadly similar. Samples are de-

pleted in Rb, Cs and Sr relative to PAAS, similar to both the background Canol Fm. and Taiga samples. Barium concentrations are very high (up to 90000 ppm). Trace elements and transition metals have similar concentrations to those from Taiga, once again with relative enrichments in V, Mo and U compared to PAAS. The REEs in these samples are relatively depleted compared to PAAS with a striking depletion in Eu similar to samples from Taiga.

Barite-bearing sediments are drastically different from all other samples. These samples (Table C4) are sulphate rich (30 – 40 % SO<sub>4</sub>) compared to all other types of samples. C<sub>org</sub> concentrations (1 – 8 %) are similar to those from Taiga and less than those from non-baritic samples within barite occurrences. Baritic samples also have much lower overall major element oxide concentrations with a dramatic decrease in SiO<sub>2</sub> concentration. While Rb and Cs concentrations are the same as all other samples, Sr is enriched (399 – 1628 ppm) in baritic samples. Barium has even higher concentrations in samples and some samples were outside the operating range of the instrument (500,000 ppm, 50 wt %). There is a dramatic decrease in trace element and transition metal concentration in baritic samples, even in V, Mo and U compared to all other samples and PAAS. REE totals are much lower than all other samples and show only a slight LREE enrichment compared to HREE concentrations. There is both enrichment and depletion in Eu in these samples compared to PAAS.

Cerium and Eu anomalies are a useful measure of the relative enrichment or depletion of these two redox-sensitive elements in a fine-grained sedimentary rock with respect to the rest of the REEs in the same sample and were calculated on the basis of the equations presented in Slack et al. (2004). Samples were normalized to the chondrite-composition of McDonough and Sun (1995). Where samples had detectable Eu concentrations, negative Eu anomalies are between 0.56 – 0.65 for background samples (with no samples below detection limits) and 0.10 – 0.51 for Taiga section samples (with one sample below the detection limits). Unmineralized samples from barite horizons have negative Eu anomalies ranging from 0.02 – 0.71 (nine samples below detection limits). Eight out of eleven barite-bearing samples were below detection limits for Eu. Of the remaining three, two have positive Eu anomalies from 1.35 – 3.03 and a single negative Eu anomaly of 0.57. Negative Ce anomalies for background shales range from 0.59 – 0.99, 0.67 – 0.88 for Taiga section samples, 0.44 – 0.98 for unmineralized shales at barite occurrences, and 0.34 – 0.86 for barite-bearing sediments.

Chondrite-normalized REE concentrations of individual samples were also

plotted (Fig 5.1). Shale and mudstone from the upper Canol Formation that is unrelated to barite mineralization has a pattern similar to PAAS. The Taiga section which is non-barite bearing but is spatially associated with the barite horizons in the NWT study area has compositions that mirror the overall shape of the PAAS curve but shows depletion in all REEs, most notably in europium (Fig 5.1b). Going from bottom to top of the Taiga section there is a drastic fluctuation in REE totals with the highest Eu and overall REE concentration found at the top of the section. Unmineralized sedimentary units within barite showings from the Canol Formation have the same patterns as the Taiga occurrence sediments (Fig. 5.1c) and have strongly negative Eu anomalies along with slightly negative Ce anomalies. Barite-bearing sediments have a drastically different ‘W-shaped’ REE pattern compared to other samples in this study (Fig 5.1d). These patterns are marked by negative Ce as well as both positive and negative Eu anomalies.

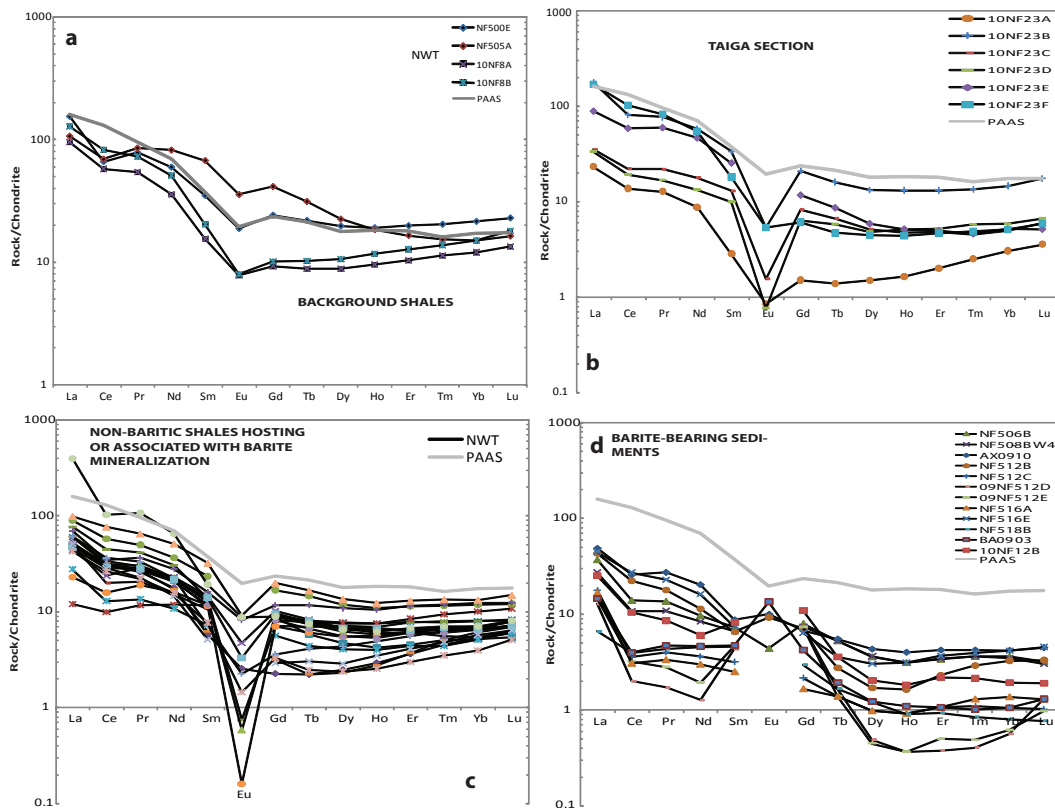


**Figure 5.1:** Chondrite-normalized REE plots of samples from the NWT. (a) Background samples, (b) Taiga section samples, (c) non-baritic samples in barite occurrences and (d) barite-bearing sediments. Thick grey line in all diagrams represents PAAS (Taylor and McLennan, 1995)

### 5.1.2 $\delta^{34}\text{S}$ and $\delta^{18}\text{O}$ isotope geochemistry of NWT barite

The results from analysis of the  $\delta^{34}\text{S}$  and  $\delta^{18}\text{O}$  isotope composition of NWT barite are presented in Table 5.1.  $\delta^{34}\text{S}$  values for laminated barite from the NWT range from +24 to +43 ‰ with a mean of +31.5 ‰ (n = 9).  $\delta^{34}\text{S}$  values from nodular barite range from +32 to +56.5 ‰ (one outlying sample at +4.8 ‰) with a mean of +41.3 (n = 22). Corresponding  $\delta^{18}\text{O}$  values for laminated barite range from +15 to +18.5 ‰ (one outlier at -0.5 ‰) compared to nodular barite which has a greater spread of  $\delta^{18}\text{O}$  values from +9 to +19 ‰. ‘Mixed’ samples with both laminated and nodular barite have a much smaller range of  $\delta^{34}\text{S}$  values (+28 and +32 ‰ for samples 10NF12A and 10NF17E respectively). Sample 10NF12C which contains epigenetic hydrothermal barite has  $\delta^{34}\text{S}$  and  $\delta^{18}\text{O}$  values of +24 ‰ and +11 ‰ respectively. Taken collectively, nodular- and laminated-barite from the NWT have overlapping isotopic compositions.

NWT barite	Texture	$\delta^{34}\text{S}$ (CDT)	$\delta^{18}\text{O}$ (vSMOW)		Texture	$\delta^{34}\text{S}$ (CDT)	$\delta^{18}\text{O}$ (vSMOW)
<b>10NF12C</b>	Hydrothermal	+23.9	+10.7	<b>Anita-508B</b>	Nodular	+33.2	+14.2
<b>10NF17D</b>	Laminated	+25.3	+15.4	<b>Ax-512B</b>	Nodular	+42	+12
<b>10NF7C</b>	Laminated	+35.3	+18.3	<b>Ax-512F</b>	Nodular	+43.1	+15
<b>Ax-09-02</b>	Laminated	+28.5	+16.7	<b>Ax-512J</b>	Nodular	+47.9	+15.4
<b>Ax-512C</b>	Laminated	+31.5	+16	<b>B1-02A</b>	Nodular	+35.3	+9.2
<b>Ax-512D</b>	Laminated	+24.1	+14.8	<b>B1-513B</b>	Nodular	+38.4	+16
<b>Ax-512E</b>	Laminated	+28.7	+15.9	<b>B2-02</b>	Nodular	+51.8	+17
<b>B1-04</b>	Laminated	+32.9	-0.5	<b>B2-515A</b>	Nodular	+52.1	+9.6
<b>B2-516A</b>	Laminated	+34.5	+17.3	<b>B2-516B</b>	Nodular	+50.4	+13.9
<b>BA-518E</b>	Laminated	+42.8	+18.8	<b>B2-516C</b>	Nodular	+45.9	+15.6
<b>10NF12A</b>	Mixed	+31.6	+17	<b>B2-516E</b>	Nodular	+47.8	+17.6
<b>10NF17E</b>	Mixed	+27.6	+15.7	<b>B2-516F</b>	Nodular	+56.5	+15
<b>10NF12B</b>	Nodular	+33.4	+17.6	<b>W1-506B</b>	Nodular	+46.5	+19.3
<b>10NF17B</b>	Nodular	+53.7	+18	<b>W3-506B</b>	Nodular	+31.5	+15
<b>10NF3A</b>	Nodular	+42.3	+16.9	<b>W4-506B</b>	Nodular	+4.8	+17.9
<b>10NF7D</b>	Nodular	+42.1	+17.8	<b>W5-506B</b>	Nodular	+33.7	+17.9
<b>10NF7F</b>	Nodular	+38.9	+15.7	<b>W6-506B</b>	Nodular	+36.5	+17.7

**Table 5.1:  $\delta^{34}\text{S}$  and  $\delta^{18}\text{O}$  values of NWT barite**

Cecile et al. (1983) analyzed barite from an assortment of lithologies in the Selwyn Basin including a number from Devonian-Mississippian strata in the

NWT that are similar in terms of their description, stratigraphic setting and that documented both barite laminations and nodules. Importantly, Cecile et al. (1983) also documented similar ranges of  $\delta^{34}\text{S}$  values for laminated barite (+23 to +30 ‰) and nodular barite (+42 to 53 ‰) hosted in “silver-white weathering siliceous basin shale or chert”.

The  $\delta^{34}\text{S}$  and  $\delta^{18}\text{O}$  values of barite from the NWT were plotted against the S and O-isotope curve of Claypool et al. (1980) assuming a late Devonian-age (360 Ma, Fig. 5.2a and b). The first observation is that barite from this study mirrors the worldwide evaporite enrichment in  $^{34}\text{S}$  during the late Devonian. However, the overall range in  $\delta^{34}\text{S}$  values in this study is far higher than documented global trends for seawater isotopic composition, even for some of the laminated barite samples

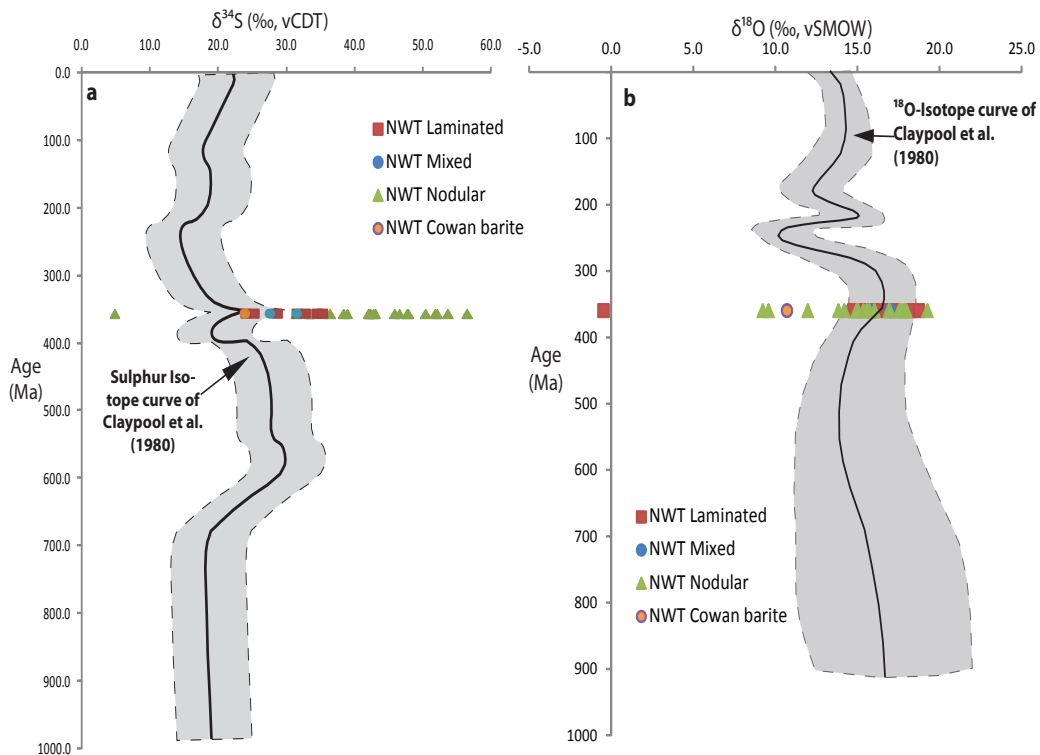


**Figure 5.2:** (a)  $\delta^{34}\text{S}$  (vCDT) and (b)  $\delta^{18}\text{O}$  (vSMOW) values of NWT barite plotted against the S- and O-isotope curves of Claypool et al. (1980).

## 5.2 Walt/Tyrala/Hess/Cathy ‘mineralized’ barite geochemistry

The bulk litho-geochemistry of four samples was analyzed. The samples can be divided into: 1. Background Portrait Lake Formation sediments unrelated to barite mineralization (n = 2), 2. Portrait Lake Formation sediments devoid of visible barite at barite occurrences (n = 1) and 3. laminated’ barite-bearing Portrait Lake

Formation from outcrop in the Hess claims (n=1). The data produced from these analyses is found in Appendix C and will be examined in similar fashion to lithochemical data from the NWT study area.

#### *5.2.1 Geochemistry of Middle Devonian Portrait Lake Fm. sediments*

The two background samples (Table C1) collected from the Walt/Tyrala/Hess occurrences have widely differing major element oxide compositions. One sample (10NF38A) has major element oxide compositions similar to those found in the NWT study area with the exception of  $\text{Fe}_2\text{O}_3$  which is considerably less than in NWT samples. The second sample (10NF32A) has low  $\text{SiO}_2$  (25 % of whole rock composition) and elevated CaO (20 % of whole rock) and MgO (11 % of whole rock) which are well above PAAS concentrations. The silica-rich sample has less  $\text{C}_{\text{org}}$  (2.3 %) compared to the carbonate-rich sample (7.8 %). There is no detectable sulphate in either of these samples. Both samples are depleted in Rb and Cs compared to PAAS, and are enriched in Ba with concentrations similar to background Ba sediment concentrations in the NWT. The carbonate-altered sample has higher Sr-concentrations compared to the Si-rich sample. The Si-rich sample has minor and transition element concentrations similar to samples from the NWT, and are also enriched in V and Mo. The carbonate-rich sample has notably higher concentrations of the elements Ni and Zn compared to the Si-rich sample which has slightly higher Pb concentrations. Overall REE concentrations in these samples are similar. The Si-rich sample and carbonate-rich sample have negative Eu anomalies of 0.56 and 0.69 respectively. There is a negative Ce anomaly of 0.73 for the Si-rich sample while the carbonate-rich sample has no Ce anomaly (0.99). Chondrite-normalized REE plots of these two samples has similar patterns to PAAS (Fig 5.3a).

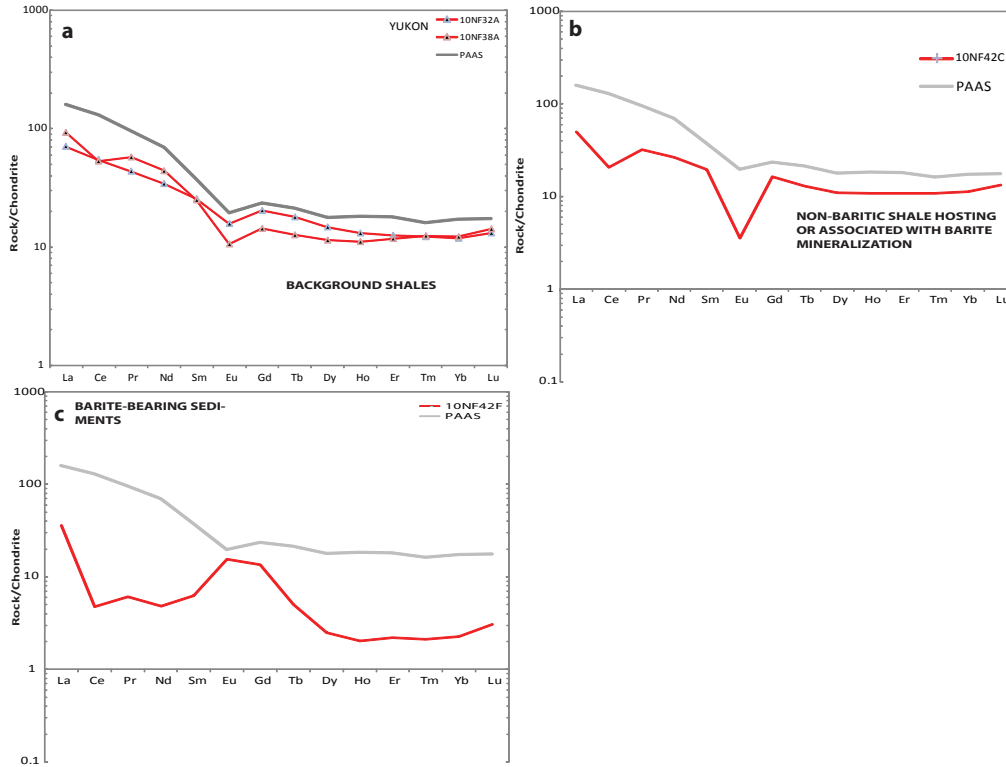


**Figure 5.3: Chondrite-normalized REE plots of samples from the Walt/Tyrala/Hess barite occurrences. (a) Background samples (10NF32A, 10NF38A), (b) non-baritic sample (10NF42C) in barite occurrence and (c) barite-bearing sample (10NF42F). Thick grey line in all diagrams represents PAAS (Taylor and McLennan, 1995)**

The non-baritic sample (10NF42C, Table C3) from outcrop hosting the Walt/Tyrala/Hess barite occurrence has the same major element oxide composition as non-baritic samples from the NWT as well as similar  $C_{org}$  and  $SO_4$  concentrations. The Ba concentration in this sample is also elevated similar to non-baritic samples from the NWT. Trace element and transition metal concentrations in this sample are also similar to NWT values with Pb, Zn and Sr being enriched in this sample compared to NWT and background samples. Chondrite-normalized REE concentrations in this sample are depleted compared to PAAS with notable negative Ce and Eu anomalies of 0.51 and 0.20 respectively (Fig 5.3b)

The barite-bearing sample from outcrop (10NF42F, Table C4) is similar in all aspects to baritic-samples from the NWT. The elements Sr and Zn have even further elevated concentrations in this sample. Chondrite-normalized REE concentrations in this sample show exactly the same pattern to those from baritic-samples

in the NWT with a negative Ce anomaly of 0.26. The sample has a large positive Eu anomaly of 1.68 (Fig 5.3c).

*5.2.2  $\delta^{34}\text{S}$  and  $\delta^{18}\text{O}$  isotope geochemistry of minerals from outcrop and Hess drill core*

The results from analysis of the S and O isotope composition of Yukon barite and sulphide are presented in Table 5.2.

Yukon barite	Texture	$\delta^{34}\text{S}$ (CDT)	$\delta^{18}\text{O}$ (vSMOW)	Hess Sulphides	Mineral	$\delta^{34}\text{S}$ (CDT)
<b>H64.5</b>	<b>Hydrothermal</b>	+19.3	+6.3	H45.0	<b>Pyrite</b>	+24.4
<b>10NF36B</b>	<b>‘Massive/ Laminated</b>	+23	+14.8	“	<b>Galena</b>	+25.4
<b>10NF37A</b>	<b>‘Massive/ Laminated</b>	+23.7	+17.2	H45.6	<b>Pyrite</b>	+23.1
<b>10NF40B</b>	<b>‘Massive/ Laminated</b>	+27.4	+17.2	“	<b>Galena</b>	+24.6
<b>10NF40C</b>	<b>‘Massive/ Laminated</b>	+22.2	+17.5	H46.2-carb	<b>Pyrite</b>	+24.5
<b>10NF40E</b>	<b>‘Massive/ Laminated</b>	+25.3	+19.6	H46.2-no carb	<b>Pyrite</b>	+24.4
<b>10NF40F</b>	<b>‘Laminated’</b>	+50.4	+18.3	H57.3	<b>Pyrite</b>	+28.4
<b>10NF42F</b>	<b>‘Laminated’</b>	+46.7	+21.8	H61.6	<b>Pyrite</b>	+25.1
				H62.4	<b>Pyrite</b>	+25
				“	<b>Galena</b>	+25.4
				H64.5	<b>Pyrite</b>	+25.3
				“	<b>Stg 1 Sphalerite</b>	+24.5
				“	<b>Galena</b>	+7.6
				H66.7	<b>Galena</b>	+26.1

**Table 5.2:  $\delta^{34}\text{S}$  and  $\delta^{18}\text{O}$  values of Yukon barite and  $\delta^{34}\text{S}$  values of Hess sulphides**

Walt/Tyralla/Hess barite:

‘Laminated’ barite from the Hess claims has a range of isotopic compositions that is broadly similar to the entire range of  $\delta^{34}\text{S}$  values seen in the NWT ( $\delta^{34}\text{S} = +19$  to +50 ‰,  $\delta^{18}\text{O} = +6.3$  to +22 ‰) even though no nodular barite was analyzed from the Yukon study area. Barite from the one Hess barite drill core sample (H64.5) has the lowest  $\delta^{34}\text{S}$  value (+19 ‰) of all samples analyzed as well as a markedly low  $\delta^{18}\text{O}$

value (+6 ‰). The  $\delta^{34}\text{S}$  and  $\delta^{18}\text{O}$  values of Yukon barite from outcrop and Hess drill core were plotted against the S and O-isotope curve of Claypool et al. (1980) assuming a late Devonian-age (360 Ma, Fig. 5.4a and b). The  $\delta^{34}\text{S}$  values of barite in outcrop form two distinct sets, one within the range +19 to +25 ‰, and the second from +46 to +50 ‰.

The isotopic composition of Devonian-Mississippian MacMillan Pass barite was first analyzed by Large (1981) who found  $\delta^{34}\text{S}_{\text{Barite}}$  had values ranging from +18 to +31 ‰ at the Tom Ba-Pb-Zn deposit. Gardner and Hutcheon (1985) documented  $\delta^{34}\text{S}_{\text{Barite}}$  values ranging from +22.9 to +26.8 ‰ at the Jason Ba-Pb-Zn deposit and also had  $\delta^{18}\text{O}_{\text{Barite}}$  values which fell in the range of Devonian seawater. Further work by Goodfellow (1987), Goodfellow and Jonasson (1984), and Goodfellow and Lydon (2007) defined a ‘Selwyn Basin barite and pyrite’ curve which more or less duplicated the shape of the evaporite age curve and showed regional enrichments in  $\delta^{34}\text{S}$  values. Yet this curve sometimes had  $\delta^{34}\text{S}_{\text{Pyrite}}$  values greater than that of coeval sulphate suggesting there were some temporal inconsistencies as to the sulphur sources for the pyrite analyzed.

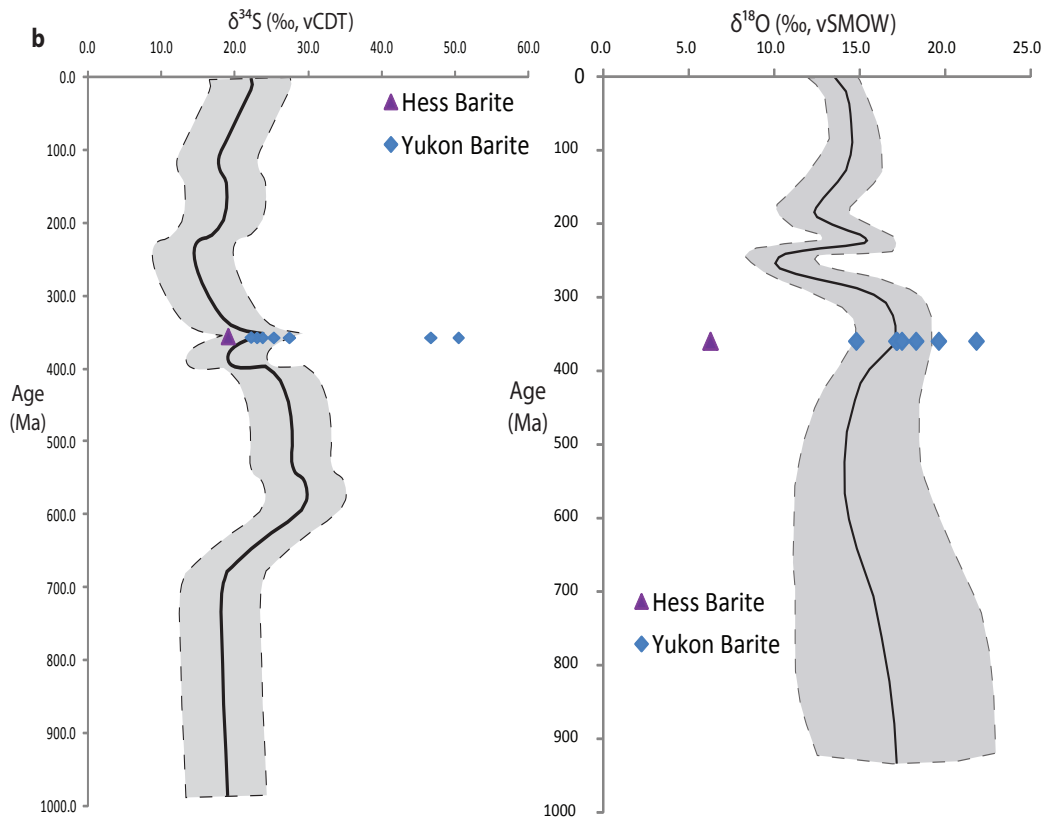


**Figure 5.4:** (a)  $\delta^{34}\text{S}$  (vCDT) and (b)  $\delta^{18}\text{O}$  (vSMOW) values of Walt/Tyralla/Hess barite plotted against the S- and O-isotope curves of Claypool et al. (1980).

The  $\delta^{34}\text{S}$  values for sulphides (vCDT) from the drill core range between +24 to +28 ‰ for pyrite, +23 to +26 ‰ for galena (one outlier at +7.6 ‰), and +24 ‰ for a single Stage 1 sphalerite sample. Co-existing, intergrown sulphides display similar  $\delta^{34}\text{S}$  values. However, these samples are isotopically-enriched in  $^{34}\text{S}$  compared to barite that is associated with base-metal mineralization in Hess drill core

### 5.2.3 Re-Os isotope systematics of Hess pyrite

Rhenium concentrations in pyrite from seven samples range from 3.144 to 20.020 ppb and Os concentrations range from 240.6 to 5071 ppt. The  $^{187}\text{Re}/^{188}\text{Os}$  ratios are between 16.51 and 93.8, and  $^{187}\text{Os}/^{188}\text{Os}$  ratios range from 0.8253 to 1.6001. The results and respective errors for each analysis are presented in Table 5.3.

Sample	$^{187}\text{Re}/^{188}\text{Os}$	$\pm 2\sigma$	$^{187}\text{Os}/^{188}\text{Os}$	$\pm 2\sigma$	rho	% Re	% $^{187}\text{Os}$	% $^{188}\text{Os}$
						blank	blk	blk
<b>H45.0</b>	21.62	0.1	1.025	0.002	0.141	0.07	0.01	0.04
<b>H46.2</b>	44.47	0.2	1.081	0.002	0.122	0.06	0.01	0.07
<b>H57.3</b>	93.8	0.46	0.825	0.002	0.329	0.2	0.11	0.47
<b>H61.6</b>	44.23	0.83	0.845	0.022	0.684	0.16	0.04	0.17
<b>H62.4</b>	20.86	0.1	0.867	0.002	0.197	0.11	0.01	0.06
<b>H64.5</b>	75.05	0.52	1.600	0.009	0.563	0.57	0.13	1.06
<b>H66.6</b>	16.51	0.1	0.851	0.005	0.321	0.37	0.04	0.15

**Table 5.3: Re/Os isotopic data for pyrite from Hess drill hole.**

The data obtained do not yield a robust isochron and therefore cannot be used to date Hess pyrite. Simple two-point isochrons were calculated for pyrite using Isoplot/Ex (Ludwig, 2000). Data generated from these calculations were eliminated if pairs of pyrite gave a negative age of formation or if the calculated age was smaller than error. These data are plotted in Figure 5.5a. Based on the data, the calculated initial  $^{187}\text{Os}/^{188}\text{Os}$  ratios for individual pyrite pairs fall largely in the range 0.58 to 0.79. There is one outlier that has a calculated initial  $^{187}\text{Os}/^{188}\text{Os}$  ratio of  $0.33 \pm 0.015$ .

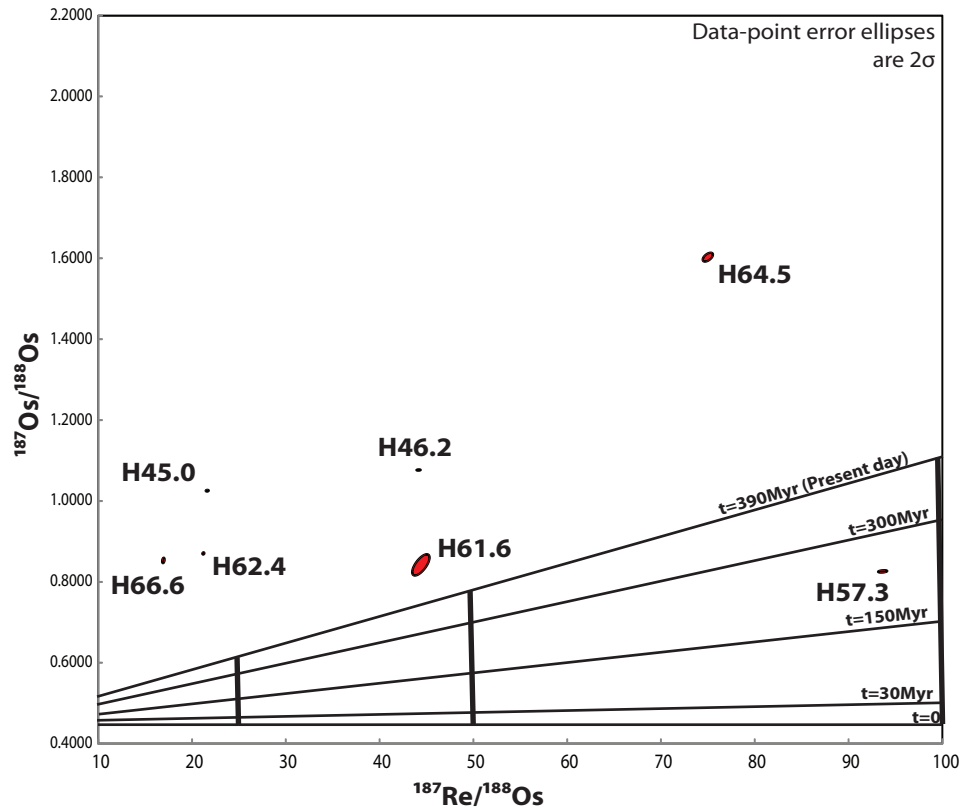


**Figure 5.5:** *Re-Os data for Hess pyrite plotted on a graph of  $^{187}\text{Re}/^{188}\text{Os}$  versus  $^{187}\text{Os}/^{188}\text{Os}$ . Shaded ellipses are the error  $2\sigma$ . Plotted using Isoplot (Ludwig, 2000)*

The theoretical evolution of the Re-Os systematics of a middle Devonian black shale (the conodont-derived age of the Cathy sediments, ~390Ma, Chapter 2) were calculated for 5 Ma time increments and initial  $^{187}\text{Re}/^{188}\text{Os}$  ranging from 10 - 500. This was done by assuming that their initial  $^{187}\text{Os}/^{188}\text{Os}$  was ~0.45 which is thought to be a good estimate for the composition of Devonian seawater that was coeval with these shales (Selby and Creaser, 2005; Turgeon et al., 2007). The results from these calculations are shown in figure 5.5b with data to be found in Appendix D.

## CHAPTER SIX: DISCUSSION

### 6.1 NWT ‘barren’ barite

#### 6.1.1 The stratigraphic position of synsedimentary-diagenetic barite

The presence of 25 – 75 m thick sediment-hosted barite sequences in the upper part of the Canol Formation in the NWT, close to the contact with the Imperial Formation implies not one, but two changes in the types of sedimentation in the Selwyn Basin at this time (Fig. 6.1). The bulk of the Earn group consists of siliceous mudstone and shale which is then overlain conformably by the sediment-hosted barite occurrences documented in this study. These are then overlain unconformably by the debritic sandstones and turbidites of the Imperial Formation.

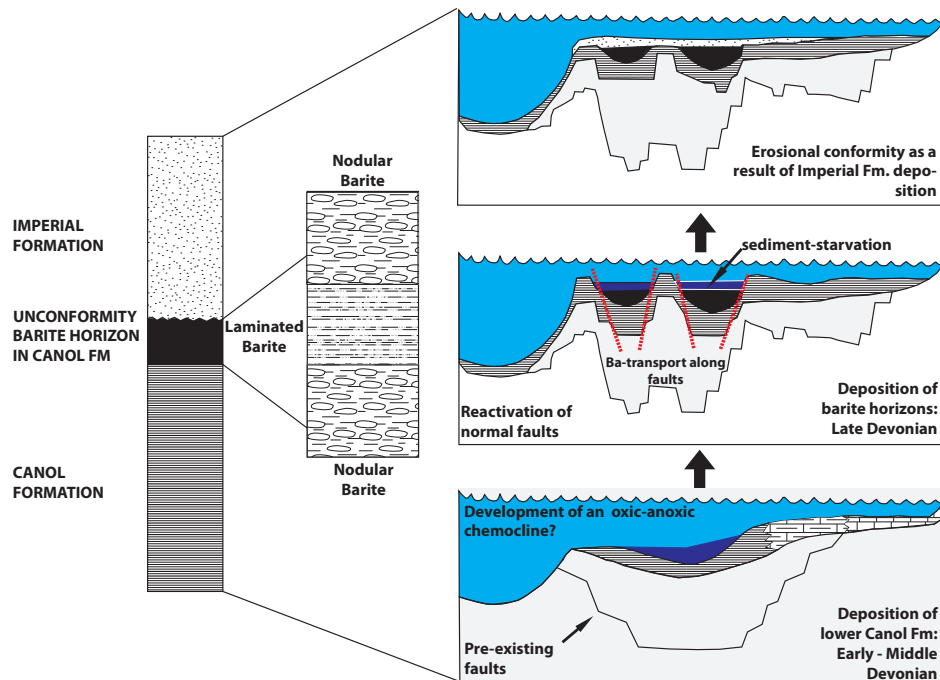


**Figure 6.1:** Stratigraphic position of barite horizons in the Earn Group, NWT

Basinal shales are universally recognized to represent periods of quiet, basin deposition with pelagic and hemipelagic clays making up the bulk of the sediment composition (Stow et al., 2001), along with variable amounts of quartz and accessory minerals (apatite, monazite, authigenic feldspars, Potter et al., 1980). In a study of the Canol Formation by Al-Aasm et al. (1996), the sediments were thought to represent an “anoxic, relatively deep-water (10s to 100s of metres), basinal facies association”. They also concluded that shallowing-upwards conditions existed during deposition of the Canol Formation followed by termination of anoxic condi-

tions which were replaced by slightly oxygenated, dysoxic waters. This organic-rich shale and mudstone stratigraphy matches observations of the lower Canol Formation below the sediment-hosted barite horizons.

The conformable transition of non-baritic to barite-bearing Canol Formation represents a higher rate of barite precipitation compared to sediment deposition and the onset of hydrothermal activity in the Selwyn Basin. This study has shown that this barite mineralization is hosted in the uppermost parts of the Canol Formation. The overlying Imperial Formation represents a drastic change in depositional setting as turbidites and debrites are linked to basinal slope environments. These coarse-grained, quartz-rich lithologies are indicative of weathering of continental (landward) sources which were then deposited in much shallower environments as turbidity flows. However, as the Imperial Formation overlies the Canol Formation unconformably, the gap in time between cessation of barite deposition and initiation of Imperial Formation clastic sedimentation is unknown.

Taken as a whole, barite occurrences in the NWT represent a marker horizon, up to 75 m thick in places, throughout the Earn Group. These barite horizons have three components: 1. laminated barite and host sediments, 2. nodular barite and host sediments and 3. non-baritic shale or mudstone.

Interlaminated barite and upper Canol Formation sediments are clear evidence of repeated cycles of pelagic and chemical sediment deposition that took place in the water column when a Ba-rich hydrothermal fluid reached the sediment-water interface (SWI). Laminated barite units in Canol Formation sediments are typically 100 – 200  $\mu\text{m}$  thick and indicate a very restricted pelagic clay supply. This can be interpreted as an indicator of sediment-starvation in the Selwyn Basin. Furthermore, the complete lack of bioturbation and fossils, combined with high fissility in Canol Formation sediments in barite horizons is proof of a quiet, sub-wave environment during sedimentation.

It is important to re-assert the fact that the bulk of the textures observed however are nodular and therefore were precipitated below the SWI (Sellés-Martínez, 1996). Laznicka (1976) documented the occurrence of such nodules in what he called Devonian-Mississippian carbonaceous shale and dolomitic limestones in the Twitya River Area, NWT. While his petrographic description bears a passing resemblance to some of the textures observed, the stratigraphic position of the units is not clear.

The Cowan barite occurrence most closely resembles what might be considered a source or vent for fluids that precipitated barite in the study region in the

NWT. The epigenetic barite in samples from Cowan is morphologically distinct from diagenetic barite nodules in other occurrences. The ~ 70 m long (along strike) horizon at Cowan is interpreted to be a synsedimentary fault that hydrothermal fluids were transported along. But it is uncertain and improbable that this was solely responsible for barite deposition in the study region. The presence of nodular and laminated barite textures within samples from the same outcrop could be evidence of synsedimentary faulting that Goodfellow and Lydon (2007) have proposed for hydrothermal fluid conduits. Further exploration for and within these structures is needed in order to assess their metal-bearing capacity.

#### Barium silicates and diagenetic processes

This study has identified barium silicates in Selwyn Basin strata from the NWT for the first time. The key barium silicates (hyalophane and cymrite) found in this study are present in both laminated and nodular barite samples, euhedral and replaced to some extent by barite. Electron microprobe analysis of hyalophane composition also indicates that there is no major difference in major element composition between feldspars from laminated and nodular barite samples. Hyalophane and cymrite are preferentially concentrated close to barite-sediment boundaries. The only observable difference is that hyalophane is more common in nodular barite compared to laminated barite. This would imply that barium feldspars from the NWT study area are products from diagenetic alteration of barite.

Diagenetic hyalophane in shales has been rarely documented in systems not associated with Ba-Zn-Pb mineralization, such as in Ordovician sediments from Norway (Bjorlykke and Griffin, 1973) and unmetamorphosed sediments from Greenland (Jakobsen, 1990). Bjorlykke and Griffin (1973) proposed that reducing environments with organic carbon could supply the conditions necessary to dissolve barite but did not comment on the sources of other elements to form hyalophane. Finlow-Bates (1987) first commented on the unusual barium-mineral assemblages present in the MacMillan Pass Ba-Pb-Zn deposits and a number of other worldwide occurrences and postulated that minerals such as celsian, hyalophane, cymrite and barium-carbonates were the result of exhalative barium depleting the sulphate budget in basins to the point that the stability field(s) of other barium minerals was reached.

The sub-linear range of feldspar compositions indicates a single heterogeneous source of the elements K, Al and Si in this system (Figure 4.1). Shales are well known to have high concentrations of these elements as a result of their min-

eralogy being dominated by clays and quartz (Potter et al., 1980). The sulphate-depleted conditions below the SWI and elevated temperatures from hydrothermal fluids, or burial of the sediments to depth provide an excellent source for the elements necessary for feldspar formation. Late diagenesis is preferred as a mechanism for formation of feldspars in this study because of their ubiquitous nature in both laminated and nodular barite. There are no K-feldspars and very little quartz in the barite laminations or nodules which one would expect if there was a hydrothermal source for K and Si.

In general, late diagenesis occurs at depths greater than 1.5 km under conditions of elevated temperature in the range 50 – 300°C (Milliken, 2004). Dissolution of clay minerals such as smectite which takes place in the temperature range 60 - 140°C can generate significant amounts of K, Al and silica in pore waters in shales (Milliken, 2004). These elements reacted with Ba in a sulphate-depleted environment to form hyalophane and cymrite. The preferential concentration of barium silicates along barite-sediment boundaries is a reflection of crystallization along chemical boundaries. Barium nodules have more surface area and therefore can form barium silicates more readily from pore water fluids. The replacement of all barium silicates by secondary barite may reflect destabilization of hyalophane and cymrite as a result of more oxidized pore waters from an unknown source.

#### *6.1.2 Basin geochemistry and geochemical processes during formation of barite horizons in the upper Canol Fm.*

The simplest way to model the geochemical processes that operate in basins and their associated oceans is to set up a box which has inputs, outputs and associated fluxes of elements and the minerals or fluids that host or transport them. The major inputs include detrital components, biogenic components (both organic matter (OM) and mineralized microskeletal remains) derived from primary photosynthetic production and heterotrophic processes on land and in the sea, and authigenic material precipitated at or near the SWI as a consequence of Eh-pH-controlled organic and inorganic reactions (Sageman and Lyons, 2004). Based on our observations and interpretations of the upper Canol Formation and baritic strata, the detrital components would include clays, organic matter and chemical sediments i.e. laminated barite. Authigenic material would include nodular barite and diagenetic feldspars.

The deep ocean today is well oxygenated thanks to a “conveyor-belt” circulation that carries cold, oxygen-rich waters from high latitudes to the distant reaches of the abyssal zone. This condition is less robust than one may think; today, half of

the oxygen injected into the deep sea in the North Atlantic deep-water formation regions is consumed during the decomposition of organic detritus settling through the water column (Meyer and Kump, 2008). The Selwyn Basin was a restricted basin (this study, Goodfellow, 1987) which would have prevented oxygenated waters from cycling down to depth to decompose organic matter, leading to depleted oxygen levels at depth, and eventually to anoxia.

One of the great challenges is distinguishing between locally and globally anoxic or euxinic conditions. During particular intervals of Earth history known as oceanic anoxic events (OAEs), the deep ocean indeed became oxygen depleted. Under oxygen-free conditions, microbes reduce alternate electron acceptors during decomposition. After the trace metal and nitrate reservoirs are depleted, bacteriogenic sulphate reduction (BSR) ensues (Konhauser, 2007). This is a temperature sensitive process and sulphate-reducing bacteria are viable between 0 – 100°C (Goldhaber, 2004) and can probably survive up to a maximum temperature of about 120°C (Machel, 2001; Machel et al., 1995). In many OAEs then, anoxia evolved into euxinia, a state in which hydrogen sulphide concentrations built up to toxic levels in deep waters. Major pathways and reactions are summarized in Figure 6.2.

The geochemistry of these barite horizons in the upper parts of the Canol Formation can be used to understand the geochemical composition and redox conditions of the Selwyn Basin during their deposition. These inferences are made based on the interpretation that the barite horizons were precipitated both above and below the SWI in unlithified pelagic sediments.

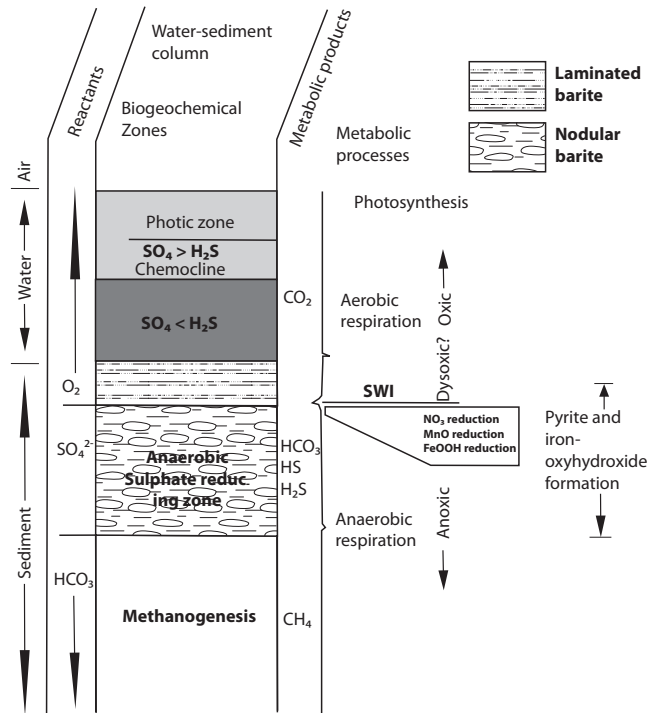


**Figure 6.2: Schematic depth zonation of biogeochemical processes in marine sediments applied to barite-forming environments (adapted and modified from Goldhaber, 2004).**

Lithogeochemistry of Canol Formation shale and barite horizons:

Trace element concentrations in shale and mudstone can be used to assess the geochemical environment that pelagic minerals were deposited in as well as the effect of diagenetic processes (e.g. Lev et al., 1999; Piper, 1994). REEs in shales can be used to delineate clastic sediment provenance (Bhatia, 1985), track the evolution of the continental crust (Taylor and McLennan, 1985), and even to understand elemental mobility in sedimentary rocks during processes such as burial and metamorphism (Lev et al., 1999). Combined with stable isotope data, the trace element and REE data from this study provides a powerful tool to track geochemical changes in the Selwyn Basin during the deposition of these barite horizons.

The lithogeochemistry of the background Canol Formation samples can be used as a baseline to track changes in basin chemistry. Sedimentary rocks associated with barite occurrences, such as at Taiga or within barite occurrences themselves; are extremely Si-rich and depleted in CaO and MgO. This implies that these sediments were deposited in the deepest parts of the basin away from a marine carbonate shelf. The low concentrations of components such as  $Al_2O_3$ ,  $Fe_2O_3$  and

TiO<sub>2</sub> and Zr may also indicate that the supply of these elements derived from continental weathering was also limited. The concentration of planktonic organic carbon in these samples is high compared to background levels. Since sedimentation rates were low, this could be correlated with increased production of organic matter as opposed to increased preservation. Trace element and transition metal concentrations in the same samples are extremely variable and show both enrichment and depletion. Redox sensitive elements such as Mo and V are enriched in non-baritic samples. While these elements are concentrated in organic-mudrocks deposited in anoxic environments (Crusius et al., 1996), it is thought that Mo (and possible V) concentrations should actually decrease in anoxic conditions due to their utilization by microbial biological processes (Meyer and Kump, 2008). The enrichment of Ba and relative paucity in sulphate means that the sulphate supply in the Selwyn Basin was limited and confirms that the basin may not have been connected to the open ocean. Most importantly, the elements Zn and Pb are often below PAAS concentrations even though Ba concentrations are extremely high in non-baritic samples. This may mean that the source of Ba in the Selwyn Basin at the time of barite precipitation carried no significant quantities of Pb or Zn, or that these elements were lost earlier.

Shale and mudstone from both the NWT study area which are unrelated to barite mineralization have REE compositions similar to the PAAS standard (Fig. 5.1a). The Taiga section which is non-barite bearing but is spatially associated with the barite horizons in the NWT study area has compositions that mirror the overall shape of the PAAS curve but shows depletion in all REEs, most notably in Eu (Fig. 5.1b). Going from bottom to top of the Taiga section there is a drastic fluctuation in overall REE concentration with the highest Eu and overall REE concentration found at the top of the section. Unmineralized sedimentary units within barite showings have the exact same patterns as the Taiga occurrence sediments (Fig. 5.1c) and have strongly negative Eu anomalies along with slightly negative Ce anomalies.

Barite-bearing sediments are enriched in Sr compared to other samples which is expected as Sr is a common trace element in sulphates (Hanor, 2000). The overall depletion in major element oxides in baritic samples is correlated with decreased clay content relative to an increase in barite. Baritic samples have even lower trace element and transition element concentrations, including Zn, Pb, Mo, V and U; compared to all other samples. These data again indicate that Zn and Pb were not associated with Ba-bearing fluids. The decrease in Mo and V could be attributed to a decrease in absorptive minerals such as clay, but also could be the re-

sult of increased microbial activity as a result of higher organic carbon production. Barite-bearing sediments display a drastically different REE pattern from all other analytes in this study (Fig. 5.1d).

The stratigraphic correlation in REE patterns among the samples from sedimentary rocks from unmineralized and mineralized upper Canol Formation sediments in the Selwyn Basin leads to the inference that geochemical conditions were one and the same during deposition.

According to McLennan (1989), most continental margin sediments display “intermediate REE abundances, variable LREE enrichment and variable negative Eu-anomalies, with  $\text{Eu}/\text{Eu}^*$  in the range of 0.60 – 1.00”. Non-barite bearing shales spatially associated with and in barite horizons show slight to moderate light rare earth element (LREE) enrichment compared to heavy rare earth elements (HREEs), coupled with an overall REE pattern that is moderately to severely depleted compared to the PAAS standard. Some major REE sources in shale are detrital or diagenetic phosphate phases such as apatite, monazite and allanite (McLennan et al., 2003). Diagenetic apatite is thought to form under sulphate-reducing conditions as a result of dissolution of biogenic phases and detrital apatite (Curtis, 1980). Overall phosphate levels in almost all these samples is well below the PAAS  $\text{P}_2\text{O}_5$  concentration level which implies that there was less phosphate in the sedimentary environment. The loss or non-deposition of phosphate minerals can be used to explain the overall depletion in REE concentrations in samples from this study.

Cerium and Eu can behave differently from the other REEs because they have two oxidation states, +3 and +4 for Ce and +2 and +3 for Eu. In even a mildly reducing environment Eu can occur in the divalent oxidation state (Bau, 1991). Sverjensky (1984) modeled the behavior of Eu under a variety of temperatures, pressures, oxygen fugacities and pH, and determined that at 25°C it would require highly reducing and alkaline conditions to form  $\text{Eu}^{2+}$ . Bau (1991) found that at a pH of 3 and a pressure of 1000 bars that it would take elevated temperatures caused by hydrothermal fluids or severely reducing conditions to stabilize  $\text{Eu}^{2+}$ . A much more reducing environment combined with the effects of lowered pH would cause  $\text{Eu}^{2+}$  to be the dominant cation in solution compared to  $\text{Eu}^{3+}$ .  $\text{Eu}^{3+}$  would normally be preferentially taken up by clay minerals even in normal marine conditions and, therefore, reducing conditions would result in slightly negative Eu-anomalies such as those described by McLennan (1989).

In oxic conditions, Ce is less readily dissolved in seawater so that oxygenated seawater is more depleted with respect to Ce, whereas oxic sediments should

be more enriched with respect to Ce (Wilde et al., 1996). The opposite effect should therefore be expected in reducing environments and is manifested by the negative Ce-anomalies obtained in this study.

Baritic samples are markedly depleted in REEs compared to the host units as a result of their lack of detrital and authigenic phosphate minerals that concentrate REEs. The HREEs are depleted relative compared to the LREEs which is consistent with ions similar in radius to that of  $Ba^{2+}$  preferentially substituting into barite. An argument could be made that diagenetic hyalophane and barium silicates could account for the positive Eu-anomalies in a few of the samples. However all barite samples, whether laminated or nodular, have appreciable amounts of hyalophane  $\pm$  cymrite which does not account for the large number of samples with Eu under detection limits. The  $Eu^{2+}$  ion is most similar to Ba of all the rare earths in both charge and size and, therefore, should be more enriched in barite.

The composition of samples with no detectable amounts of Eu is perplexing and may mean that there are still  $Eu^{3+}$  ions in solution which could be a result of temperature decrease. Guichard et al. (1979) conducted the only study available on the REE composition of marine and continental barite and found a characteristic 'V-shape' in their patterns but their overall concentrations do not match those from this study (10 – 100 times chondrite composition). Also, Guichard et al. (1979) did not have any negative Ce-anomalies. They rationalized their lack of Ce anomalies in barite to their subsurface sedimentary formation with some incorporated REE coming from the host sediment supplies. The negative Ce-anomalies in this study indicate that reduced, soluble Ce ions were in seawater during the time of deposition and barite precipitated during this time was depleted in Ce.

Based on litho-geochemical data from this study, the Selwyn Basin was indeed a restricted basin where dysoxic to anoxic conditions prevailed as a result of a limited sulphate supply.

Sulphur and oxygen isotope geochemistry of synsedimentary barite, NWT:

The sulphur isotope data for evaporites from the Devonian show a notable decrease in  $\delta^{34}S$  values in the Early Devonian (down to  $\sim +15\%$ ), followed by a sharp enrichment in  $^{34}S$  isotopes ( $\delta^{34}S$  up to  $+30 - 35 \%$ , Claypool et al., 1980). This is followed by steady decrease of  $\delta^{34}S$  to roughly  $15\%$  for most of the Carboniferous.

The overall range in  $\delta^{34}S$  values in NWT barite in this study is far higher than documented global trends for seawater isotopic composition during the Late Devonian, even for some of the laminated barite samples which were precipitated

in the water-column. Such a spread in data again suggests a limited source of dissolved sulphate in the Selwyn Basin at this time in order to produce this degree of isotopic fractionation.

NWT synsedimentary laminated barite has  $\delta^{34}\text{S}$  values that on the lower-end fit into the range for seawater sulphate, but has no observable mineralogical differences to the samples that have higher  $\delta^{34}\text{S}$  values (up to +43 ‰). Diagenetic, nodular barite which formed under the SWI has extreme enrichment in  $^{34}\text{S}$ . Each of the stratigraphic sections measured documents the presence of large, fine-grained carbonate nodules within barite horizons. If these nodules were formed by the process of thermochemical sulphate reduction (TSR), one would expect coarse-crystalline cements and/or replacement masses after anhydrite, or dolomite formation (Machel, 2001) which is not the case. Therefore the geochemical process that created the spread in  $\delta^{34}\text{S}$  values in NWT barite was BSR.

Open-system bacterial reduction of seawater/porewater  $\text{SO}_4^{2-}$  to  $\text{H}_2\text{S}$  and  $\text{HS}^-$  preferentially utilizes  $^{32}\text{S}$  resulting in the formation of  $\text{S}^{2-}$  with a  $\delta^{34}\text{S}$  signature lower than its source. Rare, fine-grained pyrite crystals intergrown with both laminated and nodular barite could have been formed as a result of BSR. The litho-geochemistry of samples and elevated  $\delta^{34}\text{S}$  values for both laminated and nodular barite indicate a closed-system with respect to sulphate.

$\delta^{18}\text{O}$  values for barite from the NWT mostly fall within the range of values for Devonian seawater. The kinetics of sulphate-water oxygen isotope exchange is sluggish except under the most acidic conditions (Seal et al., 2000) and should be able to preserve a record of the source of oxygen (seawater vs. porewater vs. hydrothermal fluids). However the overlap of the  $\delta^{18}\text{O}$  values only indicates that oxygen isotope fractionation processes in barite in the Selwyn Basin may have been similar as a result of a common geochemical environment, but cannot be attributed to a single geochemical process. Laminated and nodular barite have almost the same range of  $\delta^{18}\text{O}$  values suggesting there is no distinction between seawater or porewater sources for oxygen.

Epigenetic, hydrothermal barite from Cowan however has markedly lower  $\delta^{18}\text{O}_{\text{Barite}}$  values compared to the bulk of barite analyzed in this study. Barite from the Cowan occurrence also has morphological characteristics (epigenetic, 20 – 75  $\mu\text{m}$ , tabular barite crystals) and a  $\delta^{34}\text{S}$ -isotope value that Paytan et al. (2002) have ascribed to hydrothermal sources. This may reflect the isotopic composition of a fluid that contained sulphate but was unrelated to seawater.

### *6.1.3 Geochemical comparisons with modern environments*

Interpretation of ancient black shale deposits has been strongly influenced by observations of modern environments where organic-carbon (OC)-rich mud presently accumulates. Modern analogues for black shale-forming environments are classified on relative water depth, and the nature and position of the redox boundary and its effect on benthic communities. Arthur and Sageman (1994) broadly defined these categories as: (1) deep, enclosed, strongly stratified basins, characterized by a redox boundary high in the water column and long-term anoxia throughout much of the basin; (2) deep, unenclosed basins in which dysoxic conditions predominate and the redox boundary normally remains at some depth within the substrate, but may fluctuate up and down; (3) shallow, stratified basins that are subject to frequent mixing by storms in which dysoxic to oxic conditions predominate, and the redox boundary normally remains at some depth within the substrate but may fluctuate above and below the sediment-water interface (SWI); and (4) shallow-water areas in which the water column is dysoxic to fully oxic, but the sediments are highly OC-rich and reducing.

Epeiric seas are epicontinental seas that develop when craton interiors are flooded during transgressions and sea level highstands. Because modern environments of organic-rich sedimentation include examples of either relatively deep basins or relatively shallow environments it is not surprising that one of the longest running geological debates has focused on the relative depth of black shale deposition. However, many epicontinental black shales have characteristics that are inconsistent with those of most modern low oxygen environments (Sageman and Lyons, 2004). Water depths in such seas probably varied from less than 100 m to not significantly more than 300 m (Sageman and Lyons, 2004). The closest modern analogues to the Selwyn Basin are the Black Sea and Framvaren Fjord (both in Europe) have chemocline depths of 120 – 180 m and 18 m respectively (Meyer and Kump, 2008). But the depth of the chemocline in the Selwyn Basin during the deposition of the barite sequences remains unclear. Paleogeographic reconstructions of the North American continent during the late Devonian indicate that the Selwyn Basin was very close to the equator (e.g. Blakey, 2003), unlike the current position of the Black Sea which would certainly have affected the depth of the chemocline during this time.

The upper part of the Canol Formation i.e. the sedimentary rocks associated with baritic strata, is not particularly phosphate rich and varies between 1 - 5

weight percent organic carbon. Barite-bearing Canol Formation rocks are organic carbon-poor. These observations are consistent with slow pelagic sedimentation and organic sequestration in between periods of hydrothermal activity. The total iron content of the same samples is also usually far below those of various standards such as PAAS (Taylor and McLennan, 1985) and North American Shale Composite (NASC, Gromet et al., 1984) and is correlated with the paucity of observed pyrite (crystals or framboids) in upper Canol Formation sediments themselves. Pyrite framboid size is often used as an indicator of anoxia in the water column (Wilkin et al., 1997; Wilkin and Barnes, 1997). However most iron minerals in this study are in the form of oxyhydroxides which cannot be used in this way. One reason for the lack of Fe-minerals could be that iron supplies were limited as a result of sediment starvation.

There are modern continental margins where barite is currently being deposited such as off the coasts of Peru and Japan in cold methane seeps (Torres et al., 1996a; Torres et al., 1996b), and in active continental rift margins such as the Southern California Borderland (Hein et al., 2007). There are no recent environments that have laminated and nodular barite textures that match those observed in the Canol Formation. Hein et al. (2007) analyzed massive- to breccia-type barite and ‘cold-seep’ type barite samples from a tectonically active basin with a known geothermal anomaly. One result from this study was that barite, metres away from a known hydrothermal vent had elevated  $\delta^{34}\text{S}$  values even in a non-restricted, oxygenated sub-basin in the Southern California Borderland, and that the range of  $\delta^{34}\text{S}_{\text{Barite}}$  values in the study was +20 to +60 ‰. Lithogeochemical analyses of the barite samples had Ag < 5 ppm, Pb < 2 ppm and Zn < 50 ppm. This may indicate that the Ba-bearing hydrothermal fluids in these systems are from a separate source than those that transport Ag, Pb and Zn.

Hein et al. (2007) also analyzed the REE composition of barite, which in their study shows almost flat patterns with no detectable concentrations of europium. Their negative europium anomalies and low overall REE concentrations are the only commonalities with data acquired in this study. While they did not comment on their REE patterns directly, their conceptual model infers the crystalline basement of the basin as the barium- and REE- source for hydrothermal fluids that formed their barite deposits.

## **6.2. Walt/Tyralla/Hess mineralized barite, Yukon**

To-date, conodont biostratigraphy has been the only age-dating technique used to constrain the timing of deposition of the sediments that host stratiform Ba-Pb-Zn mineralization in the lower Earn Group in the Kechika Trough in the Gataga District, British Columbia (Paradis et al., 1998 and references therein), in parts of the Selwyn Basin (Cecile, 2000 and references therein) and in the MacMillan Pass District (Irwin and Orchard, 1991). Results from these studies indicated a Frasnian (385 to 374 Ma) age for Selwyn Basin strata whereas conodont-ages from the Gataga District yielded a Fammenian (374 to 360 Ma) age. Irwin and Orchard (1991) record Eifelian to early Frasnian (395 – 375 Ma) conodonts from the Cathy deposit in the Yukon (part of the Walt/Tyralla/Hess occurrences) They also concluded that the sediments hosting the nearby Tom and Jason SEDEX deposits were no older than those at Cathy and that there were a number of barren barite deposits that had a middle to upper Frasnian age. The middle Devonian age derived from the conodont data suggests that the sediments hosting the Cathy deposit are older than the occurrences examined in the NWT. Turner and Rhodes (1990) postulated that the Cathy occurrence was an ‘exhalative barite deposit’ based on the assumption that the barite at Cathy was coeval with sediment deposition. This study suggests that in fact the barite is epigenetic and the mineralization, therefore, is younger than host units. The barite occurrences in the Yukon are highly deformed and may occur in a series of repeated fault slices as a result of the formation of the MacMillan Fold Belt (Abbott and Turner, 1990). This folding and faulting has caused remobilization of the barite which in turn has destroyed most primary textures. However, the sulphates and sulphides examined in the Hess drill core were clearly deposited post-lithification of host Portrait Lake Formation rocks.

### *6.2.1 Lithochemistry of middle Devonian Portrait Lake Formation sediments*

There is a difference in major element oxide geochemistry and trace element geochemistry of the two background samples. The least-altered Si-rich background shale and non-baritic Portrait Lake Formation shale associated with barite mineralization have similar geochemistry to non-baritic shale from the NWT study area. Barium enrichment in samples associated with low sulphate concentrations indicates that sulphate supply was limited. Relative Sr-enrichment in the carbonate-rich sample is expected as Sr is a common trace element in carbonates (e.g. Veizer et al., 1999). The composition of the other sample (MgO, CaO, Zn etc) has been modified as a result of carbonate alteration that could be associated with sulphide mineral-

ization. Both background samples have a similar REE pattern to PAAS (Fig 5.3a). The non-baritic sample associated with barite mineralization has notable negative Ce and Eu anomalies and slightly lower overall REE concentrations compared to PAAS (Fig. 5.3b). The similarity in the litho-geochemistry of non-baritic samples from the Lower Earn Group from both the Walt/Hess/Tyralla occurrences in Mac-Millan Pass and NWT barite horizons indicates that the restricted, anoxic conditions that prevailed during the late Devonian can be extended back in time to at least the middle Devonian.

The baritic Portrait Lake Formation sample is almost identical to samples from baritic sediments from the NWT with the only exception being an enrichment in Zn (330 ppm) which is associated with sulphide mineralization. The REE pattern of the baritic sample (Fig. 5.3c) is identical to other baritic samples from the NWT. The similarity in overall geochemistry of epigenetic barite from the Walt/Hess/Tyralla occurrences and syngenetic - diagenetic barite occurrences from the NWT suggests that the hydrothermal fluids that carried Ba in both these systems were also similar.

#### *6.2.2 Timing of mineral assemblages and geochemistry of Stage 1 sulphides and sulphates at Hess: Implications for fluid geochemistry and sulphur sources:*

Pyrite is the most volumetrically significant of all the early sulphides at Hess, followed by roughly equal concentrations of galena and Stage 1 sphalerite. Pyrite is also petrographically the earliest epigenetic mineral to have formed at Hess. It has  $\delta^{34}\text{S}$  values in the range +23 to +25 ‰. Diagenetic pyrite with such  $\delta^{34}\text{S}$  values is a common feature in most black shales (e.g. Arthur and Sageman, 1994; Curtis, 1980; Leach et al., 2010).

The continental crust typically has concentrations of Re and Os averaging ~ 400 and 50 ppt respectively (Esser and Turekian, 1993). However, black shales are major reservoirs of Re and Os where they are primarily sequestered in organic matter (e.g. Cohen et al., 1999; Creaser, 2003; Turgeon et al., 2007). Organic-rich sediments can concentrate Re and Os from seawater up to 400 and 4 ppb respectively in suboxic to anoxic conditions (Colodner et al., 1993). Outcrop shale samples from the Walt/Tyralla/Hess occurrences have a range of total organic carbon from 2.35 – 7.28 % while a barite-bearing outcrop sample (Sample 10NF42F) has only 1.7 % organic carbon. Texturally, there is very little organic matter in the pyrite-rich samples. Petrographically, pyrite is also replaced by carbonates associated with Pb-Zn minerals and brecciated in places. The source of the Fe in pyrite is probably the

Canol Formation shale itself.

Very few studies on the Re-Os systematics of pyrite in age-equivalent strata have been conducted. Rhenium and Os content of pyrite from late Devonian pyritic ore from the Tharsis and Rio Tinto volcanogenic massive sulphide deposits in the Iberian Pyrite Belt in Spain ranged from 0.338 to 66.27 ppb Re and 0.051 to 0.669 ppb Os respectively (Mathur et al., 1999). While the Re concentrations are comparable with data from this study, it is very clear that Os concentrations in pyrite from Hess are orders of magnitude greater than this. Morelli et al. (2004) analyzed Re and Os concentrations in pyrite from the Mississippian Red Dog shale-hosted massive sulphide deposit in Alaska which showed broadly similar Re concentrations but also had samples that contained up to 3.637 ppb Os, similar to those measured here from Hess.

The most striking feature of the Re-Os data acquired in this study are the very low  $^{187}\text{Re}/^{188}\text{Os}$  and  $^{187}\text{Os}/^{188}\text{Os}$  ratios for pyrite. Turgeon et al. (2007) found that  $^{187}\text{Re}/^{188}\text{Os}$  ratios in black shales at the Frasnian-Fammenian boundary to be on the order of 100s, and that  $^{187}\text{Os}/^{188}\text{Os}$  ratios from the same samples ranged from 1.3 to 5.4 which they used to infer the  $^{187}\text{Os}/^{188}\text{Os}$  ratio of coeval seawater to be 0.45 – 0.47 at the time of deposition. A similar study of the time-equivalent Exshaw Formation black shale in Alberta yielded an initial  $^{187}\text{Os}/^{188}\text{Os}$  ratio of  $0.42 \pm 0.01$  for Frasnian-Fammenian seawater (Selby and Creaser, 2005). The studies on pyrite in the Iberian Pyrite Belt yielded an initial  $^{187}\text{Os}/^{188}\text{Os}$  ratio of  $0.376 \pm 0.056$  which was used to infer multiple sources for radiogenic Os such as black shale, ocean water and/or surrounding felsic crust (Mathur et al., 1999).

Simple two-point isochrons were calculated for pairs of Hess pyrite were calculated using Isoplot/Ex (Ludwig, 2000) in order to estimate the initial  $^{187}\text{Os}/^{188}\text{Os}$  values that pyrite may have started with. This was done to see if they had initial values that could have been derived from seawater or otherwise. Data generated from these calculations were eliminated if pairs of pyrite gave a negative age of formation or if the calculated age was smaller than error. These two-point isochrons are plotted against Re-Os values for Hess pyrite in Figure 6.3a. Based on this data, the calculated initial  $^{187}\text{Os}/^{188}\text{Os}$  ratios for individual pyrite pairs fall largely in the range 0.58 to 0.79. There is one outlier that has a calculated initial  $^{187}\text{Os}/^{188}\text{Os}$  ratio of  $0.33 \pm 0.015$ .

The theoretical evolution of the Re-Os systematics of a middle Devonian black shale (the conodont-derived age of the Cathy sediments, ~390Ma, Chapter 2) were calculated for 5 Ma time increments and initial  $^{187}\text{Re}/^{188}\text{Os}$  ranging from

10 - 500. This was done by assuming that their initial  $^{187}\text{Os}/^{188}\text{Os}$  was  $\sim 0.45$  which is thought to be a good estimate for the composition of Devonian seawater that was coeval with these shales (Selby and Creaser, 2005; Turgeon et al., 2007). The results from these calculations are shown in figure 6.3b with data to be found in Appendix D.

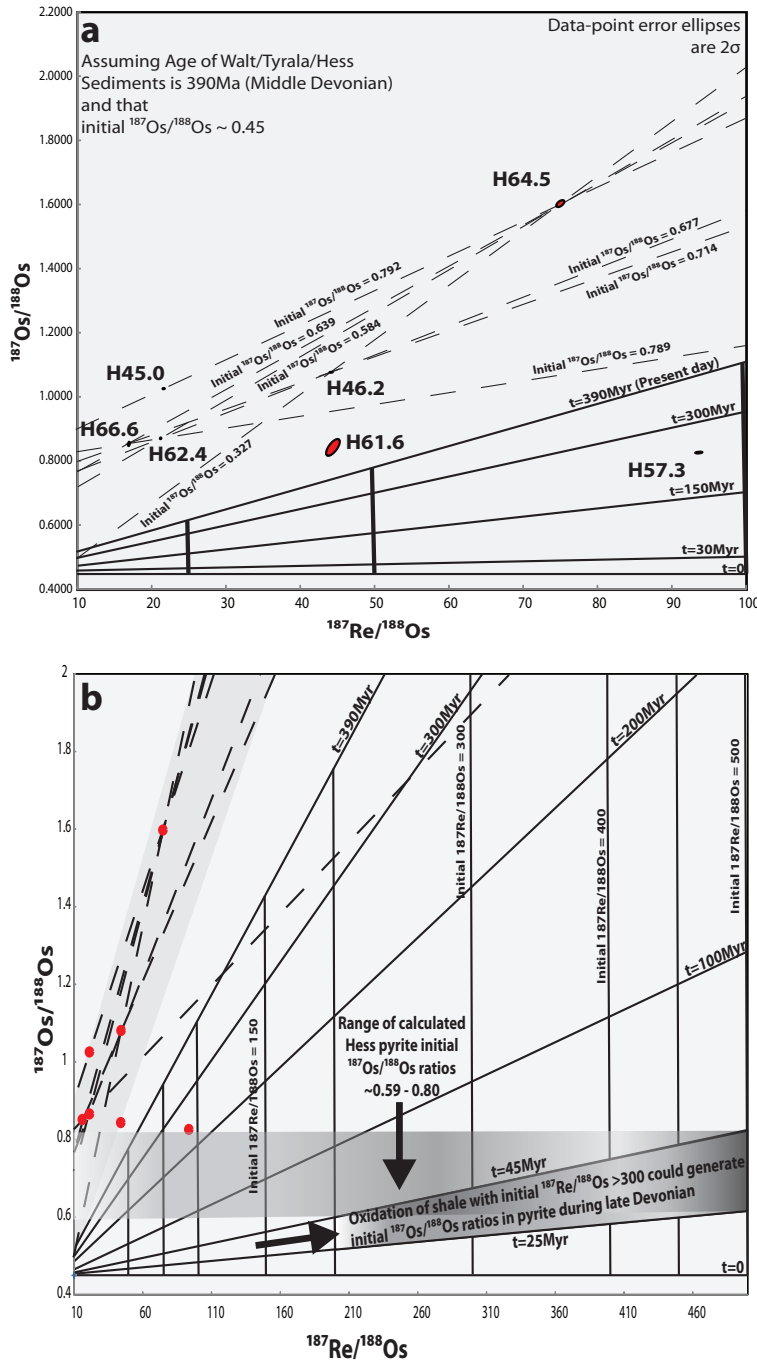


**Figure 6.3:** (a) Re-Os values for Hess pyrite plotted on a graph of  $^{187}\text{Re}/^{188}\text{Os}$  against  $^{187}\text{Os}/^{188}\text{Os}$  with 2-point isochrons calculated for individual pyrite pairs

*(b) theoretical Re-Os isotope system evolution of a black shale plotted with Hess pyrite Re-Os data showing its possible contribution to Re and Os in Hess pyrite between 15 - 45 Myr after deposition when initial  $^{187}\text{Os}/^{188}\text{Os}$  ratio = 0.45 and initial  $^{187}\text{Re}/^{188}\text{Os}$  of the shale is >300, plotted using Isoplot/Ex (Ludwig, 2000)*

The low ratios obtained in this study, while not conducive to creation of a robust isochron; indicate that there has been substantial radiogenic Os input during the formation of pyrite at Hess (and/or possible Re loss). Pyrite textures suggest they post-date lithification. By inference then the fluids that contributed Re and Os to pyrite must have pre-dated pyrite formation and could be related to an early to late diagenetic process.  $^{187}\text{Re}$  that remained in these fluids generated from shale could then undergo radioactive decay to  $^{187}\text{Os}$  over the time before Fe and S entered the system to form pyrite. This would result in an elevated calculated initial  $^{187}\text{Os}/^{188}\text{Os}$  for pyrite at Hess ratio higher than that for seawater at the time (Fig 3.2a).

The calculated initial  $^{187}\text{Os}/^{188}\text{Os}$  ratios for viable pyrite pairs fall largely in the range 0.59 – 0.80. Typical  $^{187}\text{Re}/^{188}\text{Os}$  ratios that have been analyzed in black shale from the Devonian-Mississippian transition are on the order of ~ 400 (Selby and Creaser, 2005; Turgeon et al., 2007). The calculation of the Re-Os isotopic evolution of such a shale could allow some constraints on the timing of pyrite formation at Hess, if indeed the Os in pyrite was directly sourced from the sediments the Walt/Tyralla/Hess occurrences. Two assumptions were made: 1. the age of the sedimentary rocks that host Hess is ~ 390 Ma (Middle Devonian, Irwin and Orchard, 1991), and 2. the initial  $^{187}\text{Os}/^{187}\text{Os}$  ratio of these sediments was 0.45. Using the calculated data presented in Fig 5.5, it can be seen that a shale with an initial  $^{187}\text{Re}/^{188}\text{Os}$  ratio greater than 300 could quickly evolve an  $^{187}\text{Os}/^{188}\text{Os}$  ratio of 0.59 within 30 Myr of deposition. A shale with an initial  $^{187}\text{Re}/^{188}\text{Os}$  ratio of 500 would evolve to the same  $^{187}\text{Os}/^{188}\text{Os}$  composition within 15 Myr of deposition. Similar calculations for the upper limit (0.80) of the initial pyrite  $^{187}\text{Os}/^{188}\text{Os}$  ratios would take 45 Myrs and 40 Myrs for an initial  $^{187}\text{Re}/^{188}\text{Os}$  ratio of 300 and 500 respectively. Therefore, a 15 – 45 Myr ‘window’ post-deposition of the shale in the Walt/Tyralla/Hess claims can be defined where the range of calculated initial  $^{187}\text{Os}/^{187}\text{Os}$  ratios of pyrite match those of the sediments that they were derived from. This could constrain the timing of pyrite formation at Hess to between 375 – 345 Ma which would be consistent with mineralization taking place in the late Devonian – early Mississippian.

It is likely that organic matter in the Portrait Lake Formation must have

been responsible for the high Os and low Re content of pyrite at Hess. Colodner et al. (1992) have shown that Re can be mobilized post-deposition of anoxic sediments as a result of a change to oxygenated conditions. Oxidizing fluids migrating through the stratigraphy would be necessary in order to degrade the organic matter in the host shale and solubilize Os. However, these oxidizing fluids would need to be present before pyrite formation in order to have contributed to the  $^{187}\text{Re}/^{188}\text{Os}$  and  $^{187}\text{Os}/^{188}\text{Os}$  ratios of pyrite at Hess. Slow crystallization processes may have resulted in a non-homogenous source for Os sequestered in its' crystallographic structure and could further contribute to a higher initial  $^{187}\text{Os}/^{188}\text{Os}$  ratio. Furthermore, Re could have been lost during pyrite growth as a result of preferential uptake by the reducing lithologies in the same stratigraphic horizon (Colodner et al., 1993). Based on the above petrographic and geochemical interpretation, pyrite at Hess was not sourced from seawater but directly linked to alteration of black shale in the Portrait Lake Formation as a result of other fluid interactions.

The sample set from the Hess barite drill core, while limited; can be used to outline a complex set of reactions in multiple stages that produced an assemblage of base metal sulphides, sulphosalts and barium minerals. Additional controls can be placed on the compositions of some of the fluids that precipitated these minerals based on the  $\delta^{34}\text{S}$  values of the sulphates and early sulphides in the Walt/Tyrala/Hess occurrences.

The  $\delta^{34}\text{S}$  values of barite in outcrop have two distinct populations, one within the range +19 to +25 ‰, and the second from +46 to +50 ‰. The former group could be either sourced from seawater or a hydrothermal fluid, while the latter group probably reflects the process of closed-system BSR. Primary structures and relationships that might be used to indicate a syndepositional to syndiagenetic environment have largely been destroyed. However, the bulk of the textures observed at these showings are secondary (i.e. replacing a pre-existing favourable host rock). Replacement, brecciation and nodule formation are features of diagenetic to epigenetic mineralization that could have only taken place below the SWI.

The early stage assemblage of sulphide minerals at Hess (Stage 1 sphalerite, galena and barium minerals) are also epigenetic to the host Canol Formation sediments at this occurrence. These sulphides have a very narrow range of  $\delta^{34}\text{S}$  values (+23 to + 28 ‰) which is consistent with a homogenous, reduced sulphur source. Similar  $\delta^{34}\text{S}$  values in intergrown sulphides can be used to infer equilibrium precipitation of sulphides from a reducing ( $\text{H}_2\text{S}$ -rich) fluid in which  $[\text{H}_2\text{S}]_{\text{Fluid}} \gg \gg \Sigma[\text{Metals in solution}]$  (Ohmoto et al., 1990). Such reducing fluids could not have

contained even small amounts of sulphate and by the same token could not have carried Pb or Zn in significant quantities without the precipitation of sulphides and/or barite. Therefore, the fluids responsible for Stage 1 mineralization were reducing, Ba and H<sub>2</sub>S rich and acidic. In a critical study, Cooke et al. (2000) found that such reducing, acidic, Ba-bearing hydrothermal fluids are buffered by reduced, carbonaceous lithologies. The stratigraphy underlying the Portrait Lake Formation are basinal limestone and calcareous shale belonging to the Siluro-Devonian Road River group (Cecile, 2000; Gordey et al., 1982). This package of lithologies would easily buffer and enable transport of such Ba-rich hydrothermal fluids.

In order to precipitate the early sulphides and sulphates found in mineralized Hess samples, a metal-bearing fluid must encounter an S-bearing fluid or lithology. The presence of barite and barium carbonates associated with Stage 1 galena and sphalerite suggests that the sulphate and carbonate are transported by a fluid carrying Pb, Zn, dissolved sulphate and carbonate. This metal-bearing fluid is considered an oxidizing fluid as it contained more dissolved sulphate than aqueous sulphide using the definition of Cooke et al. (2000). Fluid inclusions in ankerite from the Tom Pb-Zn-Ba deposit indicates the presence of a contemporaneous, saline fluid (14 - 18 wt. % NaCl, Ansdell et al., 1989) which could also have carried Pb and Zn.

The Re-Os and S-isotope geochemistry of pyrite at Hess indicates that this oxidizing fluid was present before any of the sulphides were precipitated. Therefore, the barite found in the Walt/Tyralla/Hess occurrences in the study area was not precipitated from seawater but was the product of mixing of a reducing fluid with a sulphate-bearing oxidizing fluid that could not have been seawater. Therefore, the bulk of the  $\delta^{34}\text{S}$  values for barite precipitated in the Yukon study area are a reflection of the composition of the oxidizing fluid.

The origin of Stage 2 sulphides and sulphosalts is less clear. Stage 2 mineralization contains Zn, Pb, Cu, Sb, Sn, As and Ag and is not at all consistent with derivation from low-temperature fluids in any of the SEDEX models whether vent-proximal (Goodfellow and Lydon, 2007) or otherwise (Cooke et al., 2000; Leach et al., 2010). In fact, the sphalerite-k esterite-geocronite assemblage has been found in intrusion related Sb-Ag mineralizing systems in the former Soviet Republics and parts of China (e.g. Corsini et al., 1991; Gamyamin et al., 2003; Osadchii, 1996). These Sb-Sn-Cu-Ag systems are thought to have formed at temperatures greater than 200 C (Borisenko et al., 2003) and are often associated with quartz and carbonates such as calcite and siderite (Gamyamin et al., 2003; Peng et al., 1999).

Mid-Cretaceous intrusion-related tin-tungsten-copper deposits are also present in MacMillan Pass (Dick and Hodgson, 1982; Gerstner et al., 1989) and intrusive bodies have been documented in the study area (Fig. 2.2). These could be the responsible for the second generation of sulphides and sulphosalts. In fact, one sample of galena had a  $\delta^{34}\text{S}$  value of  $\sim+8\text{‰}$  which could reflect a magmatic source for Stage 2 sulphides. The overall silver paucity in samples also would indicate that the temperature of the fluid that carried polymetallic elements was probably higher than 200 – 250 °C which is optimal for silver deposition in these systems (Borisenko et al., 2003; Obolensky et al., 2007).

### *6.3 Barite and its relationship with sediment-hosted Pb-Zn deposits: Implications for further exploration in the Selwyn Basin*

The model for the genesis of an ore deposit ultimately determines the exploration methods used to locate new mineral discoveries. There have been contrasting arguments for a syndepositional (e.g. Goodfellow and Lydon, 2007) versus a replacive/post-depositional origin (Kelley et al., 2003; Leach et al., 2010) for SEDEX deposits with the latter researchers preferring the term shale-hosted massive sulphide (SHMS) deposits.

The core tenet of the vent-proximal SEDEX model in the Selwyn is that Ba-Pb-Zn-bearing hydrothermal fluids were transported along syndepositional faults to the seafloor where upon interacting with a stratified water column, hydrothermal fluid mixing with anoxic, reduced seawater resulted in the precipitation of base-metal sulphides and sulphates in a zoned pattern around a vent (Goodfellow and Lydon, 2007).

The data from the NWT outline here suggest the vent-proximal SEDEX model needs to be revised. First, these baritic strata form a marker horizon in the upper most parts of the lower Earn Group near the end of the Devonian indicating a large barite mineralizing event. Second, the barite horizons have both syndepositional and diagenetic textures that together with sulphur isotope values suggest that there was barite mineralization taking place above and below the SWI with a limited supply of sulphate (Fig 6.4a, 6.4b). The lithochemistry and the degree of  $^{34}\text{S}$ -isotope fractionation in barite from the lower Earn Group sediments suggest they were deposited in oxygen-depleted conditions. Most importantly there are no observed zinc or lead minerals associated with any of the NWT barite occurrences even at the Cowan structure which transported some of the Ba-bearing fluids to the SWI. This would imply either that the high temperature, reducing acidic fluids that

carried barium had no significant quantities of Pb or Zn, or that any base-metals they carried were precipitated before this fluid reached the SWI.

In the Yukon study area, the Walt/Tyralla/Hess barite occurrences are hosted in middle Devonian lower Earn Group rocks. The textures in this area are epigenetic and indicate remobilization of barite resulting in a pseudo-laminated appearance for some samples. Despite this, the range of S-isotopic composition of barite in outcrop in the Yukon has the same range of  $\delta^{34}\text{S}$  values as in the NWT study area. Textural and geochemical evidence therefore suggests that sulphate in barite was not derived from seawater. Least altered lower Earn Group sediments in the Yukon study area are geochemically similar to those in the NWT.

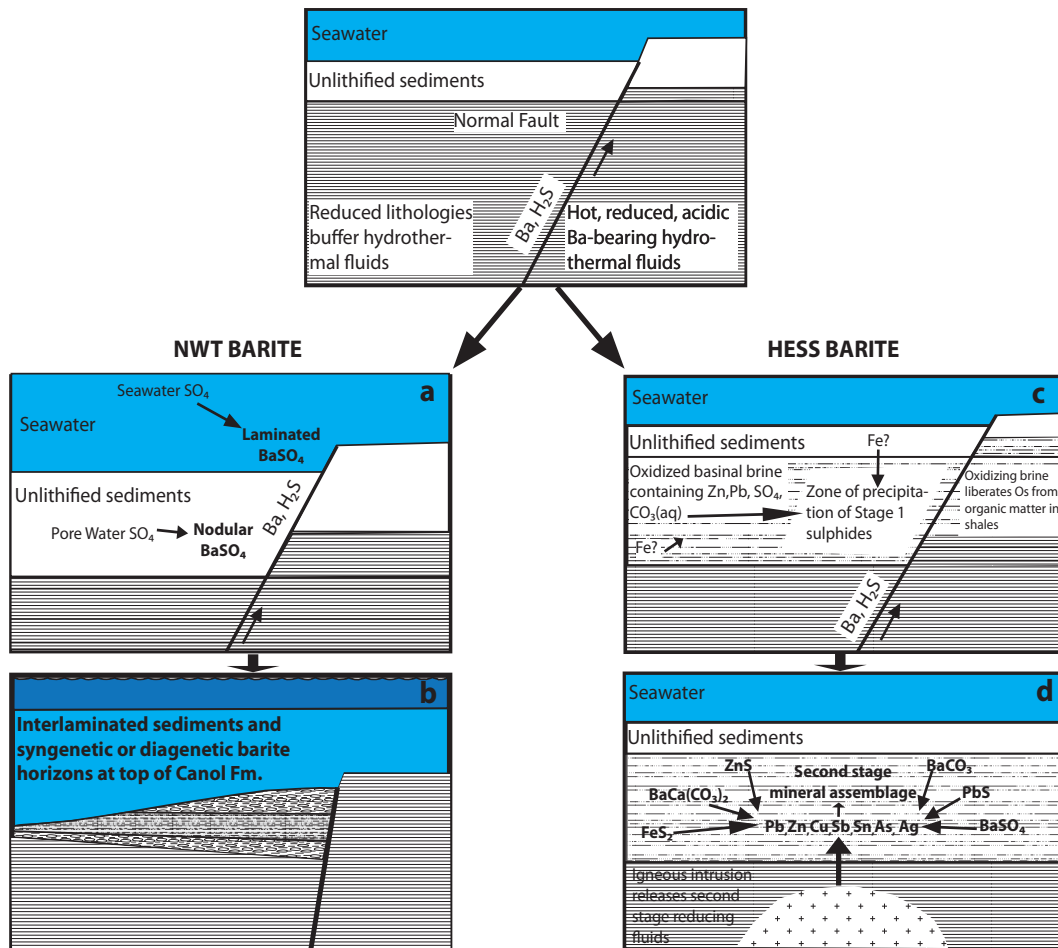


**Figure 6.4:** Schematic diagram of mineralizing events and mineral assemblages generated as a result of fluid-fluid interactions.

The drill-core from Hess contains epigenetic sulphides, barite, witherite and other carbonates which have no textures associated with syngenetic mineral-

ization hosted by altered lower Earn Group shale. Pyrite was the earliest epigenetic mineral to form and its Re-Os isotope systematics indicate that it formed as the result of alteration of lower Earn Group shale due to oxidative breakdown of organic matter in host sedimentary rocks before pyrite was crystallized. The timing of pyrite mineralization can be constrained to between 375 – 345 Ma based on its derivation from middle Devonian lower Earn Group sediments. Pyrite and Stage 1 sulphides (galena and coarse-grained, zoned, Fe-rich sphalerite) have a very narrow, enriched range of  $\delta^{34}\text{S}$  values that indicates equilibrium precipitation from a homogenous, reduced sulphur source. Intimately linked with Stage 1 sulphide mineralization is hydrothermal barite and witherite. The Stage 1 mineral assemblage is the result of the interaction of an oxidized Pb, Zn,  $\text{SO}_4^{2-}$  and  $\text{CO}_{3(\text{aq})}$ -bearing fluid and a reduced, Ba and  $\text{H}_2\text{S}$ -bearing fluid (Fig 6.4c). This reduced fluid was probably the same fluid that formed the barite sequences in the NWT study area, or may have derived from BSR of the NWT barite sequences in the uppermost parts of the lower Earn Group. The Stage 1 mineral assemblage is then overprinted by an intrusion-related, reducing mineral assemblage consisting of high-temperature sulphides, sulphosalts, quartz and carbonate (6.4d).

The components of the oxidizing fluid are analogous to those contained in modern day deep-sea brines (Kharaka and Hanor, 2004). Such oxidizing brines have been experimentally modeled to carry significant quantities of Pb, Zn and  $\text{SO}_4^{2-}$  (Cooke et al., 2000; Hanor, 1994) and are intrinsically barium-poor. Interaction of such oxidizing brines with high temperature, acidic, reducing hydrothermal fluids would precipitate the Stage 1 sulphide, sulphate and carbonate assemblage observed with Hess. In order to further constrain the geochemical properties of the oxidizing fluids, observed mineral assemblages can be plotted on mineral stability diagrams. Cooke et al. (2000) plotted such relationships for Proterozoic Australian SEDEX deposits and Selwyn-type SEDEX deposits based on temperature and salinity of fluids. Since the temperatures and salinities of fluids that formed shale-hosted lead-zinc deposits are still a subject of discussion (Ansdell et al., 1989; Cooke et al., 2000; Gardner and Hutcheon, 1985), the end-member fluid compositions of 150°C and 25 eq. wt % NaCl (Fig. 6.5a), and 250°C and 10 eq. wt % NaCl (Fig 6.5b) are plotted separately.

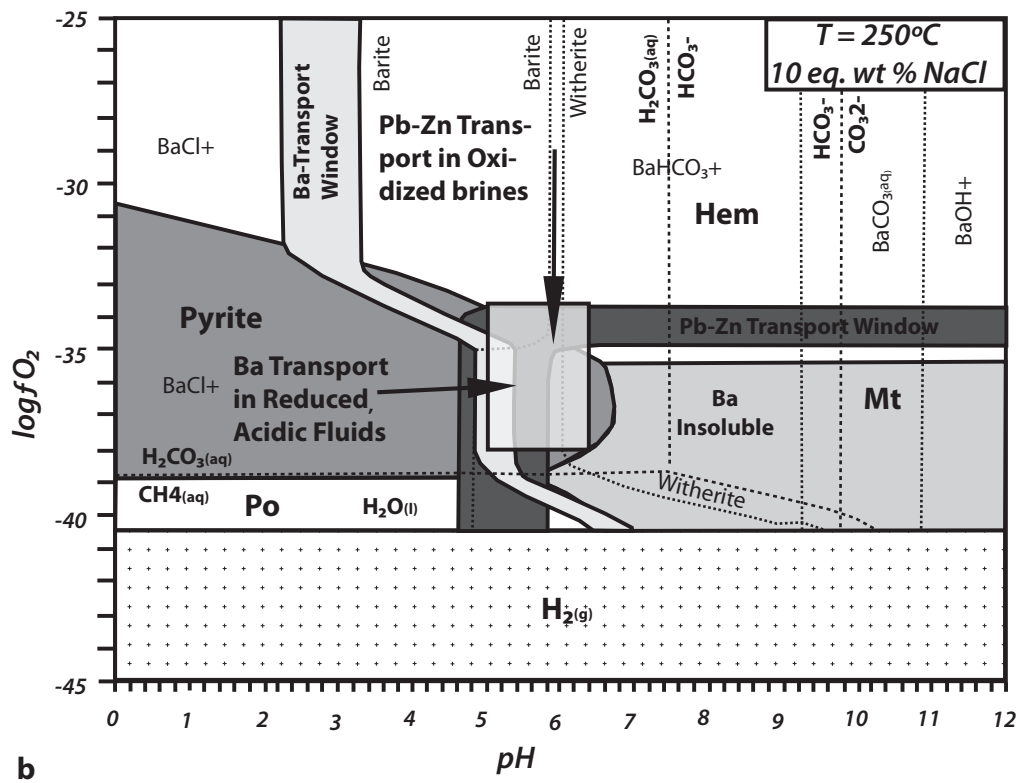
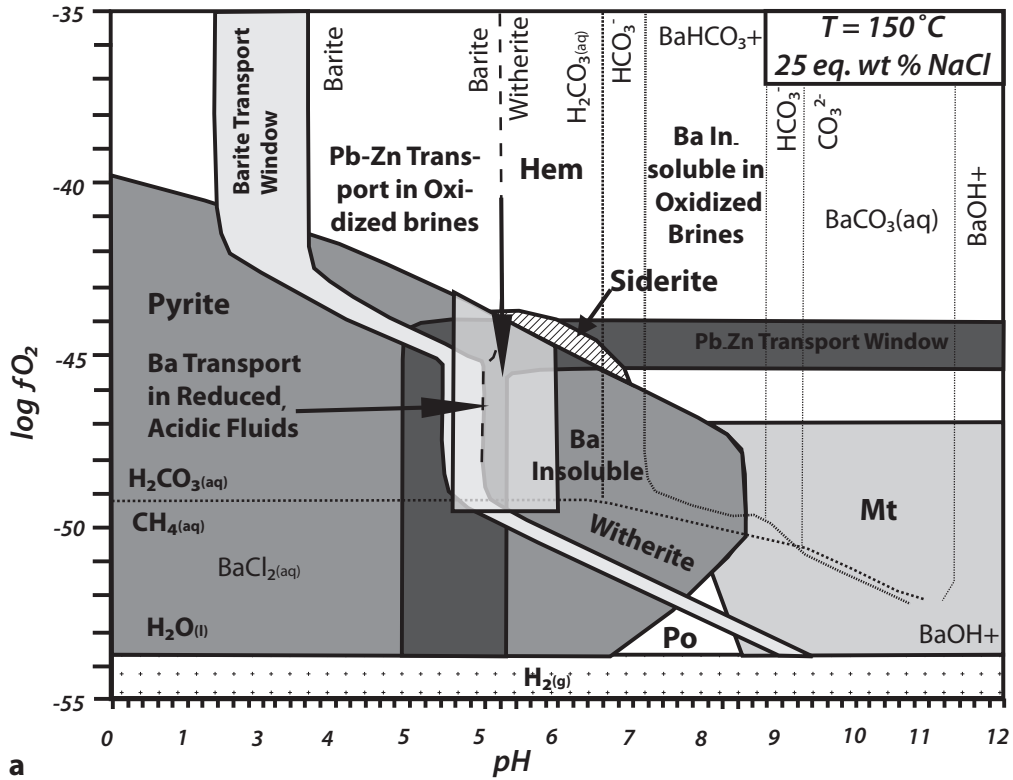


Figure 6.5: Log  $f_{\text{O}_2}$ -pH diagrams showing stability fields for Fe oxides and sulfides, siderite, solubility contours, and the metal transport window for galena and

*sphalerite, and for barite and witherite, together with the predominance fields for the principal aqueous carbon- and barium-bearing species, and the stability fields for water and  $H_2(g)$  ( $P_{H_2} = 1$  bar). Arrows indicate transport of Ba in reduced, acidic fluids and Pb-Zn transport in oxidized brines. Shaded box shows the mineral assemblages from Hess which resulted from reaction of Ba-bearing fluids with Pb-Zn-bearing brines (a) 150°C,  $m(Na^+) = 4.76$ ;  $m(K^+) = 0.46$ ;  $m(Ca^{2+}) = 0.31$ ;  $m(Cl^-) = 5.83$  ( $\approx 25$  wt % NaCl equiv). (b) 250°C,  $m(Na^+) = 1.58$ ;  $m(K^+) = 0.15$ ;  $m(Ca^{2+}) = 0.10$ ;  $m(Cl^-) = 1.94$  ( $\approx 10$  wt % NaCl equiv). Diagrams calculated for  $\Sigma S = 0.001$  m and  $\Sigma C = 0.256$  m. Abbreviations: *mt* = magnetite, *po* = pyrrhotite, *hem* = hematite (modified from Cooke et al., 2000)*

The co-existence of barite and witherite is the key factor in estimating the composition of the oxidizing brine that carried Pb and Zn. By tracking the barite-witherite stability line and using the mineral assemblage produced at Hess, it can be seen that they can only be the result of interaction between a reduced, Ba-bearing hydrothermal fluid with lead-zinc bearing oxidized fluid. The lack of siderite and presence of pyrite in Hess drill core could be the result of higher temperatures than those that formed Australian SEDEX deposits ( $> 150^\circ\text{C}$ , Fig 3.7a). Using the same mineralogical relationships to interpret the composition fluids that formed Selwyn-type SEDEX deposits (i.e.  $\sim 250^\circ\text{C}$  and 10 eq. wt % NaCl), it could be postulated that the Selwyn Pb-Zn bearing brines were mildly acidic (pH  $\sim 6$ ) and oxidized compared to hot, highly acidic (pH 2 – 4), reducing Ba-bearing hydrothermal fluids (Fig. 3.7b). Even under lower temperatures, the oxidizing brines could not have been less than a pH of 5 which is too low to carry significant quantities of Ba (Hanor, 2000).

The timing of syngenetic-diagenetic barite mineralization in the upper part of the lower Earn Group in the NWT appears to be contemporaneous with epigenetic barite/barium carbonate mineralization at the Walt/Tyrala/Hess occurrences in the Yukon study area based upon the Re-Os isotope modelling presented in this study. Barium is concentrated in K-bearing minerals such as K-feldspars and K-micas (Hanor, 2000). These minerals are found mostly in major igneous and siliciclastic rock types, the latter of which make up a large part of the stratigraphy underlying the lower Earn Group in the Selwyn basin. Dissolution of feldspathic sandstones has been shown to provide a source of Ba in basinal sediments based on Pb-isotopic evidence from Schrijver et al. (1994). By a similar process hot, acidic hydrothermal fluids could have leached Ba from the sedimentary package and base-

ment underneath the lower Earn Group.

The major result of this study is the definition of two types of fluids in the Selwyn Basin during the middle Devonian to Early Mississippian. The first is a hot, highly acidic, reducing ( $\text{H}_2\text{S}$ -rich), Ba-bearing hydrothermal fluid which without interaction with another fluid, was transported along structures that reached the SWI between the Late Devonian and Early Mississippian. Low REE totals and LREE enrichment in barite reflect a hydrothermal source for barium (Guichard et al., 1979; Hein et al., 2007). As mentioned previously, this fluid was probably buffered by the stratigraphy in the lower Earn Group and underlying Road River Group. Upon reaching the SWI, this fluid precipitated barite in both seawater (laminated barite) and in unlithified sediments (nodular barite). The second fluid is an oxidized, mildly acidic brine that contains Pb, Zn, dissolved  $\text{SO}_4^{2-}$  and  $\text{CO}_3^{2-}$  which interacted with middle Devonian lower Earn Group sediments between 375 and 345 Ma.

While interaction of these two fluids, such as at Hess; can produce a Pb-Zn-Ba occurrence, this is clearly not a reaction that occurred at the SWI and therefore application of the traditional vent-proximal SEDEX model for sediment-hosted lead-zinc deposits in the Selwyn Basin (e.g. Goodfellow, 1987; Goodfellow and Lydon, 2007) is not appropriate. The reduced sulphur source at Hess is not directly linked to an anoxic ocean, although oxygen-depleted conditions certainly prevailed. Most importantly, Pb and Zn were not transported by the Ba-bearing hydrothermal fluid at Hess which is a major difference from the Ba-Pb-Zn-bearing fluids prescribed by Goodfellow and Lydon (2007). Barite horizons at the top of the Canol Formation represent simple transport of the same Ba-bearing fluids to the SWI followed by barite precipitation from seawater or porewater sulphate. Sulphide,  $\text{BaSO}_4$  and Ba-carbonate mineralization in the Walt/Tyralla/Hess occurrences in the MacMillan Pass District of the Selwyn Basin are the result of a redox reaction of fluids well-below the SWI in lithified sedimentary rocks of the Canol Formation. Late Devonian sediment-hosted synsedimentary-diagenetic barite sequences in the Selwyn Basin are therefore a good indicator of the presence of hydrothermal fluids capable of causing sulphide precipitation from Pb-Zn bearing, oxidizing fluids. However barite coexisting with barium carbonate, which is epigenetic to lower Earn Group sedimentary rocks and not sourced from seawater is a better vector towards sediment-hosted Pb-Zn deposits in the Selwyn Basin.

## CHAPTER SEVEN: CONCLUSIONS AND DIRECTIONS FOR FUTURE RESEARCH

### 7.1 Conclusions

- Sediment-hosted barite sequences occur at the top of the Late Devonian – Early Mississippian Canol Formation in the Selwyn Basin, NWT and are a marker horizon in the Mackenzie and Selwyn Mountains.
- Sediment-hosted barite horizons in the NWT consist of both laminated and nodular barite which indicates an environment of formation at or near the SWI.
- Laminated and nodular barite in the NWT has a range of sulphur isotope values that are consistent with derivation from seawater in the case of laminated barite and from BSR in the case of nodular barite.
- The litho-geochemistry of Canol Formation sediments associated with barite mineralization, and the elevated  $\delta^{34}\text{S}$  values in laminated and nodular barite indicates a closed-system with respect to sulphate.
- The REE geochemistry of Canol Formation sedimentary rocks hosting or spatially associated with barite horizons indicates a dysoxic-anoxic environment in the Selwyn Basin during deposition of barite horizons. This is manifested by highly negative Eu-anomalies.
- The REE geochemistry of barite-bearing sedimentary rocks has negative Ce-anomalies which were the result of precipitation from seawater.
- Positive Eu-anomalies may indicate a hydrothermal source for barite.
- Barite, base-metal sulphides and barium carbonates in the Walt/Tyrala/Hess occurrences in the MacMillan Pass District, Yukon are hosted in middle Devonian Canol Formation shale and are epigenetic to sedimentary rocks in this area. This indicates that these minerals did not form near the SWI.
- The  $\delta^{34}\text{S}$  values of barite in the Walt/Tyrala/Hess occurrences show a similar range of values to those obtained for barite horizons in the NWT study area. However, they were not derived from seawater sulphate.
- $\delta^{34}\text{S}$  values of Stage 1 sulphides in Hess drill core which are co-eval with barite and witherite mineralization are narrow in range and indicate derivation from a homogenous sedimentary source, possibly from sulphide produced by BSR.
- Barium feldspars such as hyalophane and cymrite are products of late, burial-related diagenesis of barite and host sedimentary rocks.
- The pyrite in Hess drill core is diagenetic in origin and is not directly linked to Pb-Zn-Ba mineralization.

- The Re-Os systematics of pyrite from Hess drill core indicates extreme enrichment in Os. This indicates the presence of an oxidizing fluid solubilizing Os sequestered in organic matter in the Canol Formation which provides a heterogeneous radiogenic osmium source that was present before pyrite formation.
- Models of initial  $^{187}\text{Os}/^{188}\text{Os}$  values for Hess pyrite indicate that it was formed by oxidation of middle Devonian Canol Formation shale roughly ~15 to 45 Myr after deposition at 390 Ma.
- Stage 1 lead-zinc minerals are coeval with barite and witherite mineralization.
- The galena-sphalerite-barite-witherite assemblage indicates the reaction of a hot, reduced, acidic Ba and  $\text{H}_2\text{S}$ -bearing hydrothermal fluid the same as that which produced the barren barite, with a  $\text{Pb-Zn-SO}_4^{2-}\text{-CO}_{3(\text{aq})}$ -bearing, oxidized brine similar to those modeled for Australian SEDEX deposits. These mineral assemblages are not predicted by the traditional vent-proximal SEDEX model.
- An intrusion-related, reduced assemblage of galena, Stage 2 sphalerite, k esterite, geocronite, franckeite and associated gangue minerals overprint the early sulphide mineralization in Hess drill core.
- Epigenetic barite and witherite are products of a Pb-Zn sulphide-forming event in the MacMillan Pass District, Yukon. Barite horizons in the NWT are the result of interaction of the same hot, reduced, acidic Ba-bearing fluids with the seawater column.

## 7.2 Directions for future research

- More field work is necessary in the NWT study area in order to find structures such as at the Cowan occurrence which has the barite-witherite assemblage which is the most likely candidate for a SEDEX vent.
- Re-Os isotope analysis of organic matter in sediments hosting or associated with barite mineralization is necessary in order to constrain the age of ‘barren’ barite sequences in the NWT and barite associated with base-metal sulphides in the MacMillan Pass district, Yukon.
- Ion-microprobe studies are necessary to determine the  $\delta^{34}\text{S}$  values of barite in order to determine if individual barite laminations and nodular barite are homogenous within the same sample. Since pyrite in these samples is also very small, in-situ analysis of the  $^{34}\text{S}$  composition in pyrite would determine if it was indeed a product of BSR.
- The diagenetic feldspars and hydrous silicates in this study document the mobility of a number of elements (Ba, K, Al, Si) during burial of these baritic hori-

zons which was probably enhanced by acid produced by BSR. Other important ore-forming elements such as lead and zinc could also have been solubilized during this process. Therefore, a geochemical study of the entire package of Canol Formation is necessary to see if any significant quantity of base-metals could have been generated which could have been progenitors for other ore deposits.

- Barium carbonate has been recognized at a number of the sediment-hosted Ba-Pb-Zn deposits worldwide, especially in the MacMillan Pass District. The Tom and Jason deposits are hosted in age-equivalent strata to those hosting the Hess occurrence. Therefore, revisiting these sites is necessary to see if they were formed in similar fashion to the Hess occurrence.
- Re-Os systematics of pyrite and the mineral assemblages in Hess indicate the presence of an oxidizing, Pb-Zn-bearing brine that has not been documented in the Selwyn Basin. Detailed examination of all the Selwyn Basin strata is necessary in order to determine the origin of this brine and its possible migration paths through the sedimentary package.
- The overprinting Stage 2 mineralization in Hess drill core could provide a new target for intrusion-related mineralization in the Yukon study area. Further exploration in the Yukon study area is warranted in order to determine its source.

## CHAPTER 8: REFERENCES

Abbott, J.G., 1982, Structure and stratigraphy of the MacMillan Fold Belt: evidence for Devonian faulting: Department of Indian Affairs and Northern Development, Whitehorse, Open File, 16 p.

Abbott, J.G., and Turner, R.J.W., 1990, Character and paleotectonic setting of Devonian stratiform sediment-hosted Zn, Pb, Ba deposits, Macmillan fold belt, Yukon In: Mineral deposits of the northern Canadian Cordillera, Yukon, northeastern British Columbia (field trip 14), in Abbott, J.G., and Turner, R.J.W., eds., Geological Survey of Canada Open-file 2169, p. 99-136.

Abbott, J.G., Gordey, S.P., and Tempelman-Kluit, D.J., 1987, Setting of stratiform, sediment-hosted lead-zinc deposits in Yukon and northeastern British Columbia, in Morin, J.A., ed., Mineral Deposits of Northern Cordillera Symposium, Canadian Institute of Mining and Metallurgy, Special Volume 37, p. 1-18.

Aitken, J.D., Cook, D.G., and Yorath, C.J., 1982, Upper Ramparts River (106g) and Sans Sault Rapids (106H) map areas, District of Mackenzie, Geological Survey of Canada, Memoir 388, 48p.

AlAasm, I.S., Morad, S., Durocher, S., and Muir, I., 1996, Sedimentology, C-S-Fe relationships and stable isotopic compositions in Devonian black mudrocks, Mackenzie Mountains, Northwest Territories, Canada: Sedimentary Geology, v. 106, p. 279-298.

Ansdell, K.E., Nesbitt, B.E., and Longstaffe, F.J., 1989, A Fluid Inclusion and Stable Isotope Study of the Tom Ba-Pb-Zn Deposit, Yukon Territory, Canada: Economic Geology, v. 84, p. 841-856.

Arthur, M.A., and Sageman, B.B., 1994, Marine black shales - Depositional mechanisms and environments of ancient-deposits: Annual Review of Earth and Planetary Sciences, v. 22, p. 499-551.

Bau, M., 1991, Rare-Earth Element Mobility during Hydrothermal and Metamorphic Fluid Rock Interaction and the Significance of the Oxidation-State of Europium: Chemical Geology, v. 93, p. 219-230.

Bhatia, M.R., 1985, Rare-Earth Element Geochemistry of Australian Paleozoic Graywackes and Mudrocks - Provenance and Tectonic Control: Sedimentary Geology, v. 45, p. 97-113.

Birck, J.L., RoyBarman, M., and Capmas, F., 1997, Re-Os isotopic measurements at the femtomole level in natural samples: Geostandards Newsletter-the Journal of Geostandards and Geoanalysis, v. 21, p. 19-27.

Bjorlykke, K.O., and Griffin, W.L., 1973, Barium feldspars in ordovician sediments, Oslo-region, Norway: *Journal of Sedimentary Petrology*, v. 43, p. 461-465.

Blakey, R.C., 2003, Carboniferous-Permian Paleogeography of the Assembly of Pangaea, Volume of Proceedings 15th International Carboniferous-Permian Congress: Utrecht, The Netherlands.

Borisenko, A.S., Borovikov, A.A., Pavlova, G.G., and Gushchina, L.V., 2003, Sn-Ag ore-forming systems, 251-254 p.

Carne, R.C., and Cathro, R.J., 1982, Sedimentary Exhalative (Sedex) Zinc-Lead-Silver Deposits, Northern Canadian Cordillera: *Cim Bulletin*, v. 75, p. 66-78.

Cecile, M.P., 1982, The Lower Palaeozoic Misty Creek Embayment, Selwyn Basin, Yukon and Northwest Territories: *Geological Survey of Canada, Bulletin* 335, 78 p.

Cecile, M.P., 2000, Geology of the northeastern Niddery Lake map area, East-central Yukon and adjacent Northwest Territories, *Geological Survey of Canada, Bulletin* 553, 120 p.

Cecile, M.P., Shakur, M.A., and Krouse, H.R., 1983, The isotopic composition of western Canadian barites and the possible derivation of oceanic sulfate delta-S-34 and delta-O-18 curves: *Canadian Journal of Earth Sciences*, v. 20, p. 1528-1535.

Claypool, G.E., Holser, W.T., Kaplan, I.R., Sakai, H., and Zak, I., 1980, The age curves of sulfur and oxygen isotopes in marine sulfate and their mutual interpretation: *Chemical Geology*, v. 28, p. 199-260.

Cohen, A.S., and Waters, F.G., 1996, Separation of osmium from geological materials by solvent extraction for analysis by thermal ionisation mass spectrometry: *Analytica Chimica Acta*, v. 332, p. 269-275.

Cohen, A.S., Coe, A.L., Bartlett, J.M., and Hawkesworth, C.J., 1999, Precise Re-Os ages of organic-rich mudrocks and the Os isotope composition of Jurassic seawater: *Earth and Planetary Science Letters*, v. 167, p. 159-173.

Colodner, D., Sachs, J., Ravizza, G., Turekian, K., Edmond, J., and Boyle, E., 1993, The geochemical cycle of rhenium - a reconnaissance: *Earth and Planetary Science Letters*, v. 117, p. 205-221.

Colodner, D.C., Boyle, E.A., Edmond, J.M., and Thomson, J., 1992, Post-depositional mobility of platinum, iridium and rhenium in marine-sediments: *Nature*, v. 358, p. 402-404.

Cooke, D.R., Bull, S.W., Large, R.R., and McGoldrick, P.J., 2000, The importance of oxidized brines for the formation of Australian proterozoic stratiform sediment-hosted Pb-Zn (sedex) deposits: *Economic Geology and the Bulletin of the*

Society of Economic Geologists, v. 95, p. 1-17.

Corsini, F., Morelli, F., and Tanelli, G., 1991, A polymetallic sulfide (Cu-Pb-Zn) assemblage from the Boccheggiano-Campiano (Tuscany) pyrite deposit - Application of the stannite-sphalerite geothermometer: *Neues Jahrbuch Fur Mineralogie-Monatshefte*, p. 523-528.

Creaser, R.A., 2003, A review of the Rhenium-Osmium (Re-Os) isotope system with application to organic-rich sedimentary rocks, in Lentz, D.R., ed., *Geochemistry of Sediments and Sedimentary Rocks: Evolutionary Considerations to Mineral Deposit-Forming Environments*, Geological Association of Canada, *Geotext* 4, p. 79-83.

Creaser, R.A., Papanastassiou, D.A., and Wasserburg, G.J., 1991, Negative Thermal Ion Mass-Spectrometry of Osmium, Rhenium, and Iridium: *Geochimica Et Cosmochimica Acta*, v. 55, p. 397-401.

Crusius, J., Calvert, S., Pedersen, T., and Sage, D., 1996, Rhenium and molybdenum enrichments in sediments as indicators of oxic, suboxic and sulfidic conditions of deposition: *Earth and Planetary Science Letters*, v. 145, p. 65-78.

Curtis, C.D., 1980, Diagenetic Alteration in Black Shales: *Journal of the Geological Society*, v. 137, p. 189-194.

Deer, W.A., Howie, R.A., and Zussman, J., 2001, Barium feldspars, "Rock-forming minerals: feldspars", Volume 4A, 2nd edition: London, The Geological Society, p. 909-942.

Dewing, K., Sharp, R.J., Ootes, L., Turner, E.C., and Gleeson, S.A., 2006, Geological assessment of known Zn-Pb showings, Mackenzie Mountains, Northwest Territories: Geological Survey of Canada, Current Research 2006-A4, 12 p.

Dick, L.A., and Hodgson, C.J., 1982, The Mactung W-Cu(Zn) contact metasomatic and related deposits of the northeastern Canadian cordillera: *Economic Geology*, v. 77, p. 845-867.

Eisbacher, G.H., 1981, Sedimentary Tectonic and Glacial Record in the Windermere Supergroup, Mackenzie Mountains, northwestern Canada: Geological Survey of Canada, Paper 80-27, 40 p.

Essene, E.J., Claffin, C.L., Giorgetti, G., Mata, P.M., Peacor, D.R., Arkai, P., and Rathmell, M.A., 2005, Two-, three- and four-feldspar assemblages with hyalophane and celsian: implications for phase equilibria in BaAl<sub>2</sub>Si<sub>2</sub>O<sub>8</sub>-CaAl<sub>2</sub>Si<sub>2</sub>O<sub>8</sub>-NaAlSi<sub>3</sub>O<sub>8</sub>-KAIS(3)O(8): *European Journal of Mineralogy*, v. 17, p. 515-535.

Esser, B.K., and Turekian, K.K., 1993, The osmium isotopic composition of the continental-crust: *Geochimica Et Cosmochimica Acta*, v. 57, p. 3093-3104.

Fernandes, N.A., Gleeson, S.A., Sharp, R.J., Martel, E., and Fischer, B., 2010, Connecting SEDEX and carbonate-hosted base metal mineralization in the Northwest Territories: Barite as a possible vector: Northwest Territories Geoscience Office, NWT Open Report 2010-003, 26p.

Finlowbates, T., 1987, The Possible Significance of Uncommon Barium-Rich Mineral Assemblages in Sediment-Hosted Lead-Zinc Deposits: *Geologie En Mijnbouw*, v. 66, p. 65-66.

Frei, R., Nagler, T.F., Schonberg, R., and Kramers, J.D., 1998, Re-Os, Sm-Nd, U-Pb, and stepwise lead leaching isotope systematics in shear-zone hosted gold mineralization: Genetic tracing and age constraints of crustal hydrothermal activity: *Geochimica Et Cosmochimica Acta*, v. 62, p. 1925-1936.

Gamyagin, G.N., Anikina, E.Y., Bortnikov, N.S., and Alpatov, V.V., 2003, The prognostic silver-polymetallic deposit, Sakha (Yakutia): chemistry and zoning of ore veins: *Geology of Ore Deposits*, v. 45, p. 466-480.

Gardner, H.D., and Hutcheon, I., 1985, *Geochemistry, Mineralogy, and Geology of the Jason Pb-Zn Deposits, Macmillan Pass, Yukon, Canada: Economic Geology*, v. 80, p. 1257-1276.

Gerstner, M.R., Bowman, J.R., and Pasteris, J.D., 1989, Skarn formation at the MacMillan Pass tungsten deposit (Mactung), Yukon and Northwest Territories. 1. P-T-X-V characterization of the methane-bearing, skarn-forming fluids: *Canadian Mineralogist*, v. 27, p. 545-563.

Giesemann, A., Jager, H.J., Norman, A.L., Krouse, H.P., and Brand, W.A., 1994, Online sulfur-isotope determination using an elemental analyzer coupled to a mass spectrometer: *Analytical Chemistry*, v. 66, p. 2816-2819.

Goldhaber, M.B., 2004, Sulfur-rich sediments, in Mackenzie, F.T., ed., *Sediments, Diagenesis and Sedimentary Rocks, Volume 7: Treatise on Geochemistry*: Oxford, Elsevier-Pergamon, p. 257-288.

Goodfellow, W.D., 1987, Anoxic Stratified Oceans as a Source of Sulfur in Sediment-Hosted Stratiform Zn-Pb Deposits (Selwyn Basin, Yukon, Canada): *Chemical Geology*, v. 65, p. 359-382.

Goodfellow, W.D., and Jonasson, I.R., 1984, Ocean Stagnation and Ventilation Defined by Delta-S-34 Secular Trends in Pyrite and Barite, Selwyn Basin, Yukon: *Geology*, v. 12, p. 583-586.

Goodfellow, W.D., and Lydon, J.W., 2007, Sedimentary-exhalative (SEDEX) deposits, in Goodfellow, W.D., ed., *Mineral Deposits of Canada: A Synthesis of Major Deposit-types, District Metallogeny, the Evolution of Geological Provinces*,

and Exploration Methods, Geological Association of Canada Special Publication no .5, p. 163-183.

Goodfellow, W.D., Lydon, J.W., and Turner, R.J.W., 1993, Geology and genesis of stratiform sediment-hosted (SEDEX) zinc-lead-silver sulphide deposits., in Kirkham, R.V., Sinclair, W.D., Thorpe, R.I., and Duke, J.M., eds., Mineral deposit modeling: Geological Association of Canada, Special Paper no. 40, p. 201-251.

Gordey, S.P., Abbott, J.G., and Orchard, M.J., 1982, Devonian-Mississippian Earn Group and younger in strata in east-central Yukon: Current Research, Part B; Geological Survey of Canada, Paper 82-1B, p. 93-100.

Gordey, S.P., and Anderson, R.G., 1993, Evolution of the northern Cordilleran Miogeocline, Nahanni map area (105I), Yukon and Northwest Territories, Geological Survey of Canada, Memoir 428, 214 p.

Grassineau, N.V., Mathey, D.P., and Lowry, D., 2001, Sulfur isotope analysis of sulfide and sulfate minerals by continuous flow-isotope ratio mass spectrometry: Analytical Chemistry, v. 73, p. 220-225.

Gromet, L.P., Dymek, R.F., Haskin, L.A., and Korotev, R.L., 1984, The North-American Shale Composite - Its Compilation, Major and Trace-Element Characteristics: Geochimica Et Cosmochimica Acta, v. 48, p. 2469-2482.

Guichard, F., Church, T.M., Treuil, M., and Jaffrezic, H., 1979, Rare-earths in barites - Distribution and effects on aqueous partitioning: Geochimica Et Cosmochimica Acta, v. 43, p. 983-997.

Hanor, J.S., 1994, Physical and chemical controls on the composition of waters in sedimentary basins: Marine and Petroleum Geology, v. 11, p. 31-45.

Hanor, J.S., 2000, Barite-celestine geochemistry and environments of formation, Sulfate Minerals - Crystallography, Geochemistry and Environmental Significance, Volume 40: Reviews in Mineralogy & Geochemistry: Washington, Mineralogical Soc America, p. 193-275.

Hein, J.R., Zierenberg, R.A., Maynard, J.B., and Hannington, M.D., 2007, Barite-forming environments along a rifted continental margin, Southern California Borderland: Deep-Sea Research Part Ii-Topical Studies in Oceanography, v. 54, p. 1327-1349.

Irwin, S.E.B., and Orchard, M.J., 1991, Upper Devonian-Lower Carboniferous conodont biostratigraphy of the Earn Group and overlying units, northern Canadian Cordillera, in Orchard, M.J., and McCracken, A.D., eds., Ordovician to Triassic Conodont Paleontology of the Canadian Cordillera, Geological Survey of Canada, Bulletin 417, p. 185-213.

Jakobsen, U.H., 1990, A hydrated barium silicate in unmetamorphosed sedimentary-rocks of central north Greenland: *Mineralogical Magazine*, v. 54, p. 81-89.

Kelley, K.D., Leach, D.L., Johnson, C.A., Slack, J.F., Dumoulin, J.A., and King, A.R., 2003, The giant Red Dog Zn-Pb-Ag massive sulfide deposits, northwestern Alaska, USA: Basin setting and conditions of ore formation: *Mineral Exploration and Sustainable Development*, Vols 1 and 2, p. 689-692.

Kharaka, Y.K., and Hanor, J.S., 2004, Deep Fluids in the Continents: I. Sedimentary Basins, in Drever, J.I., ed., *Surface and Ground Water, Weathering, and Soils: Treatise on Geochemistry*: Oxford, Elsevier-Pergamon, p. 2-40.

Konhauser, K., 2007, *Introduction to Geomicrobiology*: Malden, Ma., U.S.A., Blackwell, 425 p.

Kornexl, B.E., Gehre, M., Hofling, R., and Werner, R.A., 1999, On-line delta O-18 measurement of organic and inorganic substances: *Rapid Communications in Mass Spectrometry*, v. 13, p. 1685-1693.

Large, D.E., 1980, On the geology, geochemistry and genesis of the Tom Pb-Zn-Barite deposit, Yukon Territory, Canada, Unpublished PhD thesis, Technische Universität Braunschweig, Institute of Geology and Palaeontology, 160 p.

Laznicka, P., 1976, Barite Nodules of Possibly Late Diagenetic Origin from Twitya River Area, Mackenzie Mountains, Northwest Territories: *Canadian Journal of Earth Sciences*, v. 13, p. 1446-1455.

Leach, D.L., Bradley, D.C., Huston, D., Pisarevsky, S.A., Taylor, R.D., and Gardoll, S.J., 2010, Sediment-Hosted Lead-Zinc Deposits in Earth History: *Economic Geology*, v. 105, p. 593-625.

Lev, S.M., McLennan, S.M., and Hanson, G.N., 1999, Mineralogic controls on REE mobility during black-shale diagenesis: *Journal of Sedimentary Research*, v. 69, p. 1071-1082.

Long, H.B., Long, J.C., Zhong, Y.R., Zhuang, S.J., and Liu, T., 1994, Existence of hyalophanite in the Zhangcun-Zhengfang black shales vanadium deposit - Evidence for a hydrothermal genesis: *Chinese Science Bulletin*, v. 39, p. 1824-1827.

Ludwig, K.R., 2000, *A geochronological toolkit for Microsoft Excel*, Berkeley, California, Berkeley Geochronology Center Special Publication 1a, 54 p.

Machel, H.G., 2001, Bacterial and thermochemical sulfate reduction in diagenetic settings - old and new insights: *Sedimentary Geology*, v. 140, p. 143-175.

Machel, H.G., Krouse, H.R., and Sassen, R., 1995, Products and Distinguishing Criteria of Bacterial and Thermochemical Sulfate Reduction: *Applied Geochemistry*, v. 10, p. 373-389.

Mair, J.L., Hart, C.J.R., and Stephens, J.R., 2006, Deformation history of the northwestern Selwyn Basin, Yukon, Canada: Implications for orogen evolution and mid-Cretaceous magmatism: *Geological Society of America Bulletin*, v. 118, p. 304-323.

Mathur, R., Ruiz, J., and Tornos, F., 1999, Age and sources of the ore at Tharsis and Rio Tinto, Iberian Pyrite Belt, from Re-Os isotopes: *Mineralium Deposita*, v. 34, p. 790-793.

McDonough, W.F., and Sun, S.S., 1995, The composition of the earth: *Chemical Geology*, v. 120, p. 223-253.

McLennan, S.M., 1989, Rare-Earth Elements in Sedimentary-Rocks - Influence of Provenance and Sedimentary Processes: *Reviews in Mineralogy*, v. 21, p. 169-200.

McLennan, S.M., Bock, B., Hemming, S.R., Hurowitz, J.A., Lev, S.M., and McDaniel, D.K., 2003, The roles of provenance and sedimentary processes in the geochemistry of sedimentary rocks, in Lentz, D.R., ed., *Geochemistry of sediments and sedimentary rocks: Evolutionary considerations to mineral deposit-forming environments*, Geological Association of Canada, *GeoText* 4, p. 7-38.

Meyer, K.M., and Kump, L.R., 2008, Oceanic euxinia in Earth history: Causes and consequences: *Annual Review of Earth and Planetary Sciences*, v. 36, p. 251-288.

Milliken, K.L., 2004, Late Diagenesis and Mass Transfer in Sandstone-Shale sequences, in Mackenzie, F.T., ed., *Sediments, Diagenesis and Sedimentary Rocks, Volume 7: Treatise on Geochemistry*: Oxford, Elsevier-Pergamon, p. 159-182.

Morelli, R.M., Creaser, R.A., Selby, D., Kelley, K.D., Leach, D.L., and King, A.R., 2004, Re-Os sulfide geochronology of the Red Dog sediment-hosted Zn-Pb-Ag deposit, Brooks Range, Alaska: *Economic Geology*, v. 99, p. 1569-1576.

Moro, M.C., Cembranos, M.L., and Fernandez, A., 2001, Celsian, (Ba,K)-feldspar and cymrite from sedex barite deposits of Zamora, Spain: *Canadian Mineralogist*, v. 39, p. 1039-1051.

Obolensky, A.A., Gushchina, L.V., Borisenko, A.S., Borovikov, A.A., and Pavlova, G.G., 2007, Antimony in hydrothermal processes: solubility, conditions of transfer, and metal-bearing capacity of solutions: *Russian Geology and Geophysics*, v. 48, p. 992-1001.

Ohmoto, H., Kaiser, C.J., and Geer, K.A., 1990, Systematics of sulphur isotopes in recent marine sediments and ancient sediment-hosted basemetal deposits, in Herbert, H.M., and Ho, S.E., eds., *Stable Isotopes and Fluid Processes in Mineraliza-*

tion, The University of Western Australia Publication No. 23, p. 70-120.

Osadchii, E.G., 1996, Kesterite-sphalerite geothermometer and physicochemical conditions of cassiterite-polymetallic deposit formation in the Dachang ore field (PR China): *Geology of Ore Deposits*, v. 38, p. 197-207.

Paradis, S., Nelson, J.L., and Irwin, S.E.B., 1998, Age constraints on the Devonian shale-hosted Zn-Pb-Ba deposits, Gataga district, northeastern British Columbia, Canada: *Economic Geology and the Bulletin of the Society of Economic Geologists*, v. 93, p. 184-200.

Paytan, A., Mearon, S., Cobb, K., and Kastner, M., 2002, Origin of marine barite deposits: Sr and S isotope characterization: *Geology*, v. 30, p. 747-750.

Pearson, D.G., and Woodland, S.J., 2000, Solvent extraction/anion exchange separation and determination of PGEs (Os, Ir, Pt, Pd, Ru) and Re-Os isotopes in geological samples by isotope dilution ICP-MS: *Chemical Geology*, v. 165, p. 87-107.

Peng, Z.N., Watanabe, M., Hoshino, K., and Shibata, Y., 1999, Ore mineralogy of tin-polymetallic (Sn-Sb-Fe-Pb-Zn-Cu-Ag) ores in the Dachang tin field, Guangxi, China and their implications for the ore genesis: *Neues Jahrbuch Fur Mineralogie-Abhandlungen*, v. 175, p. 125-151.

Piper, D.Z., 1994, Seawater as the Source of Minor Elements in Black Shales, Phosphorites and Other Sedimentary-Rocks: *Chemical Geology*, v. 114, p. 95-114.

Potter, P.E., Maynard, J.B., and Pryor, W.A., 1980, *Sedimentology of Shale: Study guide and reference source*, Springer, 306 p.

Roots, C., and Martel, E., 2008, Provisional bedrock geology of the Sekwi Mountain map area (NTS 105P and parts of 106A, 95M and 96D), Mackenzie Mountains, Northwest Territories: Northwest Territories Geoscience Office, NWT Open Report 2008-04.

Sageman, B.B., and Lyons, T.W., 2004, Geochemistry of fine-grained sediments and sedimentary rocks, in Mackenzie, F.T., ed., *Sediments, Diagenesis and Sedimentary Rocks, Volume 7: Treatise on Geochemistry*: Oxford, Elsevier-Pergamon, p. 542-564.

Schrijver, K., Zartman, R.E., and Williamsjones, A.E., 1994, Lead and barium sources in cambrian siliciclastics and sediment provenance of a sector of the Taconic Orogen, Quebec – A mixing scenario based on Pb-isotopic evidence: *Applied Geochemistry*, v. 9, p. 455-476.

Seal, R.R., Alpers, C.N., and Rye, R.O., 2000, Stable isotope systematics of sulfate minerals, *Sulfate Minerals - Crystallography, Geochemistry and Environmen-*

tal Significance, Volume 40: Reviews in Mineralogy & Geochemistry: Washington, Mineralogical Soc America, p. 541-602.

Selby, D., and Creaser, R.A., 2005, Direct radiometric dating of the Devonian-Mississippian time-scale boundary using the Re-Os black shale geochronometer: *Geology*, v. 33, p. 545-548.

SellesMartinez, J., 1996, Concretion morphology, classification and genesis: *Earth-Science Reviews*, v. 41, p. 177-210.

Shirey, S.B., and Walker, R.J., 1995, Carius tube digestion for low-blank Rhenium-Osmium analysis: *Analytical Chemistry*, v. 67, p. 2136-2141.

Slack, J.F., Dumoulin, J.A., Schmidt, J.M., Young, L.E., and Rombach, C.S., 2004, Paleozoic sedimentary rocks in the Red Dog Zn-Pb-Ag district mid vicinity western Brooks Range, Alaska: Provenance, deposition, and metallogenic significance: *Economic Geology*, v. 99, p. 1385-1414.

Stow, D.A.V., Huc, A.Y., and Bertrand, P., 2001, Depositional processes of black shales in deep water: *Marine and Petroleum Geology*, v. 18, p. 491-498.

Sverjensky, D.A., 1984, Europium redox equilibria in aqueous-solution: *Earth and Planetary Science Letters*, v. 67, p. 70-78.

Taylor, S.R., and McLennan, S.M., 1985, *The continental crust, its composition and evolution : an examination of the geochemical record preserved in sedimentary rocks*: Oxford ; Melbourne :, Blackwell Scientific Publications.

Taylor, S.R., and McLennan, S.M., 1995, The Geochemical Evolution of the Continental-Crust: *Reviews of Geophysics*, v. 33, p. 241-265.

Torres, M.E., Bohrmann, G., and Suess, E., 1996a, Authigenic barites and fluxes of barium associated with fluid seeps in the Peru subduction zone: *Earth and Planetary Science Letters*, v. 144, p. 469-481.

Torres, M.E., Brumsack, H.J., Bohrmann, G., and Emeis, K.C., 1996b, Barite fronts in continental margin sediments: A new look at barium remobilization in the zone of sulfate reduction and formation of heavy barites in diagenetic fronts: *Chemical Geology*, v. 127, p. 125-139.

Turgeon, S.C., Creaser, R.A., and Algeo, T.J., 2007, Re-Os depositional ages and seawater Os estimates for the Frasnian-Famennian boundary: Implications for weathering rates, land plant evolution, and extinction mechanisms: *Earth and Planetary Science Letters*, v. 261, p. 649-661.

Turner, R.J.W., and Goodfellow, W.D., 1990, Barium carbonate bodies associated with the Walt [Cathy] Stratiform barium deposit, Selwyn Basin, Yukon: A possible vent complex associated with a Middle Devonian sedimentary exhalative

barite deposit., Current Research, Part E. Cordillera and Pacific Margin, Geological Survey of Canada, Paper 90-1E, p. 309-319.

Turner, R.J.W., and Rhodes, D., 1990, Boundary Creek zinc deposit (Nidd property), MacMillan Pass, Yukon: sub-seafloor sediment-hosted mineralization associated with volcanism along a late Devonian syndepositional fault: Geological Survey of Canada Current Research, v. 90-1E, p. 321-335.

Veizer, J., Ala, D., Azmy, K., Bruckschen, P., Buhl, D., Bruhn, F., Carden, G.A.F., Diener, A., Ebner, S., Godderis, Y., Jasper, T., Korte, C., Pawellek, F., Podlaha, O.G., and Strauss, H., 1999, Sr-87/Sr-86, delta C-13 and delta O-18 evolution of Phanerozoic seawater: *Chemical Geology*, v. 161, p. 59-88.

Volkening, J., Walczyk, T., and Heumann, K.G., 1991, Osmium isotope ratio determinations by Negative Thermal Ionization Mass-Spectrometry: *International Journal of Mass Spectrometry and Ion Processes*, v. 105, p. 147-159.

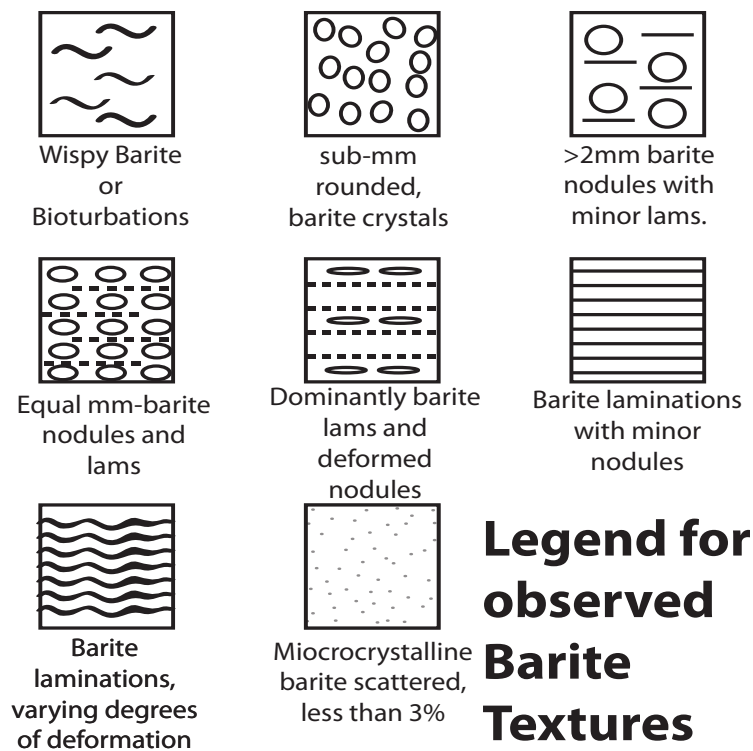
Wilde, P., Quinby-Hunt, M.S., and Erdtmann, B.D., 1996, The whole-rock cerium anomaly: A potential indicator of eustatic sea-level changes in shales of the anoxic facies: *Sedimentary Geology*, v. 101, p. 43-53.

Wilkin, R.T., and Barnes, H.L., 1997, Formation processes of framboidal pyrite: *Geochimica Et Cosmochimica Acta*, v. 61, p. 323-339.

Wilkin, R.T., Arthur, M.A., and Dean, W.E., 1997, History of water-column anoxia in the Black Sea indicated by pyrite framboid size distributions: *Earth and Planetary Science Letters*, v. 148, p. 517-525.

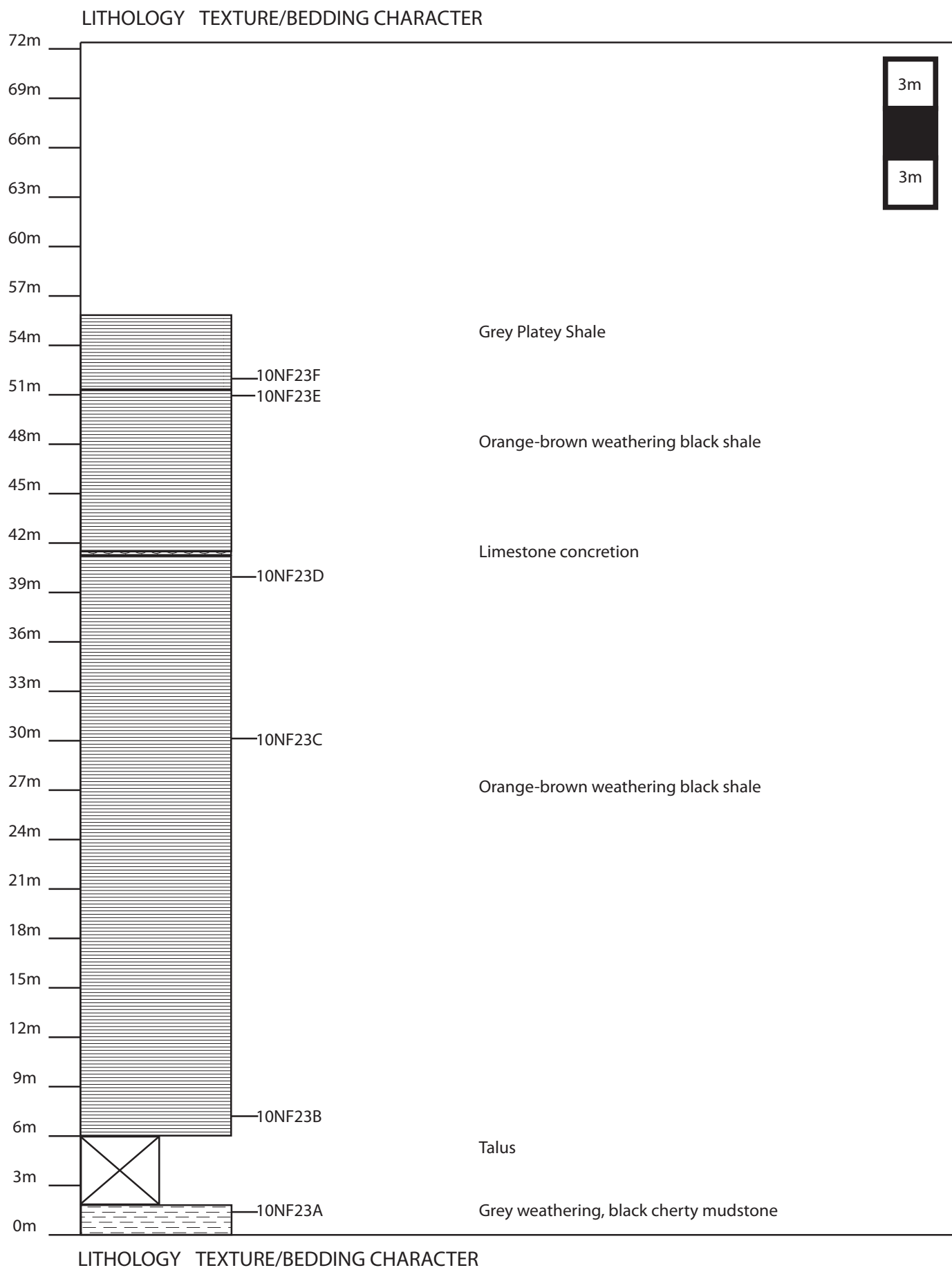
## APPENDIX A: STRATIGRAPHIC SECTIONS

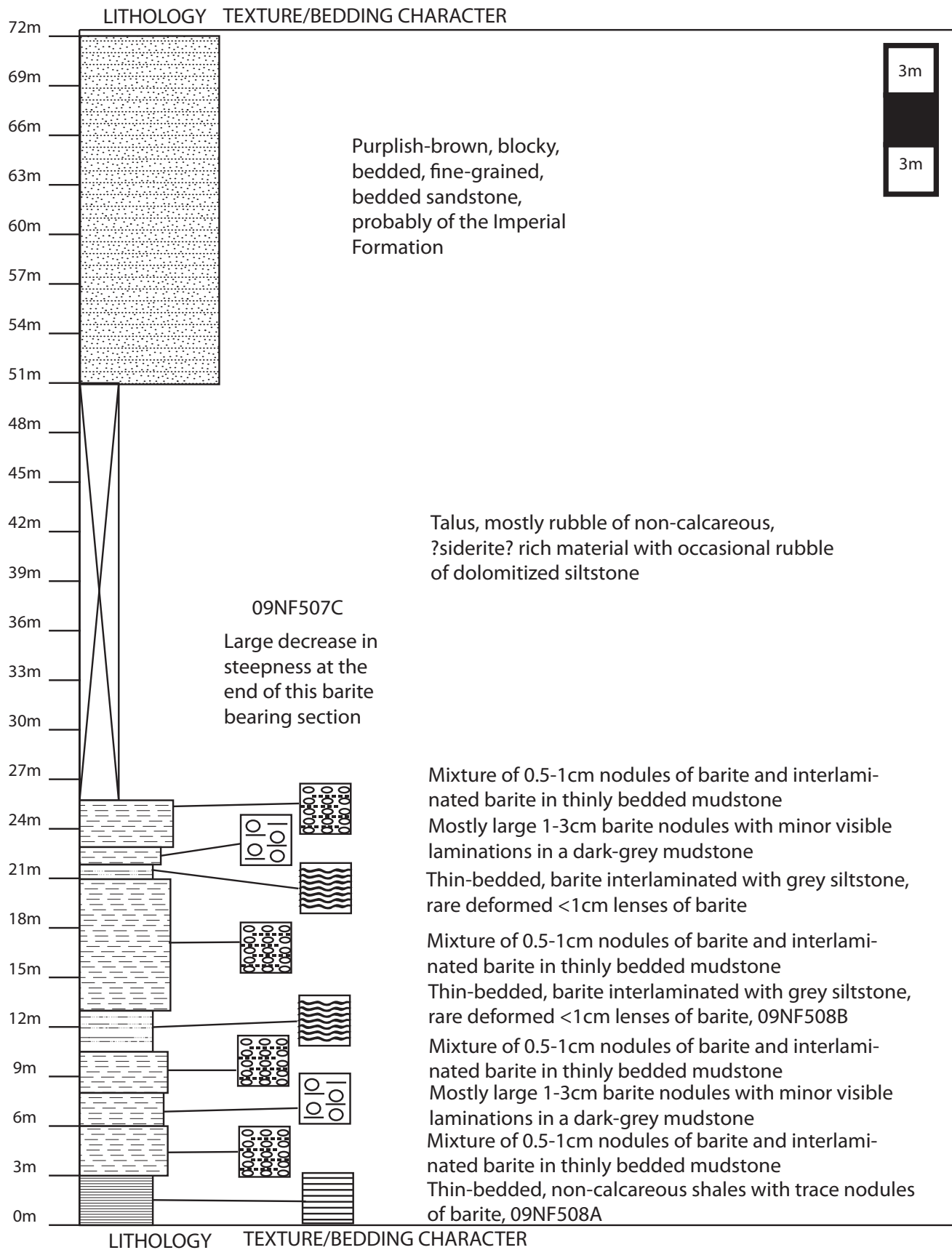
Note: Width of stratiigraphic sections represents the relative prominence of subunits within a section



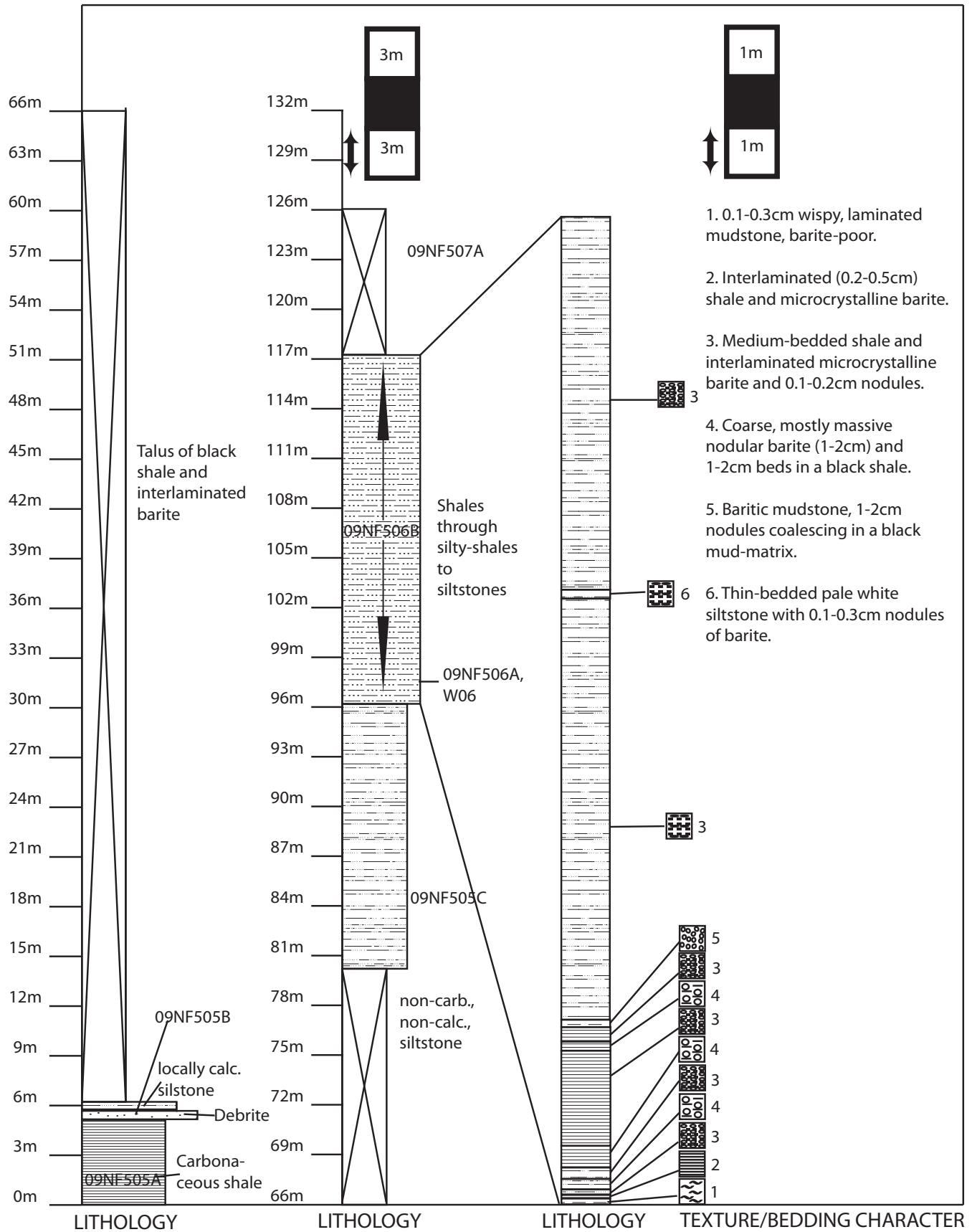
UTM COORDINATES NAD83 ZONE 9: 432835.762E 7102001.816N

Taiga

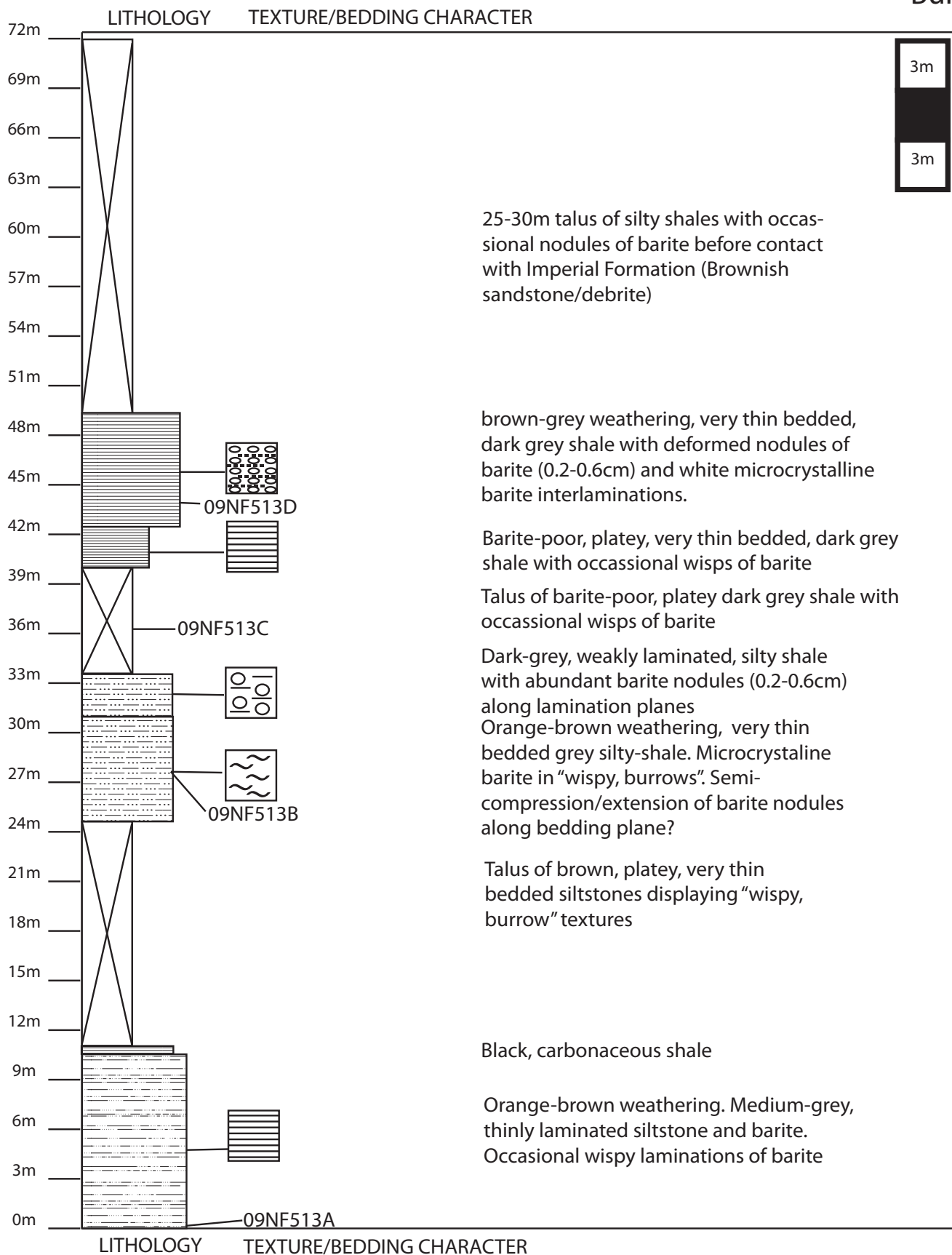




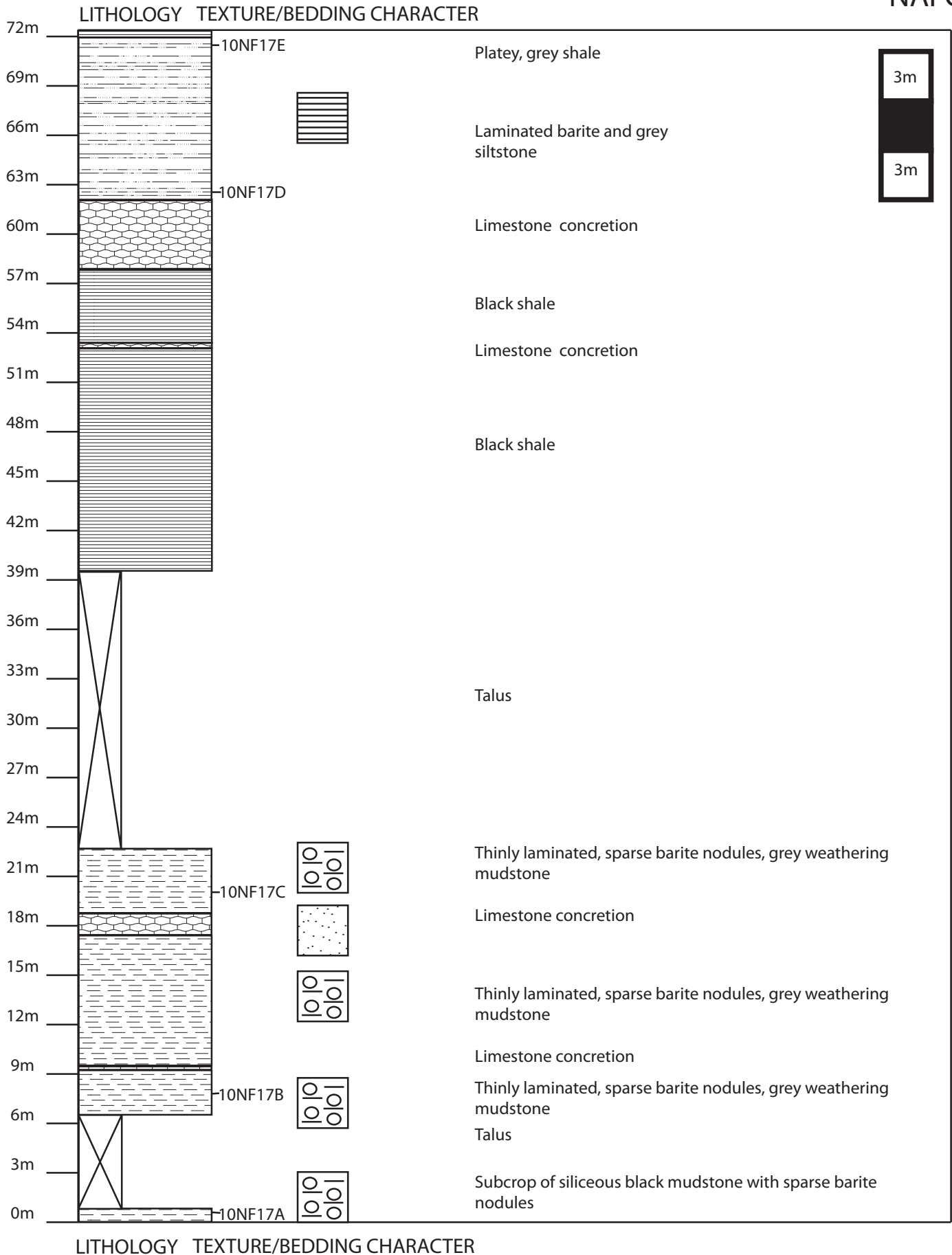
Neil Fernandes, University of Alberta

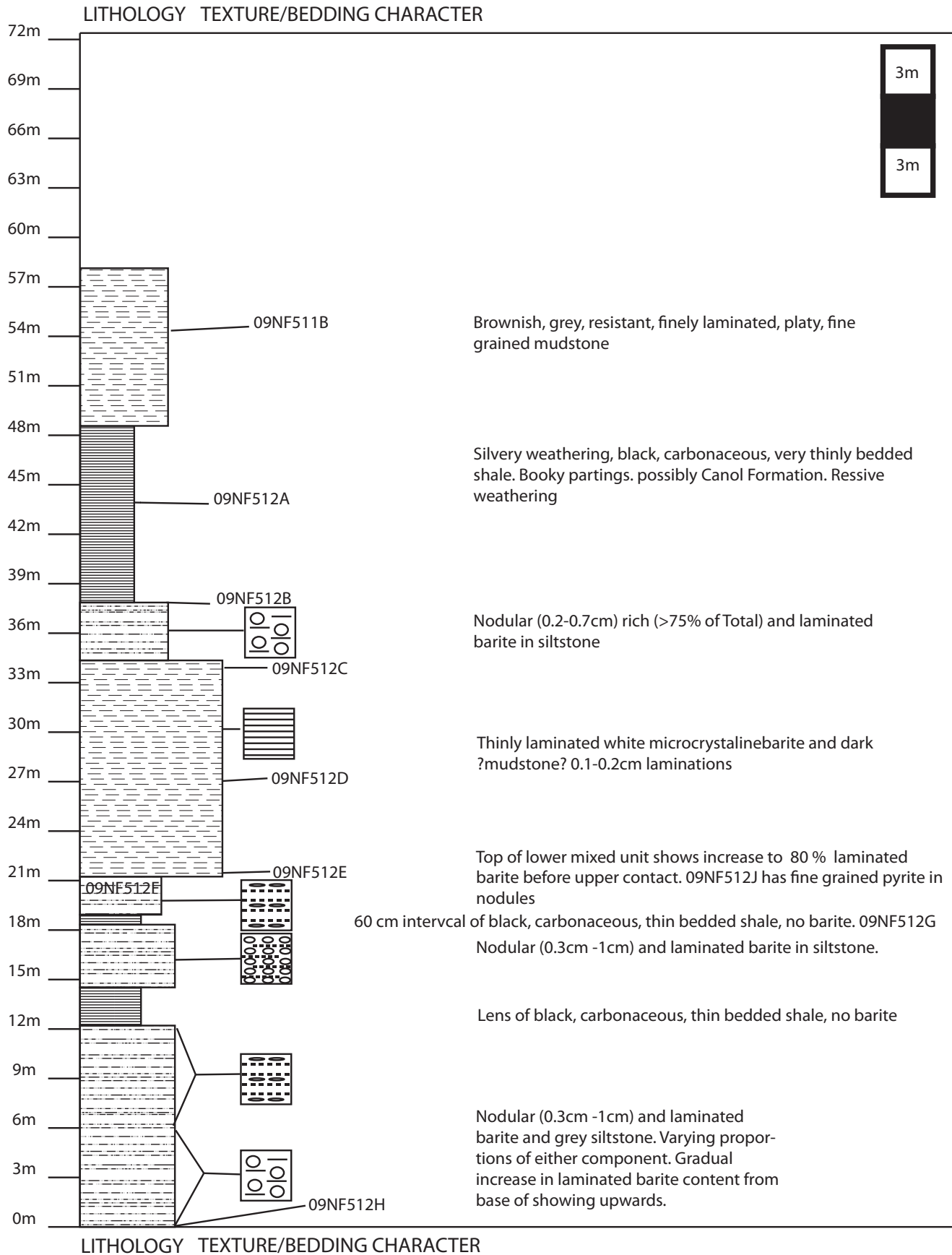


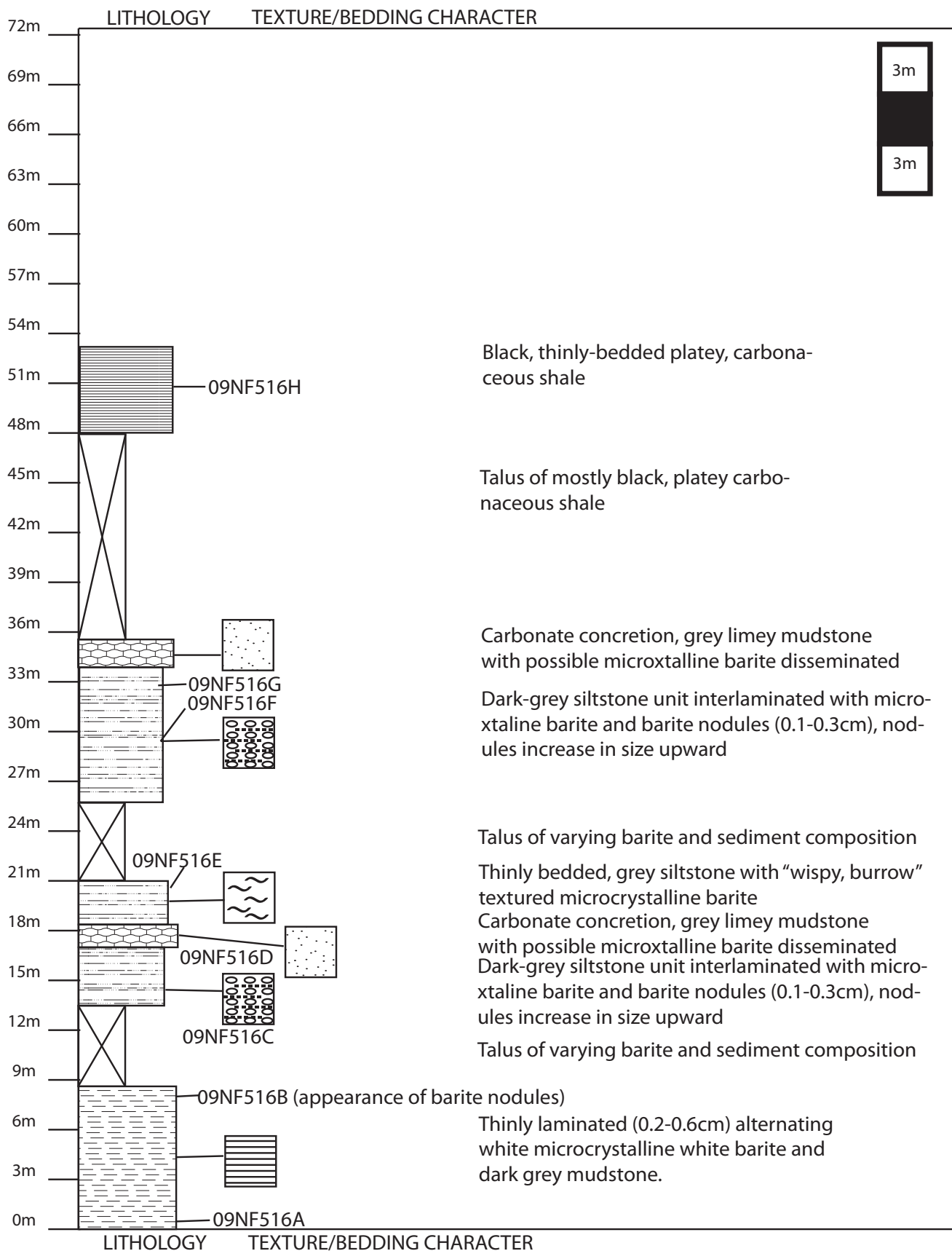
Neil Fernandes, University of Alberta



Neil Fernandes, University of Alberta

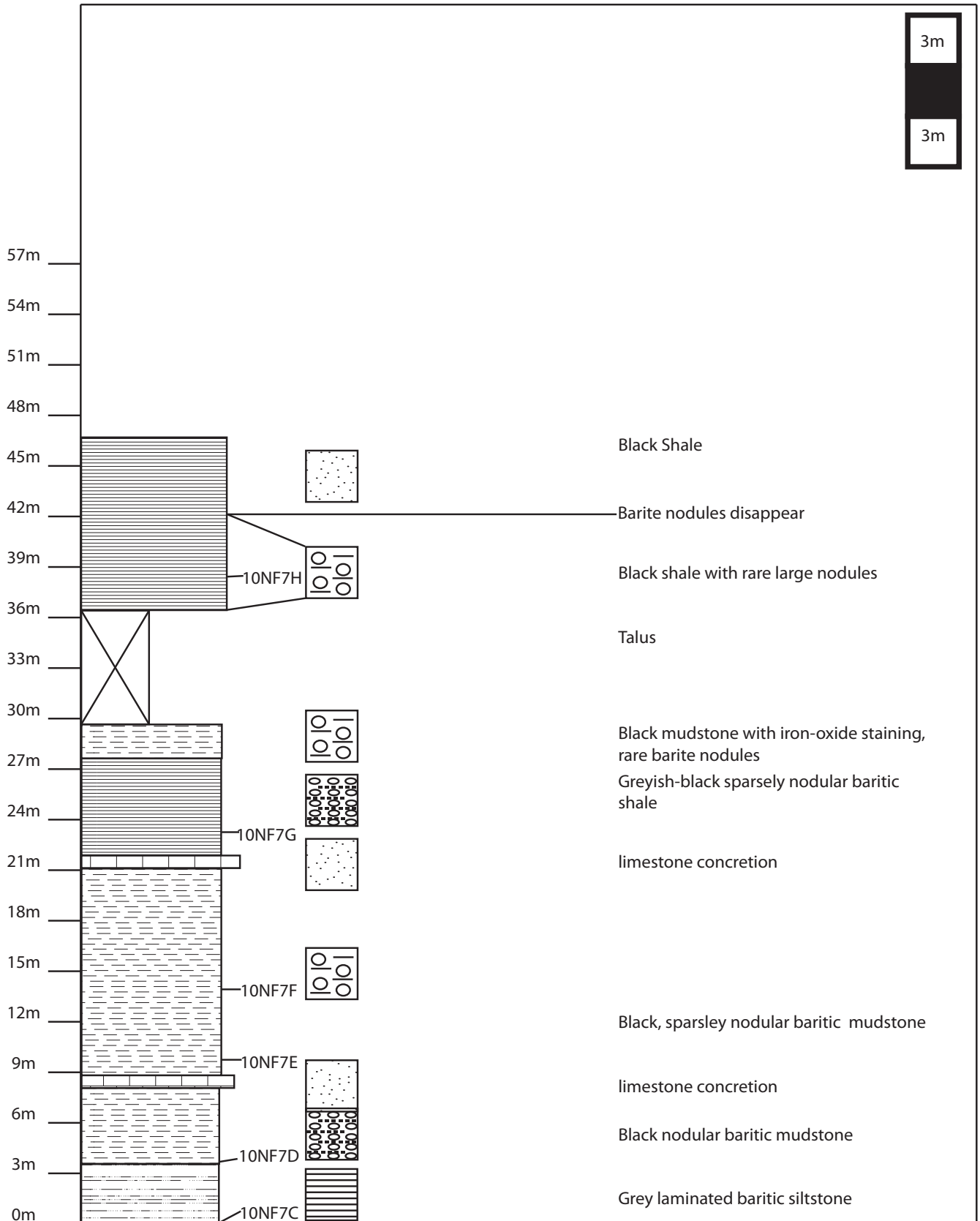






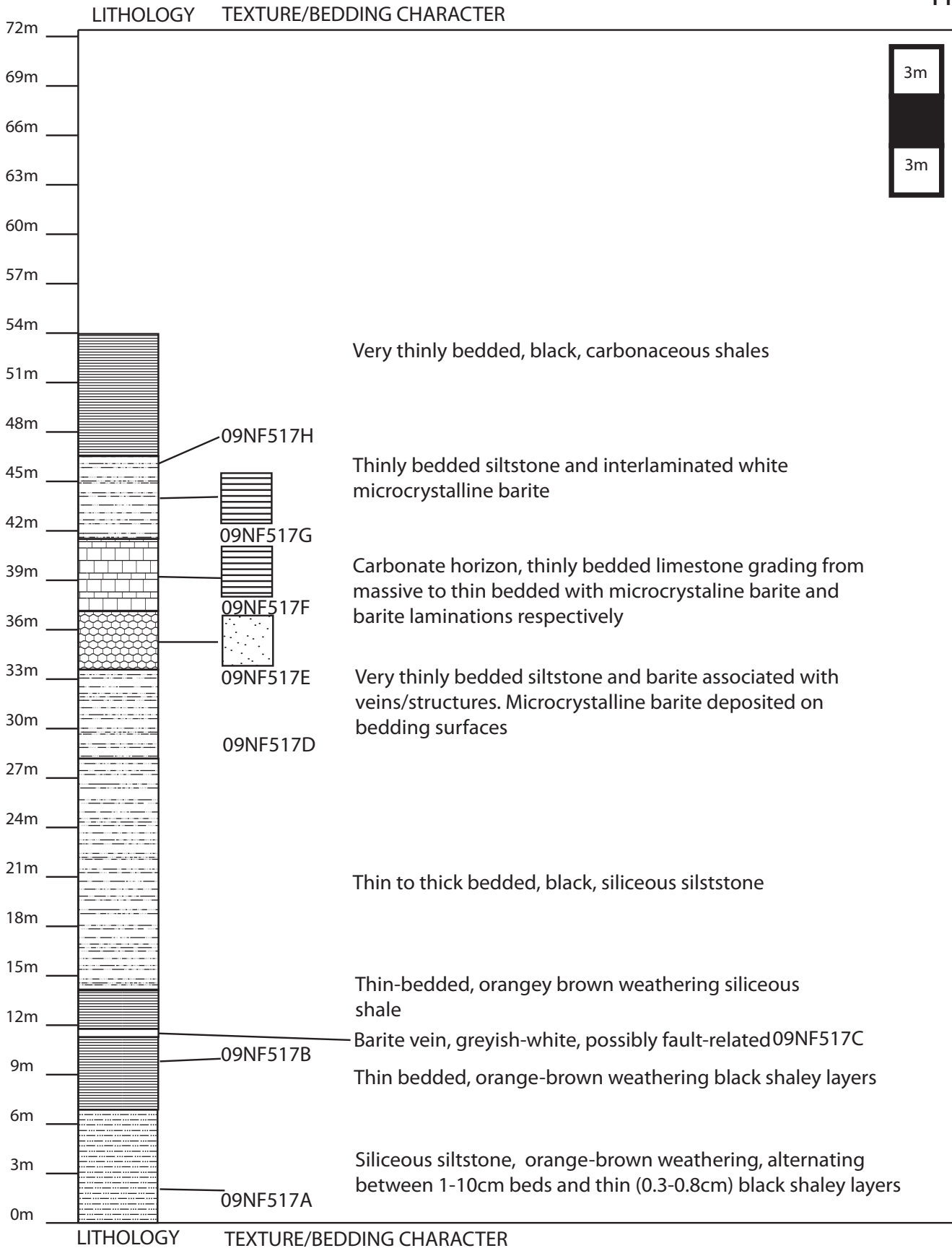
Neil Fernandes, University of Alberta

LITHOLOGY TEXTURE/BEDDING CHARACTER



LITHOLOGY TEXTURE/BEDDING CHARACTER

Neil Fernandes, University of Alberta



Neil Fernandes, University of Alberta

## **APPENDIX B: MICROPROBE DATA**

See attached CD for pdf file

## **APPENDIX C: LITHOGEOCHEMISTRY DATA**

Location	NWT				Yukon	
	Sample	09NF500E	09NF505A	10NF8A	10NF8B	10NF32A
<b>SiO<sub>2</sub> (wt %)</b>	50.64	76.48	81.99	78.70	25.71	77.64
<b>Al<sub>2</sub>O<sub>3</sub></b>	6.83	6.51	6.88	9.95	4.79	9.67
<b>Fe<sub>2</sub>O<sub>3</sub>(T)</b>	4.81	5.41	2.34	2.17	6.28	0.39
<b>MnO</b>	0.022	0.006	0.00	0.00	0.10	0.00
<b>MgO</b>	1.43	0.38	0.49	0.75	10.89	0.41
<b>CaO</b>	11.5	0.16	0.17	0.08	19.88	0.03
<b>Na<sub>2</sub>O</b>	0.05	0.10	0.19	0.23	0.05	0.06
<b>K<sub>2</sub>O</b>	1.58	1.63	1.73	2.52	1.41	2.42
<b>TiO<sub>2</sub></b>	0.328	0.335	0.402	0.570	0.25	0.45
<b>P<sub>2</sub>O<sub>5</sub></b>	0.12	0.52	0.17	0.20	0.03	< 0.01
<b>C<sub>org</sub></b>	0.11	1.33	1.48	1.45	7.82	2.35
<b>LOI</b>	21.83	6.58	29.68	6.55	5.17	4.96
<b>Total</b>	99.14	98.12	99.05	97.63	99.53	100.10
<b>Total S</b>	n.a.	n.a.	0.86	0.31	0.18	0.20
<b>CO<sub>2</sub></b>	n.a.	n.a.	0.09	0.09	27.80	0.53
<b>SO<sub>4</sub></b>	n.a.	n.a.	1.00	0.40	< 0.3	< 0.3
<b>Rb (ppm)</b>	61	73	72	117	51	111
<b>Cs</b>	3.7	4.6	5.3	10.2	2.0	8.4
<b>Sr</b>	216	359	113	61	466	16
<b>Ba</b>	3079	3209	11830	6245	2099	4641
<b>Y</b>	38.8	25.7	14.6	19.3	23.1	21.1
<b>La</b>	36.8	25.3	22.6	30.5	16.8	22.1
<b>Ce</b>	40.6	42.5	35.4	50.7	33.7	32.7
<b>Pr</b>	7.3	7.93	5.06	6.78	4.06	5.36
<b>Nd</b>	27.3	37.6	16.3	23.4	15.7	20.2
<b>Sm</b>	5.18	10	2.30	3.02	3.80	3.72
<b>Eu</b>	1.06	2.01	0.44	0.45	0.89	0.60
<b>Gd</b>	4.81	8.25	1.85	2.01	4.07	2.87
<b>Tb</b>	0.79	1.13	0.32	0.37	0.65	0.46
<b>Dy</b>	4.85	5.54	2.17	2.61	3.65	2.83
<b>Ho</b>	1.04	1.01	0.52	0.64	0.72	0.61
<b>Er</b>	3.17	2.65	1.66	2.04	2.02	1.90
<b>Tm</b>	0.503	0.38	0.28	0.34	0.30	0.31
<b>Yb</b>	3.46	2.43	1.94	2.42	1.92	1.98
<b>Lu</b>	0.564	0.403	0.33	0.44	0.33	0.35
<b>Hf</b>	2.4	2.4	2.20	2.70	1.80	1.80
<b>Ce/Ce<sup>o</sup></b>	0.59	0.71	0.84	0.87	0.99	0.73
<b>Eu/Eu<sup>o</sup></b>	0.65	0.67	0.65	0.56	0.69	0.56
<b>Sc</b>	10	10	8	12	5	7
<b>Be</b>	2	2	2	2	1	2
<b>V</b>	634	756	493	658	59	1670
<b>Cr</b>	80	130	100	130	40	60
<b>Co</b>	10	3	2	< 1	3	< 1
<b>Ni</b>	350	30	< 20	< 20	30	< 20
<b>Cu</b>	110	60	30	< 10	20	20

**Table C1: Lithogemistry of background Lower Earn Group sediments**

Location	NWT				Yukon	
Sample	09NF500E	09NF505A	10NF8A	10NF8B	10NF32A	10NF38A
Zn	510	320	50	50	90	< 30
Ga	10	12	11	17	8	11
Ge	1.6	2.8	1.1	2.0	0.8	1.6
As	65	43	< 5	6	21	9
Zr	108	103	102	125	86	93
Nb	10.8	10	8.80	12.80	4.40	7.00
Mo	114	33	9	9	3	10
Ag	1.1	1.4	1.40	1.30	0.60	1.30
In	< 0.1	< 0.1	< 0.1	< 0.1	< 0.1	< 0.1
Sn	< 1	1	1	2	1	3
Sb	33.2	19.3	5.70	7.60	2.10	31.20
Ta	0.50	0.53	0.68	0.98	0.32	1.30
W	0.7	1.8	1.1	1.3	0.5	4.1
Tl	0.36	1.18	0.77	1.08	0.34	1.78
Pb	29	22	7	10	7	18
Bi	0.1	< 0.1	< 0.1	< 0.1	< 0.1	0.10
Th	5.30	7.12	5.01	7.99	4.38	5.31
U	22.4	9.35	3.08	4.15	1.93	5.50

**Table C1: Lithogemistry of background Lower Earn Group sediments**

Location	Taiga section, NWT					
Sample	10NF23A	10NF23B	10NF23C	10NF23D	10NF23E	10NF23F
SiO <sub>2</sub> (wt %)	91.81	68.99	83.65	82.74	78.32	85.3
Al <sub>2</sub> O <sub>3</sub>	2.05	5.72	3.43	4.4	7.29	4.69
Fe <sub>2</sub> O <sub>3</sub> (T)	0.42	3.39	1.1	1.2	1.22	1.03
MnO	0.003	0.003	0.004	0.002	0.003	0.002
MgO	0.14	0.29	0.15	0.22	0.19	0.33
CaO	0.03	0.07	0.07	0.09	0.23	0.05
Na <sub>2</sub> O	0.04	0.08	0.04	0.07	0.08	0.07
K <sub>2</sub> O	0.47	1.74	0.76	1.05	1.89	1.12
TiO <sub>2</sub>	0.089	0.439	0.161	0.233	0.187	0.234
P <sub>2</sub> O <sub>5</sub>	0.02	0.06	0.06	0.06	0.09	0.05
LOI	3.34	13.72	7.15	6.55	6.38	6.45
Total	98.41	94.5	96.58	96.61	95.88	99.31
C <sub>Org</sub>	2.03	5.27	3.28	2.72	2.77	3.45
Total S	0.2	2.56	1	0.8	0.82	0.39
CO <sub>2</sub>	0.06	2.78	0.65	0.51	0.47	0.28
SO <sub>4</sub>	< 0.3	3.7	1.6	1.4	1.2	< 0.3
Rb (ppm)	23	64	34	46	63	55
Cs	1.5	3.1	1.9	2.4	2	3.9
Sr	13	107	62	61	68	26
Ba	2493	59670	28200	24840	47830	4960
Y	3.1	25.5	8.7	8.7	9.1	7.5
La	5.47	42	8.34	7.9	21.1	39.8

**Table C2: Lithogeochemistry of Taiga section Lower Earn Group sediments**

Location	Taiga section, NWT					
Sample	10NF23A	10NF23B	10NF23C	10NF23D	10NF23E	10NF23F
Ce	8.35	50	13.5	11.7	36.1	62.4
Pr	1.18	7.16	2.03	1.56	5.55	7.59
Nd	3.99	26.5	8.12	6.04	21.3	24.8
Sm	0.42	4.98	1.92	1.46	3.76	2.68
Eu	0.048	0.303	0.087	0.043	< 0.005	0.302
Gd	0.3	4.17	1.64	1.27	2.32	1.21
Tb	0.05	0.58	0.24	0.21	0.31	0.17
Dy	0.37	3.26	1.26	1.18	1.44	1.10
Ho	0.09	0.72	0.26	0.28	0.28	0.24
Er	0.32	2.11	0.77	0.83	0.79	0.75
Tm	0.062	0.334	0.112	0.142	0.113	0.121
Yb	0.49	2.36	0.8	0.94	0.83	0.82
Lu	0.088	0.432	0.146	0.163	0.126	0.145
Hf	0.4	1.7	0.7	0.9	0.8	0.8
Ce/Ce <sup>o</sup>	0.82	0.67	0.79	0.78	0.82	0.88
Eu/Eu <sup>o</sup>	0.41	0.20	0.15	0.10	-	0.51
Sc	2	9	4	6	5	5
Be	<1	2	<1	1	3	1
V	620	273	688	726	568	1107
Cr	30	50	30	30	40	30
Co	<1	<1	<1	<1	1	<1
Ni	<20	<20	20	<20	30	<20
Cu	<10	20	20	20	10	10
Zn	<30	<30	<30	30	70	<30
Ga	4	9	5	7	7	9
Ge	1.6	<0.5	<0.5	0.5	1.4	0.9
As	<5	12	7	9	15	12
Zr	21	73	30	38	30	34
Nb	1.4	6.1	2.3	2.8	3.3	2.7
Mo	14	26	22	19	19	16
Ag	<0.5	0.9	<0.5	<0.5	<0.5	0.5
In	<0.1	<0.1	<0.1	<0.1	<0.1	<0.1
Sn	<1	<1	<1	<1	<1	<1
Sb	7.6	25.7	3.2	6.5	10.8	12.5
Ta	0.12	0.54	0.22	0.28	0.37	0.3
W	0.6	1.6	<0.5	0.8	3	0.5
Tl	0.85	3.08	1.36	1.9	0.67	2.19
Pb	<5	6	<5	<5	62	5
Bi	<0.1	<0.1	<0.1	<0.1	<0.1	<0.1
Th	1.22	6.02	2.4	3.18	2.95	3.58
U	1.42	6.19	4.03	4.60	3.90	4.72

**Table C2: Lithochemistry of Taiga section Lower Earn Group sediments**

Location	NWT									
	Sample	09NF508A	09NF511B	09NF512A	09NF512G	09NF512H	09NF512I	AX09-08	AX-09-10	09NF513B
<b>SiO<sub>2</sub> (wt %)</b>	76.22	78.26	84.74	80.72	75.84	83.68	75.82	83.76	81.06	72.47
<b>Al<sub>2</sub>O<sub>3</sub></b>	5.85	4.96	5.57	5.38	3.42	4.06	5.59	2.17	4.2	9.24
<b>Fe<sub>2</sub>O<sub>3</sub>(T)</b>	0.56	1.72	0.46	1.54	1.9	1.62	6.22	0.97	1.67	3.02
<b>MnO</b>	0.003	0.004	0.001	0.004	0.004	0.003	0.007	0.005	0.004	0.01
<b>MgO</b>	0.37	0.23	0.35	0.18	0.17	0.18	0.31	0.22	0.27	0.33
<b>CaO</b>	0.1	0.17	0.03	0.09	0.16	0.09	0.24	0.22	0.36	0.49
<b>Na<sub>2</sub>O</b>	0.06	0.07	0.09	0.06	0.05	0.06	0.07	0.06	0.06	0.07
<b>K<sub>2</sub>O</b>	1.31	0.95	1.27	0.89	0.73	0.88	1.16	0.48	1.01	1.64
<b>TiO<sub>2</sub></b>	0.302	0.254	0.268	0.239	0.166	0.198	0.327	0.107	0.232	0.618
<b>P<sub>2</sub>O<sub>5</sub></b>	0.03	0.04	0.02	0.08	0.22	0.06	0.7	0.05	0.06	0.38
<b>LOI</b>	7.23	7.79	6.59	7.26	8.92	7.87	9.38	7.27	7.95	6.81
<b>Total</b>	92.03	94.44	99.39	96.44	91.58	98.7	99.83	95.31	96.87	95.09
<b>C<sub>Org</sub></b>	1.69	2.28	3.74	3.26	1.72	4.51	3.77	2.37	3.73	1.18
<b>Total S</b>	1.63	<i>N.A.</i>	0.43	1.56	<i>N.A.</i>	1.1	0.45	<i>N.A.</i>	<i>N.A.</i>	2.16
<b>CO<sub>2</sub></b>	2.27	<i>N.A.</i>	0.08	0.32	<i>N.A.</i>	0.41	0.94	<i>N.A.</i>	<i>N.A.</i>	0.16
<b>SO<sub>4</sub></b>	5.5	<i>N.A.</i>	<0.3	1.7	<i>N.A.</i>	1	0.4	<i>N.A.</i>	<i>N.A.</i>	2.5
<b>Rb (ppm)</b>	57	41	64	41	29	39	52	20	43	69
<b>Cs</b>	3.8	2.4	4.7	2.3	1.7	2.2	3.3	1.4	2.1	3.6
<b>Sr</b>	159	66	38	60	248	55	58	189	118	90
<b>Ba</b>	69980	38890	5143	43290	62920	22490	3510	37820	19580	45940
<b>Y</b>	6.9	11.3	8.1	10.5	10.3	10.3	9.7	6.7	13	19.4
<b>La</b>	12.1	14.2	14.5	12.2	11.9	10.9	93.9	11.6	18.2	23.5
<b>Ce</b>	17.5	20.5	22.4	19	12.2	17.7	63.3	15.9	27.5	47.1
<b>Pr</b>	2.11	2.74	3.08	2.51	1.92	2.6	10	2.55	3.86	6.05
<b>Nd</b>	6.72	9.64	10.2	9.37	6.96	9.87	29.8	9.34	14	23.4
<b>Sm</b>	0.76	1.68	1.07	1.75	1.58	2.08	2.86	1.3	2.03	4.77
<b>Eu</b>	<0.005	<0.005	0.127	<0.005	<0.005	0.187	0.495	0.565	0.042	0.512
<b>Gd</b>	0.58	1.74	0.72	1.61	1.93	1.89	1.78	1.35	1.42	3.98
<b>Tb</b>	0.11	0.29	0.15	0.24	0.28	0.29	0.27	0.2	0.25	0.6
<b>Dy</b>	0.71	1.9	1.08	1.36	1.64	1.67	1.61	1.07	1.76	3.34
<b>Ho</b>	0.19	0.41	0.27	0.29	0.35	0.37	0.34	0.22	0.38	0.67
<b>Er</b>	0.66	1.25	0.9	0.96	1.06	1.03	1.08	0.68	1.24	2.08
<b>Tm</b>	0.119	0.191	0.156	0.149	0.167	0.169	0.173	0.105	0.197	0.332
<b>Yb</b>	0.93	1.28	1.07	1.03	1.13	1.06	1.14	0.68	1.29	2.14
<b>Lu</b>	0.157	0.203	0.196	0.178	0.168	0.172	0.199	0.111	0.197	0.368
<b>Hf</b>	1.4	1.5	1.1	1	1.1	1	1.3	0.8	1.3	3.9
<b>Ce/Ce<sup>o</sup></b>	0.85	0.79	0.84	0.82	0.59	0.81	0.48	0.71	0.79	0.97
<b>Eu/Eu<sup>o</sup></b>	-	-	0.44	-	-	0.29	0.67	1.3	0.08	0.36
<b>Sc</b>	5	6	5	6	4	5	6	3	5	12
<b>Be</b>	1	1	2	1	1	<1	2	<1	1	2
<b>V</b>	675	515	1005	974	852	395	405	792	1382	230
<b>Cr</b>	40	50	40	40	80	40	30	30	50	80
<b>Co</b>	1	<1	<1	3	<1	4	3	<1	1	10
<b>Ni</b>	<20	<20	<20	40	<20	70	40	<20	40	50

**Table C3: Litho geochemistry of non-baritic lower Earn Group sediments associated with barite occurrences**

Location	NWT									
Sample	09NF508A	09NF511B	09NF512A	09NF512G	09NF512H	09NF512I	AX09-08	AX-09-10	09NF513B	09NF513C
<b>Cu</b>	< 10	10	< 10	30	< 10	20	20	< 10	< 10	30
<b>Zn</b>	< 30	< 30	< 30	< 30	40	130	290	< 30	190	70
<b>Ga</b>	8	10	11	9	8	7	9	4	9	16
<b>Ge</b>	2.5	1.4	2.3	< 0.5	3	1.8	1.9	1.7	2	2.2
<b>As</b>	8	19	8	10	12	25	56	11	16	16
<b>Zr</b>	53	51	47	40	33	42	54	24	45	159
<b>Nb</b>	4.8	7.4	3.8	3.3	5	2.8	3.8	5.1	6	8
<b>Mo</b>	4	17	15	26	17	34	32	18	21	4
<b>Ag</b>	< 0.5	< 0.5	< 0.5	< 0.5	0.6	< 0.5	0.6	< 0.5	< 0.5	0.9
<b>In</b>	< 0.1	< 0.1	< 0.1	< 0.1	< 0.1	< 0.1	< 0.1	< 0.1	< 0.1	< 0.1
<b>Sn</b>	1	< 1	1	< 1	< 1	1	< 1	< 1	< 1	2
<b>Sb</b>	17.7	11.5	16.3	4.9	9.6	11.7	23.9	6.9	27.2	8
<b>Ta</b>	0.59	0.42	0.62	0.31	0.37	0.61	0.75	0.25	0.35	1.06
<b>W</b>	8	2.5	3.3	0.5	1	2.8	5.2	1.4	2.2	2.8
<b>Tl</b>	0.33	1.29	0.97	1.45	0.08	0.63	1.01	0.11	1.61	0.61
<b>Pb</b>	9	20	12	< 5	10	15	22	12	18	11
<b>Bi</b>	0.2	< 0.1	0.1	< 0.1	< 0.1	0.1	0.4	< 0.1	< 0.1	0.2
<b>Th</b>	2.72	3.72	3.16	3.43	2.08	3.04	4.75	1.88	3	7.41
<b>U</b>	3.13	4.54	3.71	5.05	4.61	4.03	7.87	3.79	5.23	3.78

**Table C3: Litho geochemistry of non-baritic lower Earn Group sediments associated with barite occurrences**

Location	NWT									
Sample	09NF514A	09NF515A	09NF516H	09NF517B	09NF517H	09NF517I	10NF12D	10NF13A	10NF17A	10NF17B
<b>SiO<sub>2</sub> (wt %)</b>	85.12	70.66	84.99	77.24	64.64	65.32	82.66	84.14	86.08	82.75
<b>Al<sub>2</sub>O<sub>3</sub></b>	4.88	4.33	4.36	5.21	7.02	5.33	4.21	6.47	2.58	3
<b>Fe<sub>2</sub>O<sub>3</sub>(T)</b>	0.48	2.21	0.89	2.19	4.1	1.73	1.05	0.94	1.67	1.73
<b>MnO</b>	0.004	0.004	0.002	0.003	0.008	0.015	0.002	0.007	0.002	0.004
<b>MgO</b>	0.3	0.16	0.23	0.3	0.06	0.62	0.18	0.47	0.14	0.13
<b>CaO</b>	0.03	0.06	0.06	0.12	0.22	7.74	0.21	0.23	0.05	0.17
<b>Na<sub>2</sub>O</b>	0.06	0.12	0.07	0.07	0.03	0.05	0.06	0.06	0.06	0.07
<b>K<sub>2</sub>O</b>	1.15	0.75	0.89	1.58	0.86	1.22	0.94	1.6	0.74	0.69
<b>TiO<sub>2</sub></b>	0.237	0.187	0.203	0.306	0.366	0.242	0.189	0.328	0.161	0.141
<b>P<sub>2</sub>O<sub>5</sub></b>	0.02	0.15	0.04	0.08	0.15	0.06	0.02	< 0.01	0.06	0.09
<b>LOI</b>	6.04	11.31	6.99	9.14	10.8	16.23	7.22	4.5	7.77	6.9
<b>Total</b>	98.31	89.94	98.71	96.24	88.25	98.56	96.73	98.74	99.31	95.68
<b>C<sub>Org</sub></b>	3.28	2.31	3.49	< 0.05	0.47	< 0.05	2.53	1.39	3.55	2.6
<b>Total S</b>	<i>N.A.</i>	<i>N.A.</i>	0.81	<i>N.A.</i>	<i>N.A.</i>	<i>N.A.</i>	1.07	0.3	0.94	1.25
<b>CO<sub>2</sub></b>	<i>N.A.</i>	<i>N.A.</i>	0.07	<i>N.A.</i>	<i>N.A.</i>	<i>N.A.</i>	1.69	0.5	1.09	2.09
<b>SO<sub>4</sub></b>	<i>N.A.</i>	<i>N.A.</i>	0.8	<i>N.A.</i>	<i>N.A.</i>	<i>N.A.</i>	2.5	0.4	1.4	3
<b>Rb (ppm)</b>	48	33	46	62	17	55	41	69	33	30
<b>Cs</b>	3.1	2.2	3.6	2.7	0.2	3.7	2.5	5.2	1.8	1.6
<b>Sr</b>	25	327	75	43	163	101	187	41	68	165
<b>Ba</b>	1561	86830	13990	23190	90220	2882	37080	2982	19900	46740
<b>Y</b>	4.9	7.2	3.9	15.3	17.6	19.5	11	10.1	10.2	8.3
<b>La</b>	12.5	11.5	10.1	2.85	21.3	16.5	12	13.5	10.4	6.55

**Table C3: Litho geochemistry of non-baritic lower Earn Group sediments associated with barite occurrences**

Location	NWT									
	Sample	09NF514A	09NF515A	09NF516H	09NF517B	09NF517H	09NF517I	10NF12D	10NF13A	10NF17A
Ce	19	18.5	16.2	6.07	35.5	21.3	19.4	26.4	14.6	7.93
Pr	2.41	2.65	2.05	1.09	4.65	3.37	2.82	3.34	2.66	1.26
Nd	8.08	10.1	7.2	5.41	16.9	12.7	10.3	12.6	10.5	4.95
Sm	0.86	1.87	1.14	1.72	3.49	2.38	1.92	1.99	2.15	1.08
Eu	0.144	< 0.005	0.082	< 0.005	< 0.005	0.461	0.033	0.266	0.267	< 0.005
Gd	0.45	1.74	0.66	1.62	3.36	2.33	1.85	1.08	2.03	1.13
Tb	0.08	0.21	0.09	0.28	0.53	0.42	0.27	0.19	0.3	0.16
Dy	0.61	1.16	0.59	1.86	2.94	2.67	1.53	1.38	1.67	1
Ho	0.16	0.23	0.14	0.41	0.6	0.57	0.32	0.3	0.33	0.22
Er	0.58	0.72	0.48	1.35	1.83	1.84	1	0.93	0.97	0.71
Tm	0.112	0.124	0.087	0.232	0.288	0.293	0.161	0.159	0.139	0.11
Yb	0.86	0.83	0.64	1.62	1.92	1.98	1.05	1.12	0.88	0.83
Lu	0.148	0.132	0.126	0.266	0.299	0.306	0.18	0.192	0.155	0.151
Hf	1.3	1.2	0.9	1.7	2.3	3.1	0.9	1.4	0.8	0.6
Ce/Ce <sup>o</sup>	0.85	0.81	0.86	0.83	0.87	0.68	0.82	0.96	0.67	0.64
Eu/Eu <sup>o</sup>	0.71	-	0.29	-	-	0.6	0.05	0.55	0.39	-
Sc	5	4	5	6	6	6	4	5	4	4
Be	1	1	1	2	2	2	1	1	1	1
V	156	226	983	816	222	1163	749	98	741	623
Cr	40	50	40	60	80	80	30	30	40	30
Co	< 1	2	< 1	< 1	11	3	< 1	< 1	2	3
Ni	< 20	< 20	30	< 20	70	130	30	< 20	40	80
Cu	< 10	30	30	< 10	60	80	20	< 10	20	20
Zn	< 30	90	70	< 30	< 30	4220	< 30	< 30	50	180
Ga	7	7	9	10	9	11	7	10	6	5
Ge	2.1	1.9	3.1	1.4	0.7	4.4	1.4	1	1.5	< 0.5
As	< 5	20	15	9	27	21	15	6	20	7
Zr	48	43	39	71	64	81	35	58	32	28
Nb	6.8	4.6	2.6	8.5	8.7	16.5	2.8	4.9	2.1	1.7
Mo	12	16	13	41	37	49	25	17	42	26
Ag	< 0.5	< 0.5	1	< 0.5	< 0.5	1.3	< 0.5	0.6	< 0.5	< 0.5
In	< 0.1	< 0.1	< 0.1	< 0.1	< 0.1	< 0.1	< 0.1	< 0.1	< 0.1	< 0.1
Sn	< 1	< 1	2	< 1	< 1	3	< 1	1	< 1	< 1
Sb	7.1	6.1	41.1	12	13.8	42.1	7	2.7	12.6	4.3
Ta	0.36	0.33	0.55	0.45	0.73	1.36	0.74	0.48	0.56	0.2
W	0.6	1.4	4.8	7.2	2.8	2.7	4.8	0.7	2.8	0.6
Tl	0.42	< 0.05	0.69	1.59	0.94	0.28	0.5	2.8	0.24	1.02
Pb	22	13	18	30	28	17	14	11	8	< 5
Bi	< 0.1	< 0.1	0.2	< 0.1	0.3	< 0.1	0.2	< 0.1	0.1	< 0.1
Th	3.26	3.03	3.32	4.78	5.63	10.3	2.76	3.54	2.38	1.95
U	2.44	3.8	5.28	5.6	7.16	11	5.02	3.08	5.43	4.61

**Table C3: Litho geochemistry of non-baritic lower Earn Group sediments associated with barite occurrences**

Location	NWT			Yukon
	Sample	10NF17C	10NF7B	10NF7E
<b>SiO<sub>2</sub> (wt %)</b>	81.58	79.86	79.54	80.09
<b>Al<sub>2</sub>O<sub>3</sub></b>	4.52	5.38	6.06	3.58
<b>Fe<sub>2</sub>O<sub>3</sub>(T)</b>	1.03	0.97	0.96	1.24
<b>MnO</b>	0.002	0.002	0.002	0.003
<b>MgO</b>	0.21	0.21	0.29	0.02
<b>CaO</b>	0.06	0.04	0.06	1.02
<b>Na<sub>2</sub>O</b>	0.07	0.07	0.07	0.05
<b>K<sub>2</sub>O</b>	0.97	0.9	1.3	0.9
<b>TiO<sub>2</sub></b>	0.233	0.278	0.339	0.138
<b>P<sub>2</sub>O<sub>5</sub></b>	0.05	0.02	0.03	0.91
<b>LOI</b>	7.98	7.1	6.54	5.67
<b>Total</b>	96.71	94.84	95.17	93.62
<b>C<sub>Org</sub></b>	3.1	3.05	2.41	2.62
<b>Total S</b>	1.18	1.05	0.95	0.96
<b>CO<sub>2</sub></b>	1.12	0.35	0.46	1.33
<b>SO<sub>4</sub></b>	2.4	1.5	2.1	1.9
<b>Rb (ppm)</b>	49	45	63	39
<b>Cs</b>	2.8	3.2	3.7	3
<b>Sr</b>	42	74	56	800
<b>Ba</b>	38510	33580	26730	46460
<b>Y</b>	9	4.5	9.9	21.7
<b>La</b>	5.46	14.3	16.7	11.9
<b>Ce</b>	9.78	19.4	27.9	12.8
<b>Pr</b>	1.76	2.5	3.74	3
<b>Nd</b>	7.33	7.85	13.5	12.2
<b>Sm</b>	1.73	0.92	2.21	2.92
<b>Eu</b>	0.009	< 0.005	0.073	0.2
<b>Gd</b>	1.41	0.63	1.48	3.28
<b>Tb</b>	0.22	0.08	0.23	0.47
<b>Dy</b>	1.36	0.57	1.51	2.7
<b>Ho</b>	0.31	0.15	0.35	0.59
<b>Er</b>	0.97	0.59	1.13	1.74
<b>Tm</b>	0.165	0.125	0.189	0.27
<b>Yb</b>	1.11	0.99	1.27	1.83
<b>Lu</b>	0.194	0.171	0.225	0.33
<b>Hf</b>	1.2	1.2	1.4	0.7
<b>Ce/Ce<sup>o</sup></b>	0.78	0.8	0.86	0.51
<b>Eu/Eu<sup>o</sup></b>	0.02	-	0.12	0.2
<b>Sc</b>	6	6	7	6
<b>Be</b>	1	2	2	1
<b>V</b>	755	621	720	444
<b>Cr</b>	50	70	50	90

**Table C3: Lithochemistry of non-baritic lower Earn Group sediments associated with barite occurrences**

<b>Location</b>	<b>NWT</b>			<b>Yukon</b>
<b>Sample</b>	<b>10NF17C</b>	<b>10NF7B</b>	<b>10NF7E</b>	<b>10NF42C</b>
<b>Co</b>	< 1	2	< 1	1
<b>Ni</b>	20	30	< 20	60
<b>Cu</b>	20	30	20	40
<b>Zn</b>	< 30	< 30	< 30	160
<b>Ga</b>	9	9	11	3
<b>Ge</b>	1.7	2.5	2.3	0.9
<b>As</b>	17	16	18	45
<b>Zr</b>	46	52	59	32
<b>Nb</b>	3.4	4	4.6	2.8
<b>Mo</b>	21	9	14	27
<b>Ag</b>	< 0.5	1.6	0.6	0.9
<b>In</b>	< 0.1	< 0.1	< 0.1	< 0.1
<b>Sn</b>	1	< 1	1	7
<b>Sb</b>	14.5	20.3	21.3	47.8
<b>Ta</b>	0.61	0.87	1.07	1.57
<b>W</b>	2.8	3.8	3.3	3.9
<b>Tl</b>	0.62	0.54	0.92	0.15
<b>Pb</b>	16	51	12	46
<b>Bi</b>	0.2	0.2	0.2	< 0.1
<b>Th</b>	3.36	4.06	4.73	1.99
<b>U</b>	5.04	3.34	4.27	4.23

**Table C3: Lithochemistry of non-baritic lower Earn Group sediments associated with barite occurrences**

Location	NWT												Yukon	
	Sample	09NF506B	09NF508B-W4	09NF512B	09NF512C	09NF512D	09NF512E	09NF516A	09NF516E	BA-09-03	09NF518B	10NF12B	10NF12B	10NF42F
SiO <sub>2</sub> (wt %)	28.98	31.97	64	8.48	3.89	8.82	8.44	62.14	5.75	3	22.02	10.2		
Al <sub>2</sub> O <sub>3</sub>	2.68	2.17	3.56	0.7	0.31	0.52	0.39	3.4	0.42	0.69	1.24	0.76		
Fe <sub>2</sub> O <sub>3</sub> (T)	0.86	0.97	1.89	0.34	0.23	0.2	0.11	0.82	0.17	0.23	0.43	0.36		
MnO	0.004	0.004	0.003	0.004	<0.001	<0.001	0.003	0.004	0.004	0.004	0.001	0.003	0.003	
MgO	0.18	0.15	0.11	0.04	0.02	0.02	0.03	0.16	0.05	0.08	0.03	0.05	0.05	
CaO	0.1	0.24	0.05	0.08	0.04	0.04	0.05	0.06	0.07	0.05	0.03	0.17	0.17	
Na <sub>2</sub> O	0.06	0.05	0.06	0.02	0.01	0.02	0.02	0.11	0.02	0.02	0.02	0.03	0.03	
K <sub>2</sub> O	0.52	0.44	0.92	0.13	0.05	0.1	0.07	0.68	0.08	0.11	0.27	0.14	0.14	
TiO <sub>2</sub>	0.11	0.096	0.22	0.032	0.015	0.027	0.026	0.186	0.017	0.025	0.067	0.033	0.033	
P <sub>2</sub> O <sub>5</sub>	0.19	0.43	0.06	0.07	0.04	0.04	0.02	0.05	0.04	0.03	0.06	0.07	0.07	
LOI	5.48	4.77	7.96	1.67	0.87	1.11	0.77	5.97	1.21	1.25	2.2	1.7	1.7	
Total	39.18	41.28	78.83	11.57	5.48	10.9	9.94	73.58	7.83	5.48	26.38	13.51	13.51	
C <sub>Org</sub>	0.21	0.2	1.15	0.12	0.23	0.31	0.06	0.42	<0.05	<0.05	0.75	0.37	0.37	
Total S	N.A.	N.A.	N.A.	N.A.	13.5	12.5	N.A.	N.A.	N.A.	N.A.	10.1	11.8	11.8	
CO <sub>2</sub>	N.A.	N.A.	N.A.	N.A.	0.53	0.72	N.A.	N.A.	N.A.	N.A.	1.95	1.08	1.08	
SO <sub>4</sub>	N.A.	N.A.	N.A.	N.A.	41.1	40.8	N.A.	N.A.	N.A.	N.A.	31.9	36.2	36.2	
Rb (ppm)	24	21	31	4	2	3	3	26	3	5	10	6	6	
Cs	1.5	1.3	1	<0.1	<0.1	<0.1	<0.1	2	0.3	0.6	0.2	0.4	0.4	
Sr	1628	675	399	755	684	800	780	662	884	1519	830	2338	2338	
Ba	359300	351300	123600	518200	>500000	>500000	530700	151400	547500	549500	418400	493400	493400	
Y	7.5	7.7	2.7	3.1	4.1	3.8	2.1	5.1	2.8	4	6.1	6.5	6.5	
La	8.85	6.47	10.2	4.23	3.04	3.47	3.94	10.6	3.46	1.57	6	8.52	8.52	
Ce	8.55	6.62	13.7	2.2	1.23	1.97	1.88	16.8	2.44	2.42	6.43	2.9	2.9	
Pr	1.27	1.01	1.66	0.37	0.16	0.26	0.31	2.13	0.44	0.4	0.8	0.56	0.56	
Nd	4.42	3.84	5.22	1.65	0.58	0.89	1.37	7.41	2.12	2.06	2.75	2.2	2.2	
Sm	1.09	0.99	0.97	0.47	0.64	0.69	0.37	1.11	0.7	0.68	1.21	0.92	0.92	
Eu	0.246	<0.005	0.522	<0.005	<0.005	<0.005	<0.005	<0.005	0.762	<0.005	<0.005	0.867	0.867	
Gd	1.59	1.48	1.43	0.43	1.48	1.47	0.33	1.28	0.84	0.59	2.18	2.69	2.69	
Tb	0.19	0.19	0.1	0.05	0.06	0.05	0.05	0.13	0.07	0.06	0.13	0.18	0.18	
Dy	0.88	0.9	0.42	0.24	0.12	0.11	0.24	0.75	0.3	0.3	0.5	0.61	0.61	
Ho	0.17	0.17	0.09	0.05	0.02	0.02	0.05	0.17	0.06	0.05	0.1	0.11	0.11	
Er	0.54	0.55	0.37	0.17	0.06	0.08	0.17	0.59	0.17	0.15	0.35	0.35	0.35	
Tm	0.089	0.09	0.072	0.027	0.01	0.012	0.032	0.098	0.025	0.021	0.053	0.052	0.052	

Table C4: Lithochemistry of baritic lower Earn Group sediments

Location	NWT												Yukon	
	Sample	09NF506B	09NF508B-W4	09NF512B	09NF512C	09NF512C	09NF512D	09NF512E	09NF516A	09NF516E	BA-09-03	09NF518B	10NF12B	10NF42F
<b>Yb</b>	0.58	0.56	0.53	0.17	0.09	0.1	0.22	0.67	0.17	0.13	0.31	0.36		
<b>Lu</b>	0.079	0.075	0.082	0.025	0.032	0.024	0.032	0.112	0.032	0.019	0.047	0.075		
<b>Hf</b>	0.7	0.7	1.4	0.4	1.1	1.1	0.4	1.1	0.7	0.8	1.8	0.3		
<b>Ce/Ce<sup>o</sup></b>	0.59	0.59	0.81	0.34	0.34	0.43	0.33	0.86	0.40	0.68	0.67	0.26		
<b>Eu/Eu<sup>o</sup></b>	0.57	-	1.35	-	-	-	-	-	3.03	-	-	1.68		
<b>Sc</b>	3	2	3	<1	<1	<1	<1	4	<1	<1	1	1		
<b>Be</b>	<1	<1	<1	<1	<1	<1	<1	<1	<1	<1	<1	<1		
<b>V</b>	240	115	686	120	94	173	35	280	53	57	80	94		
<b>Cr</b>	50	<20	40	<20	<20	<20	<20	50	<20	<20	<20	<20		
<b>Co</b>	<1	<1	<1	<1	<1	<1	<1	<1	<1	<1	<1	1		
<b>Ni</b>	<20	<20	20	<20	<20	<20	<20	<20	<20	<20	<20	30		
<b>Cu</b>	20	<10	<10	<10	<10	<10	<10	<10	<10	<10	<10	20		
<b>Zn</b>	<30	<30	50	<30	<30	<30	<30	<30	<30	<30	50	330		
<b>Ga</b>	5	4	4	<1	<1	<1	<1	5	<1	<1	2	<1		
<b>Ge</b>	1.3	<0.5	1	<0.5	<0.5	<0.5	<0.5	1.7	<0.5	<0.5	<0.5	<0.5		
<b>As</b>	<5	<5	18	<5	5	<5	<5	10	<5	<5	<5	6		
<b>Zr</b>	27	28	41	13	3	6	13	36	19	25	14	12		
<b>Nb</b>	10.6	9.2	6.3	7.7	0.2	0.3	7	3.4	10.4	7.6	0.5	0.5		
<b>Mo</b>	4	<2	16	<2	2	2	<2	9	<2	<2	4	3		
<b>Ag</b>	<0.5	<0.5	<0.5	<0.5	<0.5	<0.5	<0.5	<0.5	<0.5	<0.5	<0.5	<0.5		
<b>In</b>	<0.1	<0.1	<0.1	<0.1	<0.1	<0.1	<0.1	<0.1	<0.1	<0.1	<0.1	<0.1		
<b>Sn</b>	<1	<1	<1	<1	<1	<1	<1	<1	<1	<1	<1	<1		
<b>Sb</b>	4.7	3	16.8	1.9	0.5	1.2	<0.2	5	1.8	1	<0.2	3.7		
<b>Ta</b>	0.24	0.21	0.44	0.24	1.44	1.34	0.24	0.39	0.2	0.26	2.13	0.19		
<b>W</b>	<0.5	<0.5	1.6	<0.5	3.2	1.1	<0.5	5.5	<0.5	<0.5	<0.5	0.8		
<b>Tl</b>	<0.05	<0.05	<0.05	<0.05	<0.05	<0.05	<0.05	<0.05	<0.05	<0.05	<0.05	0.31		
<b>Pb</b>	<5	<5	37	<5	<5	<5	<5	12	<5	<5	<5	<5		
<b>Bi</b>	<0.1	<0.1	<0.1	<0.1	<0.1	<0.1	<0.1	<0.1	<0.1	<0.1	<0.1	<0.1		
<b>Th</b>	1.74	1.41	3.53	0.46	0.17	0.31	0.3	2.57	0.43	0.45	0.91	0.45		
<b>U</b>	2.85	1.33	4.31	0.92	0.51	0.57	0.4	2.43	1.13	0.7	1.25	1.47		

Table C4: Lithochemistry of baritic lower Earn Group sediments

## **APPENDIX D: RE-OS MODEL DATA**

See attached CD for spreadsheet file